2017

EFFECTS OF TEMPERATURE, ORIENTATION, LOAD LEVEL AND INDENTER SHAPE ON THE INDENTATION RESPONSE OF NITI-BASED SHAPE MEMORY ALLOYS

Peizhen Li
University of Kentucky, peizhen.li@uky.edu
Digital Object Identifier: https://doi.org/10.13023/ETD.2017.344

STUDENT AGREEMENT:

I represent that my thesis or dissertation and abstract are my original work. Proper attribution has been given to all outside sources. I understand that I am solely responsible for obtaining any needed copyright permissions. I have obtained needed written permission statement(s) from the owner(s) of each third-party copyrighted matter to be included in my work, allowing electronic distribution (if such use is not permitted by the fair use doctrine) which will be submitted to UKnowledge as Additional File.

I hereby grant to The University of Kentucky and its agents the irrevocable, non-exclusive, and royalty-free license to archive and make accessible my work in whole or in part in all forms of media, now or hereafter known. I agree that the document mentioned above may be made available immediately for worldwide access unless an embargo applies.

I retain all other ownership rights to the copyright of my work. I also retain the right to use in future works (such as articles or books) all or part of my work. I understand that I am free to register the copyright to my work.

REVIEW, APPROVAL AND ACCEPTANCE

The document mentioned above has been reviewed and accepted by the student's advisor, on behalf of the advisory committee, and by the Director of Graduate Studies (DGS), on behalf of the program; we verify that this is the final, approved version of the student's thesis including all changes required by the advisory committee. The undersigned agree to abide by the statements above.

Peizhen Li, Student

Dr. Haluk E. Karaca, Major Professor

Dr. Haluk E. Karaca, Director of Graduate Studies

EFFECTS OF TEMPERATURE, ORIENTATION, LOAD LEVEL AND INDENTER SHAPE ON THE INDENTATION RESPONSE OF NITI-BASED SHAPE MEMORY ALLOYS

DISSERTATION

A dissertation submitted in partial fulfillment of the requirements for the degree of Doctor of Philosophy in the College of Engineering at the University of Kentucky

By

Peizhen Li

Lexington, Kentucky

Director: Dr. Haluk E. Karaca, Professor of Mechanical Engineering

Co-Director: Dr. Yang-Tse Cheng, Professor of Materials Engineering

Lexington, Kentucky

2017

ABSTRACT OF THE DISSERTATION

EFFECTS OF TEMPERATURE, ORIENTATION, LOAD LEVEL AND INDENTER SHAPE ON THE INDENTATION RESPONSE OF NITI-BASED SHAPE MEMORY ALLOYS

Owing the capability of recovering large deformations through reversible phase transformation, shape memory alloys (SMAs) are well-known for their unique behaviors such as shape memory effect (SME) and superelasticity (SE), which can also be characterized by instrumented indentation techniques. Nickel titanium (NiTi) SMAs have been extensively used for nano/micro-indentation studies and widely applied to biomedical and other elaborate medical devices.

In this study, indentation responses of NiTi, NiTiHf, NiTiHfPd and NiTiHfCu alloys were investigated using spherical and Berkovich indenters at room temperature. Spherical and Berkovich indentation hardness, modulus, and work/depth recoverable ratio of these NiTi-based alloys were revealed as a function of maximum loading level at nano and macro scales. It has been revealed that indentation responses are highly composition, aging and load level dependent. Perfect work/depth recovery was observed in superelastic NiTiHfPd alloys using the spherical indenter.

Temperature-dependent shape memory properties of equiatomic NiTi, Nickel rich NiTi, and as-received and aged NiTiHf alloys were investigated using a spherical indenter between 30-340 ºC under selected load levels. Ti-6Al-4V was also tested for comparison. Spherical indentation response of aged high temperature NiTiHf alloys showed a clear relationship between the work recoverable ratio and transformation temperatures, superelastic and plastic behavior. It was concluded that indentation response can be used to measure local superelasticity response, determine phase transformation temperatures and reveal the temperature intervals of the deformation mechanisms of shape memory alloys. Spherical indentation hardness and modulus as a function of temperature can be used to exam the phase transformation, but cannot provide sufficient information regarding the superelastic and plastic behavior.

Orientation dependence of the shape memory properties in aged Nickel rich $Ni_{50.3}Ti_{29.7}Hf_{20}$ single crystals were investigated along the [100], [110] and [111] orientations under room and high temperatures through indentation techniques. Indentation hardness, modulus and work /depth recoverable ratio were investigated as a function of temperature and indentation depth/load. It was found that indentation response of work recovery ratio is orientation independent, however, shape memory properties (e.g.

transformation temperatures) determined from the indentation responses are almost orientation independent.

KEYWORDS: Nanoindentation; Shape memory alloys; High temperature indentation; Local mechanical characterization;

Peizhen Li

Student's Signature

07/27/2017

Date

EFFECTS OF TEMPERATURE, ORIENTATION, LOAD LEVEL AND INDENTER SHAPE ON THE INDENTATION RESPONSE OF NITI-BASED SHAPE MEMORY ALLOYS

By

Peizhen Li

Haluk E. Karaca

Director of Dissertation

Yang-Tse Cheng

Co-Director of Dissertation

Haluk E. Karaca

Director of Graduate Studies

07/27/2017

This work is dedicated to my mother and father.

ACKNOWLEDGEMENTS

Foremost, I would like to sincerely thank my research advisor, Prof. Haluk E. Karaca, who provided to me with his guidance, patience, encouragements, and the opportunities to complete this dissertation and taught me how to conduct scientific research. His willingness to dedicate his time so generously has been very much appreciated. He has kept encouraging me to read literature and has taught me how to write scientific articles, trained me to be a professional engineer, given me opportunities to develop my communication and leadership skills through student organizations and conferences. This research work could not have been made possible without his guidance and comments.

I would like to express my sincere gratitude towards Prof. Yang-Tse Cheng from the Department of Material Science Engineering for his valuable suggestions and creative ideas on my research work. I appreciated the convenience to access all the equipment and labs I needed from Prof. Yang-Tse Cheng, and his patience and guidance of editing my manuscripts. His encouragement and intelligence motivated me to pursue further in research and to develop myself as a competent researcher.

I am also grateful towards my PhD committee members, Prof. Christine Trinkle, Prof. Charles Lu, and Prof. Keith Rouch for their valuable time, and for giving valuable comments and suggestions during my PhD study.

I am especially thankful and grateful to my former senior colleague, Dr. Ali Sadi Turabi, who has mentored and introduced me with most of the experimental work and study. He has been a great friend and colleague in my life. I would also like to thank my lab and office mates during my PhD degree, Irfan Kaya, Sayed Saghaian, Dr. Hirobumi

Tobe, Mohannad Souri, Soheil Saedi, Ethan Vance, Sesha spanadana Pulla, Jie Pan, and Yikai Wang. I also appreciate the generous advice and training from Tim Jochum on the NanoVantage equipment. Thanks also to the technicians of the mechanical engineering department for their help. I would also like to thank all my friends who supported me in writing, and incented me to strive towards my goal. All of you have been there to support me when I recruited patients and collected data for my Ph.D. thesis.

Finally, I would like to express my gratitude to my father and mother for their supports. Words cannot express how grateful I am for all of the sacrifices that you've made on my behalf. Your supports and believes were what sustained me thus far.

Table of Contents

Acknowledgements……..…….....III

List of Figures…… VIII

List of Tables…… XIII

1 INTRODUCTION 1
1.1. Motivation and Purpose of the Study 1
1.2. Mechanism of Shape Memory Alloys 5
1.2.1. Thermal-Induced Martensitic Transformation 7
1.2.2. Shape Memory Effect 11
1.2.3. Two-Way Shape Memory Effect 12
1.2.4. Superelasticity 14
1.3. Background of NiTi-Based Shape Memory Alloys 17
1.3.1. Nickel Titanium Shape Memory Alloys 18
1.3.2. Ni-Rich NiTiHf Alloys 22
1.3.3. NiTiHf –X (X= Cu, Pd) Alloys 24
2 LITERATURE REVIEW OF INDENTATION 27
2.1. History and Overview of Indentation. 27
2.2. Contact Mechanisms 28
2.3. Indentation in Shape Memory Alloys 33
2.4. Indentation-Induced TWSME 37
2.5. High Temperature Indentation 40
2.6. Indentation in Single Crystal 43
3 EXPERIMENTAL METHODOLOGY 44
3.1. Material Preparation 44
3.2. Calorimetry Measurements 45
3.3. Surface Polishing 46
3.4. Mechanical Testing 47
3.5. Indentation 48
4 INDENTATION RESPONSE OF NITI-BASED SHAPE MEMORY ALLOYS AT AMBIENT TEMPERATURE 55

4.1. Introduction 55
4.2. Stress-Free Phase Transformation Temperatures of NiTi-Based Alloys 57
4.3. Shape Memory Behavior of NiTi-Based Alloys 58
4.4. Spherical Indentation Response of NiTi and NiTiHfPd Alloys 59
4.4.1. Spherical Indentation Load-Depth Curves 59
4.4.2. Discussion 62
4.4.3. Conclusion 69
4.5. Load and Indenter Effect of NiTi-Based Shape Memory Alloys 70
4.5.1. Spherical and Berkovich Indentation Load-Depth Curves of NiTi-Based Alloys 70
4.5.2. Discussion 79
4.5.3. Conclusion 88
5 TEMPERATURE DEPENDENT INDENTATION RESPONSE OF AGED NITIHF SHAPE MEMORY ALLOYS 90
5.1. Introduction 90
5.2. Shape Memory Behavior and Phase Diagram of aged $Ni_{50.3}Ti_{29.7}Hf_{20}$ 93
5.3. Load-Depth Curves of Aged NiTiHf Shape Memory Alloys under Heating and Cooling 96
5.4. Work Recoverable Ratio Vs. Temperature 99
5.5. Conclusion 105
6 LOAD AND TEMPERATURE DEPENDENT INDENTATION RESPONSE OF NITI-BASED SHAPE MEMORY ALLOYS 107
6.1. Introduction 107
6.2. Temperature and Load Effect of as-received NiTiHf Shape Memory Alloy under Spherical Indenter 109
6.2.1. Load-Depth Curves of as-received NiTiHf Shape Memory Alloys under Heating and Cooling 109
6.2.2. Discussion 111
6.2.3. Conclusion 120
6.3. Temperature and Load Effect of NiTi-Based Shape Memory Alloys under Spherical Indenter 121
6.3.1. Load-Depth Curves of NiTi-based Shape Memory Alloys under Cooling 121
6.3.2. Discussion 124

6.3.3. Conclusion 133
7 ORIENTATION DEPENDENT INDENTATION RESPONSE OF NITI-BASED SMAS 134
7.1. Introduction 134
7.2. Load-Depth Curves of Single Crystal NiTiHf SMAs 134
7.3. Discussion 136
7.3.1. Indentation Work Recovery 136
7.3.2. Deformation Behavior in Schematics 139
7.3.3. Deformation Behavior during Heating 140
7.3.4. Deformation Behavior during Cooling 145
7.3.5. Work Recovery Analysis in [100] and [110] 147
7.4. Conclusions 150
8 GENERAL CONCLUSIONS AND FUTURE WORKS 151
REFERENCES 156
VITA 161

List of Figures

Figure 1.1: Actuation energy density diagram of different active materials [1]. 2
Figure 1.2: Actuation frequency of active materials [1]. 2
Figure 1.3: Schematic illustration of austenite and martensite phase with invariant plane as a habit plane [1]. 8
Figure 1.4: Thermal induced phase transformation a) in the absence of applied stress, b) in the presence of applied stress..... 11
Figure 1.5: Schematics of shape memory effect in SMAs described in (a) structure, (b) experimental..... 12
Figure 1.6: A typical schematic of superelastic behavior loading-unloading cycle explained in (a) structure, (b) experimental. 15
Figure 1.7: Schematic of relationship between critical stress and temperatures in SMAs. 16
Figure 1.8 The Homer Mammalok ^{TM} Nitinol wire needle localizer [45]. 18
Figure 1.9:The compressive stress-strain response of Ni-rich $Ni_{54}Ti_{46}$ aged samples as a function of temperature [5]. 20
Figure 1.10: Orientation dependence of stress-strain behavior of $Ni_{50.8}Ti_{49.2}$ alloy [6].... 21
Figure 1.11: The compressive stress-strain response of aged $Ni_{51}Ti_{49}$ single crystals as a function of temperature [49]. 22
Figure 1.12: Composition dependence of the martensitic peak temperature Mp, as a function of (a) hafnium content in NiTiHf system, (b) Zr content in the NiTiZr alloy system [6]..... 23
Figure 1.13: Superelastic behavior for the $Ni_{50.3}Ti_{29.7}Hf_{20}$ alloy as a function of temperature, (a) as-extruded, (b) aged 550 ˚C-3h, (c) aged 650 ˚C-3h [9]..... 24
Figure 1.14: Stress-strain response of Ni45.3Ti29.7Hf20Cu5 alloys aged at 550C-3 hours [66]..... 25
Figure 1.15: Isothermal stress-strain curves for polycrystalline NiTiHfPd (a) as-extruded, (b) aged at 400°C for 3h, (c) aged at 550°C for 3h, and (d) aged at 650°C for 3h demonstrating superelastic behavior [13]. 26
Figure 2.1: Schematic illustration of the unloading process showing parameters characterizing the contact geometry with (a) a Vickers indenter, (b) indentation load-displacement data [72]. 30
Figure 2.2: (a) Contact geometry of a spherical indenter with a tip radius of R_r, (b) corresponding load-displacement curve for an elastic-plastic specimen loaded with a spherical indenter [66]. 31
Figure 2.3: Elastic-plastic indentation response of a mild steel material, (a) Top view of residual impression in the surface, (b) Cross section view of subsurface underneath indent, (c) Finite element results of pressure distribution, (d) Finite element results of plastic zone distribution [73]. 32
Figure 2.4: (a) Dimensionless load-displacement curve under Berkovich indenter, (b) dimensionless L-D curve under spherical indenter, (c) recovery ratio under Berkovich indenter, and (d) recovery ratio under spherical indenter [12]. 34

Figure 2.5: Microscopic shape memory effect: spherical indentation in the martensitic NiTi shape memory alloy [14]. 35
Figure 2.6: (a) Comparison of experimental and FE modeling, (b) recovery ratios vs representative strains at different depths [88]. 37
Figure 2.7: Two-way indentation depth change (a) over 5 thermal cycle, (b) indentation depth change ratio and absolute depth change [90]. 38
Figure 2.8: Indent training (a-c) and planarization (d) thermal cycling to obtain surface form memory effect (e-f) [15]. 39
Figure 2.9: Depth measurements of (a) initial indent depth-recovery, and (b) extent-to-flat surface transition during heating and cooling after planarization of the LSP indent [15]. 40
Figure 2.10: Plots of (a) load-depth obtained during indentation at various temperature around and below A_f, (b) remnant depth ratio as a function of indentation temperature at two different loads by using a spherical indenter (r=10μm) [100]. 42
Figure 3.1: Electrical discharge machining (EDM) to cut specimens into desired shapes. 45
Figure 3.2: Perkin-Elmer Pyris 1 Differential Scanning Calorimeter to measure the stress free phase transformation temperatures. 46
Figure 3.3: Buehler EcoMet 250 Grinder-Polisher (AutoMet 250 Power head) with chemical polishing. 47
Figure 3.4: The MTS Landmark servo-hydraulic test frame. 48
Figure 3.5: Sun-Tec model FM-7 micro-hardness test equipment. 49
Figure 3.6: Nano Test Vantage Instrumented Indentation Machine (a) the outside figure, (b) detail setup of the inside configurations with low load and high load heads. 50
Figure 3.7: The horizontal loading design of the NanoTest Vantage with the high temperature set up. 52
Figure 3.8: An example spherical indenter with a tip radius of 5 μm and a full angel of 60 degree. 53
Figure 3.9: Corresponding indentation load-depth curve with important indentation parameters. 54
Figure 4.1: Stress-strain relationships of NiTi-based alloys on bulk material at room temperature. 59
Figure 4.2: Nano-indentation results of typical load-displacement relationships. Load-displacement curve of a) NiTi-M and NiTi-A at 10mN, 25mN, and 50mN b) NiTiHfPd-M (600) and NiTiHfPd-A(400) at 10mN, 25mN, and 50mN (c) NiTi-M and NiTi-A at 100, 250 and 500mN (d) NiTiHfPd-M (600) and NiTiHfPd-A(400) at 100, 250 and 500mN. 61
Figure 4.3: Work recoverable ratios as a function of D_{max}/R of NiTi and NiTiHfPd alloys. Data were calculated from six load levels of 10mN, 25mN, 50mN, 100mN, 250mN and 500mN. 63
Figure 4.4: Depth recovery ratio as function of maximum indentation depth for NiTi and NiTiHfPd alloys. Zhang's results from modeling of superelastic NiTi were added for comparison [88]. 65

Figure 4.5: The corresponding dimensionless load-displacement curves (a) NiTi alloys at 10mN, (b) NiTi alloys at 25mN, (c) NiTi alloys at 50mN, (d) NiTiHfPd alloys at 10mN, (e) NiTiHfPd alloys at 25mN, (f) NiTiHfPd alloys at 50mN. 66
Figure 4.6: Hardness vs. maximum depth relationship of NiTi and NiTiHfPd alloys. Data were calculated at selected load of 10mN, 25mN, 50mN, 100mN, and 250mN. 69
Figure 4.7: Spherical and Berkovich nano-indentation L-D response under load 10 mN, 25 mN, and 50 mN of (a) NiTi-M, (b) NiTi-A, (c) NiTiHf-A, (d) NiTiHfPd-A, (e) NiTiHfPd-A (400), (f) NiTiHfPd-M (600), (g) NiTiHfCu-M (500), and (h) NiTiHfCu-M (600) alloys. The solid line represents the spherical indentation data, while the dash line is from Berkovich indentation response. 74
Figure 4.8: Spherical and Berkovich nano-indentation L-D response under load 100 mN, 250 mN, and 500 mN of (a) NiTi-M, (b) NiTi-A, (c) NiTiHf-A, (d) NiTiHfPd-A, (e) NiTiHfPd-A (400), (f) NiTiHfPd-M (600), (g) NiTiHfCu-M (500), and (h) NiTiHfCu-M (600) alloys. The solid line represents the data from spherical tip, while the dash line is from Berkovich tip. 77
Figure 4.9: (a) Maximum indentation depth (D_{max}), (c) recoverable depth (D_r), of all alloys as a function of selected loads under both spherical and Berkovich indenters. (b) is the zoom of (a) till load level of 250 mN, and (d) is the zoom of (b) at same load level. 79
Figure 4.10: (a) Indentation hardness vs. D_{max}/R relationship of all alloys under spherical tip, and (b) hardness vs. maximum depth D_{max} relationship of all alloys under Berkovich tip. Data was calculated at selected peak load of 10, 2, 50, 100, 250 and 500mN. To be noted, H vs. D_{max}/R shows indentical trend with H vs. D_{max}, thus, it is comparable with other results under different tip sizes. 82
Figure 4.11: Indentation work recovery ratio against the (a) D_{max}/R of all alloys under spherical tip, as well as the copper from Ni et al [79], (b) D_{max} of all alloys under Berkovich tip, as well as the copper from Ni et al [92]. Data was calculated at selected peak load of 10, 2, 50, 100, 250 and 500mN. 85
Figure 4.12: Calculated indentation modulus E as a function of (a) D_{max}/R of all alloys, as well as fused silica and Al from Ni et al [79], (b) D_{max} of all alloys under Berkovich indenter. Data was calculated at selected peak load of 10, 25, 50, 100m, 250 and 500mN. 88
Figure 5.1: Optical microscopy image of aged $Ni_{50.3}Ti_{29.7}Hf_{20}$ after indentation experiments. 92
Figure 5.2: Phase transformation diagram of aged $Ni_{50.3}Ti_{29.7}Hf_{20}$. The stress-strain curves showing temperature dependency of the critical stress (a); relationship of critical stress and transformation temperatures (b). 96
Figure 5.3: Spherical indentation responses of typical load-displacement relationships at selected temperature. Load-displacement curves of NiTiHf under load 500 mN with (a) heating process from 28 °C to 340 °C, and (b) cooling process from 340 °C to 28 °C. . 99
Figure 5.4: Spherical indentation response of work recovery ratio (a), maximum indentation depth D_{max} (b) as a function of temperature under 500 mN of NiTiHf with heating process from 28 °C to 340 °C marked as circle and cooling process from 340 °C to 30 °C marked as triangle. 105

Figure 6.1: Spherical indentation responses of typical load-displacement relationships at selected temperature. Load-displacement curves of NiTiHf under load 500 mN with (a) heating process from 30 to 320 °C, (b) cooling process from 320 to 30 °C; and under 2000 mN with (c) heating process from 30 to 320 °C, (b) cooling process from 320 to 30 °C. 111
Figure 6.2: Spherical indentation response of work recoverable ratio as a function of temperature for as-received NiTiHf alloy under load (a) 500 mN, (b) 2000 mN..... 114
Figure 6.3: Spherical indentation response of hardness as a function of temperature for as-received NiTiHf alloy under load (a) 500 mN, (b) 2000 mN. 116
Figure 6.4: Spherical indentation response of modulus as a function of temperature for as-received NiTiHf alloy under load (a) 500 mN, (b) 2000 mN. 118
Figure 6.5: Spherical indentation responses of typical load-displacement relationships. Load-displacement curve of (a) Ti under load 500 mN and (b) Ti under load 2000 mN, (c) NiTiHf under load 500 mN, (d) NiTiHf under load 2000 mN, (e) NiTi under load 500 mN, (f) NiTi under load 2000 mN, (g) 50.8NiTi under load 500 mN, (h) 50.8NiTi under load 2000 mN as a function of temperature from 340 °C down to 28 °C. 124
Figure 6.6: Work recoverable ratio as a function of temperature for a) NiTiHf, b) NiTi, c) 50.8NiTi, and d) Ti under load 500 mN and 2000 mN..... 126
Figure 6.7: Spherical indentation hardness as a function of elevated temperatures for a) NiTiHf, b) NiTi, c) 50.8NiTi, and d) Ti under load 500 mN and 2000 mN..... 129
Figure 6.8: Spherical indentation modulus as a function of temperature for NiTiHf, NiTi, 50.8NiTi, and Ti under load (a) 500 mN and (b) 2000 mN..... 131
Figure 7.1: Spherical indentation response of typical load-depth relationships at selected temperatures between 30 and 340 °C under 500 mN. The L-D curves of [100]-oriented NiTiHf 650 °C-3h are shown in (a) heating and (b) cooling process. 136
Figure 7.2: Spherical indentation response of work recoverable ratio (a) and the corresponding maximum depth (b) as a function of temperature under 500 mN of single crystal NiTiHf aged at 650 °C-3h with heating process from 30 to 340 °C marked as circle and cooling process from 340 to 30 °C marked as triangle in [111] orientations. 138
Figure 7.3: The schematic drawing of (a) work recovery, and (b) maximum indentation depth as a function of temperature during heating (solid lines) and cooling (dotted lines). 140
Figure 7.4: Temperature dependent compressive stress-strain relation of a typical SMA during heating process in (a) stage *IH* (T< *AsI*), (b) Stage IIHa (AsI< T< As*), (c) Stage IIHb (As*< T< AfI), (d) Stage IIIH (AfI<T<TSE), (e) Stage IVH (TSE<T<Md), and (f) Stage VH (T > Md). The correspondent D_{max} is also presented at each temperature..... 144
Figure 7.5: Temperature dependent compressive stress-strain relation of a typical SMA during cooling process at (a) Stage IICa (MsI< T< Af*I*), (b) temperature 125 °C (MsI), (c) temperature 115 °C (Ms*), (d) Stage IICc (Mf*I*<T<Ms*). The correspondent D_{max} is also presented at each temperature..... 147
Figure 7.6: Spherical indentation response of work recoverable ratio as a function of temperature under 500 mN of single crystal NiTiHf aged at 650 °C-3h with heating

process from 30 to 340 °C marked as circle and cooling process from 340 to 30 °C marked as triangle in (a) [111] and (b) [110] orientation. 149

List of Tables

Table 3.1: Spherical indenters with calculated theoretical maximum limit parameters. .. 53
Table 4.1: Transformation temperatures observed from DSC and Vicker's hardness at room temperature for NiTi-based alloys. 58
Table 4.2: Calculated D_{max}/R of NiTi, NiTiHf NiTiHfPd, and NiTiHfCu alloys at selected load level of 10mN, 25mN, 50mN, 100mN, 250mN, and 500mN. 62
Table 4.3: Depth recovery ratio of spherical indents on NiTi and NiTiHfPd alloys at selected load levels. 64
Table 4.4: The minimum and maximum indentation hardness of eight alloys from spherical and Berkovich indentation response, and also the hardness measurements from Vichkers. 82
Table 6.1: Transformation temperatures observed from DSC and Vickers hardness at room temperature for Ti, NiTi, 50.8NiTi and NiTiHf alloys..... 108
Table 6.2: Shape memory properties observed from DSC, indentation work recovery, hardness, and modulus at varied load levels. 119
Table 6.3: Indentation temperature stages of Ti, NiTi, 50.8NiTi and NiTiHf alloys under both 500 mN and 2000 mN load. Indentation Hardness..... 127
Table 6.4: Shape memory properties such as TTs, T_{SE}, and M_d observed from temperature dependent indentation response under two load levels were listed for NiTi, NiTiHf alloys. 132
Table 7.1: Shape memory properties observed from indentation work recovery and hardness under 500 mN from [100], [110], and [111] orientations, as well as the DSC results. 149

1 INTRODUCTION

1.1.Motivation and Purpose of the Study

Mechanical characterizations such as compression and tension tests have been widely used on bulk metals for centuries in order to understand their behavior. With advancements and improvements in the field of material science over the last few decades, shape memory (coupling of thermal with mechanical fields), piezo-electric (coupling of mechanical with electrical fields) and piezo-magnetic (coupling of mechanical with magnetic fields) alloys have been called multifunctional materials as they exhibit a mechanical response once subjected to non-mechanical field (i.e. thermal, electrical, magnetic, etc.). The most desirable and ideal active material should have high actuation energy density, frequency and stress since these essential factors determine the suitability of an active material application. Common active materials are distributed in Figure 1.1 with their actuation energy densities and Figure 1.2 with respect to the actuation frequencies [1]. Actuation energy density distribution is shown by the dotted lines in Figure 1.1, and materials are the products of the actuation strain with the actuation stress. Although magnetic shape memory alloys and shape memory polymers have the highest actuation energy density and larger stain compared with standard shape memory alloys (SMAs), the actuation stress is much lower. In addition, Figure 1.2 shows that shape memory alloys have the highest specific actuation energy density with a magnitude frequency response of 10. Owing the ability to recover large shape deformation under high stress levels once temperature is increased and the potential to dissipate mechanical energy by undergoing a reversible hysteretic mechanical loading cycle, and with the benefit of high actuation density, stress, and suitable range of frequency response, SMAs have been selected as an

essential candidate for actuators, sensors, dampers, sealing elements, couplers, biomedical devices and electrical components [1, 2]. Since the discovery of SMAs, much attention and progress has been made both in the scientific understanding and applications of the system and mechanisms of shape memory effect (SME) and superelasticity (SE).

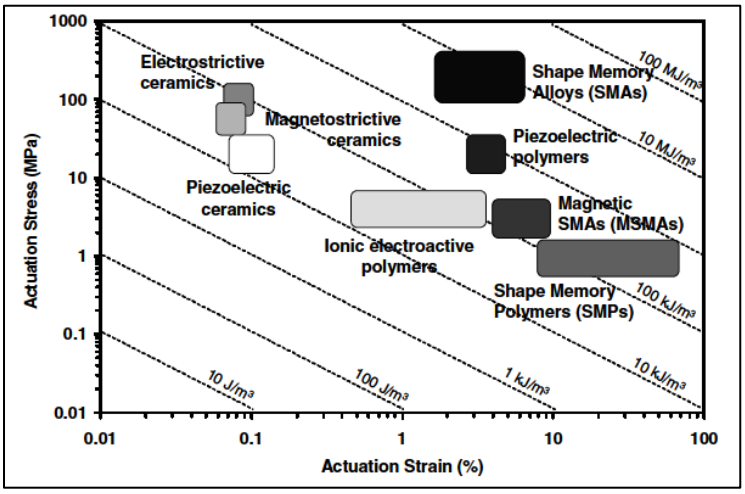

Figure 1.1: Actuation energy density diagram of different active materials [1].

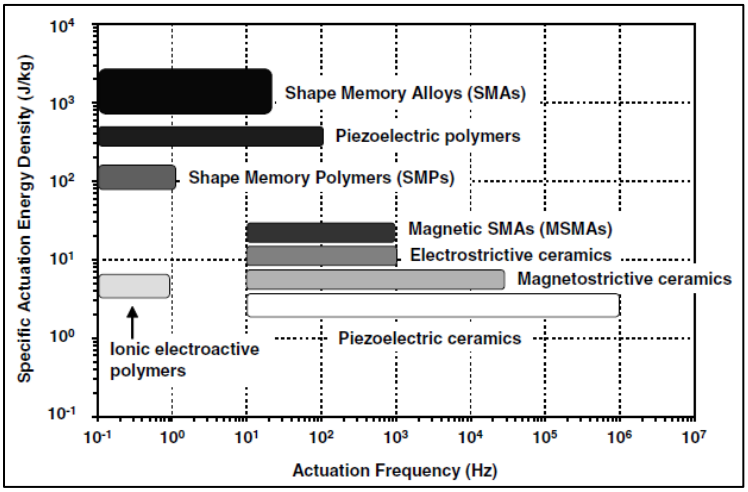

Figure 1.2: Actuation frequency of active materials [1].

The design of SMAs-based micro-electro-mechanical systems (MEMS) and elaborate medical devices require the characterization of material performance on small-

scale systems instead of bulk materials. Consequently, tools that can quickly and accurately interpret the mechanical properties on small-scale materials are required to be assembled [3]. One method to extract small-scale mechanical properties of metals is the instrumented indentation techniques. Compared to other mechanical characterization techniques, the indentation method has several advantages, such as the uncomplicated sample preparation, the quantitative characterization under nano-scale, rapid performance with non-oxidization at elevated temperature, and the ability to measure mechanical properties of thin films. Various macro-, micro-, and nano-indentation methods have been employed in SMAs as alternatives to the conventional compressive/tensile tests for measuring the shape memory properties.

NiTi alloys are the most explored and widely used SMAs due to their good ductility, dimensional stability, large transformation strain (10 %), and superior shape memory properties (SME and SE). In addition, NiTi alloys have good corrosion resistance, biocompatibility, and high work output capability, which are critical to applications in the biomedical field. However, low transformation temperatures (<100 ^{o} C) and strength (<700 MPa) of near-equiatomic NiTi alloys limit a wider use of their applications in high temperatures or strength environments [4]. Ni-rich NiTi shape memory alloys have better superelasticity and shape memory properties than near equiatomic NiTi shape memory alloys [5]. Aging and composition alteration can be employed to strengthen and control their transformation temperatures to result in superelasticity at room temperature [5-10]. It has been shown that superelastic NiTi alloys have large recoverable depths [11], where the depth recovery ratio of a superelastic NiTi was about 45% for Berkovich (~200 mN) and 95 % for spherical (~2.75 N) indenters [12]. Thus, it can be concluded that extensive plastic

deformation can be omitted and superelasticity can be detected much easier by using a spherical indenter [12].

However, with the increasing interests of applications in industries such as aerospace and automotive, which require high temperature and strength SMAs, ternary elements such as Hf, Zr, Pd, and Pt are added to NiTi alloys to increase their transformation temperatures while maintaining its superior shape memory properties. It has been found that the Hf addition in NiTi seems to be the most promising of the HTSMAs for a wide range of applications between temperatures of 100-300 ºC based on the consideration of low cost, medium ductility and high work output as compared with other elements [6]. Recently, the quaternary alloy of NiTiHfPd was developed as a high damping materials which could be utilized as dampers in aircraft engines to decrease the acoustic energy as well as in construction devices to counter seismic movements. Damping capacity is defined as the amount of energy that can be dissipated from a system, where good damping materials should have a large hysteresis loop under high stress level. Moreover, the high damping capacity of the quaternary NiTiHfPd alloys are 30-34Jcm^{-3}, and their shape memory properties can be controlled by aging and orientation selection [13]. To date, ternary NiTi-based alloys have not been extensively studied under instrumented indentation techniques, and the investigation of quaternary high damping NiTi-based alloys with indentation has not been generally pursued. Furthermore, the SMAs are highly temperature and orientation dependent. Thus, the current study will focus on the characterization of NiTi-based polycrystalline alloys through nano-, macro-indentation techniques at both room temperature and high temperatures. Indentation response of the effect of orientation on NiTi-based single crystal alloys will be investigated.

With the inspiration of the 'self-healing' effect through indentation [14] (where the shallow spherical indents in austenitic NiTi can fully recover upon unloading, and indents in martensite can partially recover after unloading and full recovery occurs upon heating to austenite phase), a planarization step was added in the martensitic state after the indent's initial heating and cooling in order to create a thermally-reversible-controlled flat to patterned surface which is so called 'Surface Form Memory' (SFM) [15]. The protrusions were caused by preferentially-oriented dislocation structures remained underneath the round indenter and the stress distributed around the indentation site after planarization. Once the temperature is reached to initiate the thermally-induced phase transformation, the temperature assist positive depth would occur as a protrusion. Such a flexible SFM can be used in aerospace to control the flow type (laminar or turbulent) of a surface which opens the realm for many exciting potential functionalities such as tribological or self-cleaning applications. Thus, further study of SFM on NiTi and HTSMAs NiTiHf alloys are the motivation in this study to optimize the highest protrusion with different sizes of spherical tips. Macro-indentation prints made by a MTS compressive load frame and laser shock-wave imprinting method were introduced on NiTi and NiTiHf alloys and demonstrated the maximum two-way shape memory effect recovery in depth.

1.2.Mechanism of Shape Memory Alloys

Shape memory alloys are distinguished from other conventional metals by their unique properties such as shape memory effect (SME) and superelasticity (SE), where they can produce very large recoverable strain (up to 20 % uniaxial strain) through reversible phase transformations [16][17]. SMAs are an extraordinary group of materials that undergo solid to solid state diffusionless phase transformation which involves the coordinate

movement of the atoms in the crystal as the material structure transforms from one to another. Since no diffusion processes are involved, the local concentration of the chemical composition is not affected, only the changes in crystal structure are impacted. Within the operating temperature range, SMAs have two phases which play important roles in shape memory alloys. Each phase has a different crystal structure and therefore different mechanical properties. The high temperature phase is called "*austenite*" (A) and the low temperature phase is termed "*martensite*" (M). Austenite phase is high symmetry cubic crystal structure while martensite can be tetragonal, orthorhombic or monoclinic structures. Each martensitic crystal structure can be formed in different orientation directions, named "variant". There are two forms of martensitic variants that exist: twinned (self-accommodated) and detwinned (reoriented or deformed) martensite. The transformation from one phase to another can be triggered by shear lattice distortion, temperature, stress, or magnetic fields. Therefore, the fundamental reason for the unique behavior of these alloys is due to the martensitic phase transformation. Detailed discussion can be found in the following sections.

Shape memory alloys have been considered as active or multifunctional materials. The development of these novel materials have made great contributions to material engineering and industry. Active materials can produce a mechanical response when a non-mechanical field (thermal, electrical, magnetic) is applied. Piezoelectrics, electristrictives, and shape memory materials are the main groups of active materials. However, shape memory alloys display more distinctive properties (SME, SE) than other active materials. Such behaviors were utilized and applied to practical applications in function engineering, medical devices, and surface morphology fields.

A major step towards the eventual discovery of shape memory alloys can be attributed to the discovery of martensite in steel in the 1890s by Adolf Martens. Then the martensitic phase transformation was the most widely studied topic in the early 1900s. However, it was established that the martensitic transformation as observed in the Fe-C system was an irreversible process. The reversible martensitic transformation in SMAs can be understood by the sense that as a material cools down from the high temperature phase austenite to the relative low temperature martensite phase the "f*orward*" transformation takes place and an increase in temperature results in the "*reverse*" transformation from martensite to austenite. Such concepts of thermally reversible martensitic transformation was initially introduced and explained on CuZn and CuAl alloys by Kurdjumove in 1949 [18], and later InTl and CuZn also demonstrated such a phenomenon. Chang and Read [19] revealed the fundamental mechanisms in the crystal lattice was attributed to the thermoelastic behavior of the martensitic phase transformation (thermoelastic martensitic phase transformation) where no additional lattice defects were created in these reversible processes.

1.2.1. Thermal-Induced Martensitic Transformation

The high temperature austenite parent phase with a B2 type order bcc structure can transform to the martensite phase with monoclinic B19' type lattice at low temperature through shear distortion of the lattice structure (motion of atoms). Owning the well-defined characteristics, the martensitic transformation is distinguished from other transformations. In a single grain in a polycrystalline material shown as the schematic in Figure 1.3, austenite and martensite are separated by the interface plane, where the shear distortion occurs. This plane is defined as the "*habit plane*" or referred to as "*lattice invariant plane*"

since it does not deform or rotate during transformation. Martensite matrix and martensite twins are formed in the martensite phase. A single twinned martensite domain is called "*habit plane variant*" (h.p.v.), and martensite twins with different variants have correspondence with the austenite phase, so called "*lattice correspondence variants*" (LCP). The transformation to martensite can occur along the habit plane by two different mechanisms: 1) slip between atoms by one or more atomic space; 2) twinning where atoms moving through a fraction of an atomic space. To be noted, these mechanisms of martensitic formation involve very small or no volumetric change in the material. However, the detwinning process of a SMA can result in a relative displacement of atoms which causes a macroscopic shape change.

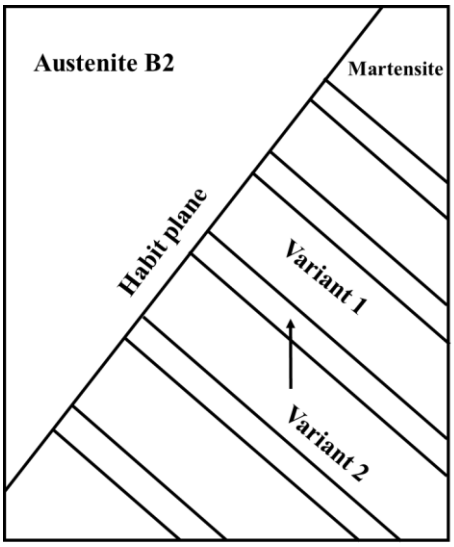

Figure 1.3: Schematic illustration of austenite and martensite phase with invariant plane as a habit plane [1].

The transformation from austenite to martensite and vice versa is associated with the release and absorption of latent heat. Thermal-induced martensitic transformation can be observed in both conditions of stress-free and with applied stress. Figure 1.4 demonstrates the temperature-induced phase transformation in the absence and presence of

applied mechanical stress. Upon cooling in the absence of an applied load shown in Figure 1.4a, the crystal structure changes from austenite to martensite, where the phase transformations are represented as peaks and the areas underneath the peaks are the enthalpies of transformations. At high temperature, it is in austenite phase with the cubic structure. Phase transformation happens from austenite to martensite during cooling is termed as "*forward transformation*" and the arrangement of variants occurs with negligible shape change, resulting in self-accommodated (twinned) martensite. When the material is heated from martensitic phase and as a result, the phase transformation takes place from martensite to austenite during heating. This transition is called "*reverse transformation*" or "*back transformation*", during which there is no associated shape change. There are four characteristic temperatures generally measured by drawing the tangents to the start and end regions of the transformation peak and the heating and cooling curves shown in Figure 1.4a. During forward transformation, fully austenite phase under zero load, begins to transform to the twinned martensite at the martensite start temperature (M_s) and followed with martensite finish temperature (M_f), at which the phase transformation is completed and material is fully martensite. Similarly, during heating of the fully martensite phase, reverse transformation was initiated at the austenite start temperature (A_s) and completed at austenite finish temperature (A_f) where the material is fully austenite phase. The forward transformation from A to M is exothermic and the reverse transformation from M to A are endothermic reactions. The specific heat capacity can be computed by normalizing the power by the heating rate and the weight of the specimen. Transformation temperatures can be significantly affected by the stored mechanical energy (i.e. precipitates, detwinning), therefore making the initial state of the material very important. Identifying these

transformation temperatures (TTs) is the essential and initial step for SMAs so that alloys can be effectively investigated with further experimental procedures.

It is also possible to obtain the temperature-induced martensitic phase transformation under applied load and during which materials associate the shape change. It is instructive to note that the load applied should be sufficient to initiate the detwinning process, otherwise no phase transformation can be observed, such corresponding stress level is called "*detwinning start stress*" (σ_s). However, sufficiently high stress can result in complete detwinning of martensite, and such stresses can be termed as "*detwinning finish stress*" (σ_f). As shown in Figure 1.4b, if a stress higher than σ_s is isothermally applied in austenitic phase, the phase transformation will result in the direct formation of detwinned martensite phase with a net shape change once the material is cooled. At low temperatures, the material is in the fully detwinned martensite phase. Reheating the material to the temperature above A_f will result in full shape recovery while the load is still applied. Such perfect shape recovery occurs only in the condition that the applied stress is not high enough to produce dislocations or defects, which results in plastic deformation. Heating and cooling with an appropriate temperature range under applied stress gives TTs (M_s^σ, M_f^σ, A_s^σ, A_f^σ) measured by the tangent method as shown in Figure 1.4b.

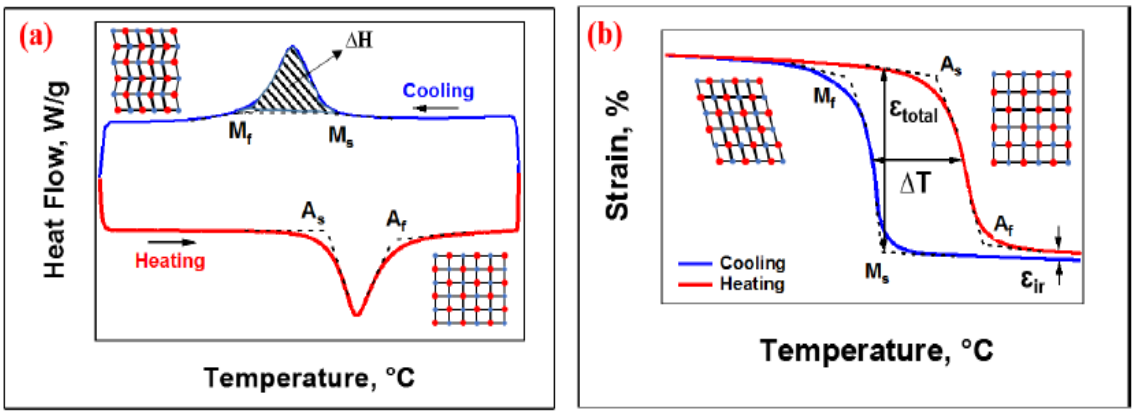

Figure 1.4: Thermal induced phase transformation a) in the absence of applied stress, b) in the presence of applied stress.

1.2.2. Shape Memory Effect

The thermo-elastic martensitic transformation is a reversible solid-solid phase transformation with no additional lattice defects in shape memory alloys. However, unique properties exhibited by shape memory alloys depend on the TTs of the alloy and the operating temperature. As mentioned previously, cooling materials from the parent phase (austenite) without any stresses can results in twinned martensite (no shape change) by self-accommodating mechanisms. If a mechanical load is applied to the SMA in the twinned martensitic phase (temperature below M_f), stress distorts self-accommodating structures and selects favored martensite variants grow along the application direction. Figure 1.5a shows schematics of the detwinned martensite phase formed by reorienting a certain number of martensitic variants. Consequently, the detwinning process results in a shape change, where the deformation in the material is retained in the detwinned structure while the load is released (Figure 1.5b). If the material is heated above A_f temperature in both cases (stress-free and with stress), the martensite phases can transform back to the austenite phase (original shape). This natural mechanism is defined as "*one-way shape*

memory effect" or "*shape memory effect*". It is instructive to mention that the deformed strain might not be fully recovered by heating up above A_f if the applied stress is sufficient to introduce plastic deformation, the irrecoverable strain (ε_{irr}) remains after heating. As illustrated in Figure 1.5b, the total recoverable strain is the summation of the elastic (ε_{el}) and shape memory effect (ε_{SME}) strains.

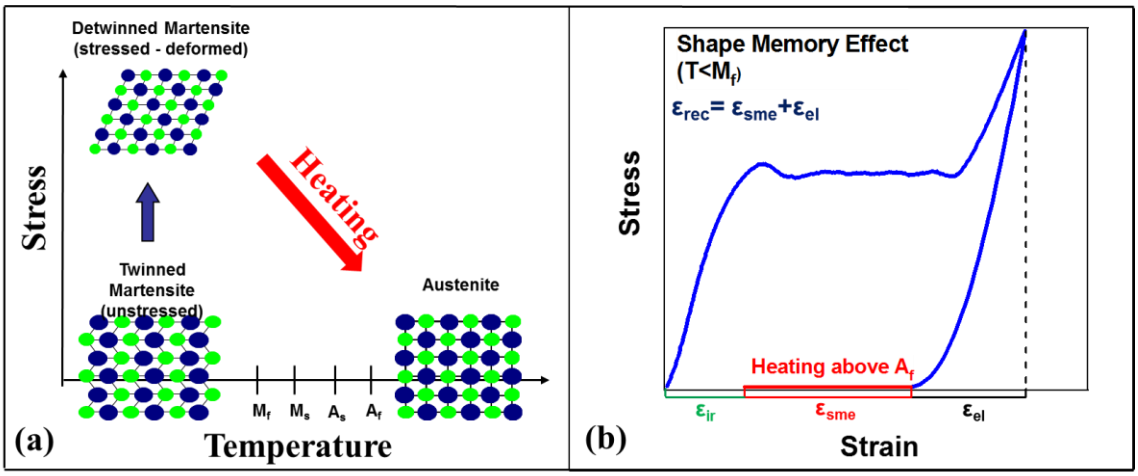

Figure 1.5: Schematics of shape memory effect in SMAs described in (a) structure, (b) experimental.

1.2.3. Two-Way Shape Memory Effect

Different from the one-way shape memory effect, it is possible that the material can remember the shape change between low and high temperature phase, such phenomena is called the "*two-way shape memory effect*" (TWSME) where it drives a shape change by only thermal cycling in the absence of applied stress. In order to have the shape change occur, certain martensite variants need to be selected to transform back to the shape in martensite during cooling. However, the selective formation of martensite variants is not an intrinsic property of SMAs, and strong reversibility and lattice correspondence take place in TWSME. Thus, the material requires externally stored energy to help the transformation occur, such as the internal stresses in the microstructure which may

demonstrate shape memory strain under no mechanical loading but by thermal cycling [20]. The TWSME behavior can be achieved by different training sequences [21, 22]. A recent method is to age the material under stress in the martensitic state that TWSME behavior can be observed as well [23]. The two main mechanisms for TWSME are attributed to either residual stresses induced in the matrix by dislocation arrays or on stabilized martensite [24-26].

Thermo-mechanical cycling under compressive and tensile deformation are the most popular methods to develop TWSME. It was reported that complex dislocation arrays can be generated by thermo-mechanical cycling during the training procedure and these dislocations are responsible for the TWSME due to the residual strain from the stress fields [27]. Specifically, if the material is deformed in the martensite phase under tension or compression, then a sufficient heat above A_f would need to be applied to the specimen, followed by cooling to the martensite phase without load, and then repeating of the cycle. If the material is deformed in the austenite phase, then cooling to the martensite phase under load should be carried out, followed by the unloading and reheating of the specimen to the austenite phase, and then repeating of the cycle. Lahoz *et al*.[28] have deformed NiTi SMAs in martensite phase and repeated the thermal cycle between A_f and M_s with and without load, and have concluded that thermal cycling without load is more effective than with load. Inducing TWSME strain also has been studied in austenite phase on CuZnAl shape memory alloys by thermo-mechanical cycling in tension and repeated at least 15 times to get optimum strain [24].

Constrain aging (aging under stress) can form an internal stress field which leads to the TWSME. Solution-treated single crystal $Ni_{51}Ti_{49}$ was compressed along [111]

direction under 300 MPa with 773 K and 6 ks aging, resulting in precipitates formation around the austenite phase [29]. Ni-rich Ni_4Ti_3 precipitates play an essential role in TWMSE, where the internal stress fields that control the growth of the martensite variants, and provides TWSME strain, are produced by these precipitates [30-32]. It has been clearly shown by the TEM results that the oriented strain field around precipitates can cause martensite variants to align in a preferential direction (reoriented martensite), and the stress field created around precipitates can be retained again upon heating to austenite phase [33]. The magnitude of TWSME strain heavily depends on the microstructure change such as dislocation formation, martensite reorientation, and internal stress [31]. Thus, the mechanism of the constrained aging-induced TWSME is clear.

1.2.4. Superelasticity

In addition to the thermo-induced martensitic phase transformation, SMAs can also exhibit phase transformation by applying stress, defined as "*stress-induced phase transformation*". The superelastic behavior of shape memory alloys start at a sufficiently high temperature (above A_f) where the austenite is stable so that the parent phase can transform to martensite under an applied load, shown in Figure 1.6. Figure 1.6a shows the schematic of the structure change between austenite and martensite phases while applying load at temperatures slightly above A_f. Detwinned martensite formed at sufficient stress level and it transforms back to cubic austenite phase once the load is released. Superelasticity is usually represented in the stress-strain curve as shown in Figure 1.6b. At a temperature above A_f, elastic deformation of austenite starts linearly with applied load, and then the stress-induced martensite transformation initiated at a critical stress level of σ^{Ms} and finished at σ^{Mf}. With further loading, the material is fully in martensite phase and

deforms linearly. Upon unloading, the martensite phase starts to transform back to austenite phase at σ^{As} and fully finished at σ^{Af} with an ideally shaped recovery. The total amount of superelasticity strain recovered upon unloading is symbolized by ε_{SE}. The Young's modulus of elasticity for austenite and martensite phases are calculated tangentially and represented by E_A and E_M, respectively.

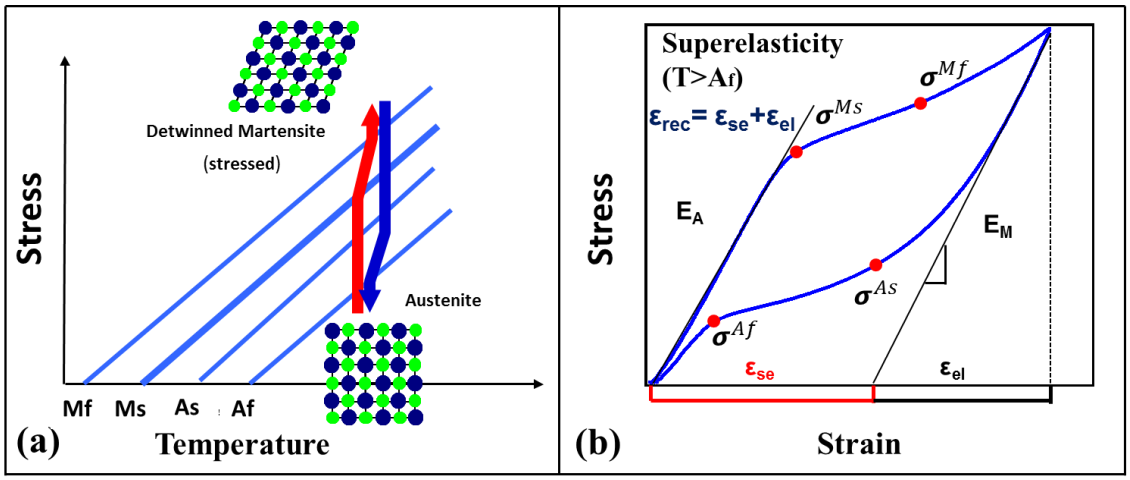

Figure 1.6: A typical schematic of superelastic behavior loading-unloading cycle explained in (a) structure, (b) experimental.

Thus, comparing with the SME which is a consequence of thermal cycling between A_f and M_f, superelasticity is caused by stress-induced martensitic transformation above A_f where the Clausius-Clapeyron (CC) equation can express the stress-temperature dependence of martensitic transformation in SMAs as:

$$\frac{\Delta\sigma(T)}{\Delta T} = -\frac{\Delta S}{\varepsilon_{tr}} = -\frac{\Delta H}{T_0\varepsilon_{tr}} \tag{1.1}$$

Where the $\Delta\sigma(T)$ is the change in critical stress, ΔT is the change in temperature, ΔS is the specific or molar transformation entropy change and ΔH is the enthalpy change. T_0 is the stress-free B2-B19' equilibrium temperature that can be estimated in the usual form: $T_0 = \frac{1}{2}(M_s + A_f)$, and ε_{tr} is the transformation strain. Critical stress for martensite reorientation,

martensitic phase transformation and slip plasticity are strongly temperature dependent as shown in Figure 1.7. Critical stress of SME for the martensite reorientation decreases with temperature due to the increased mobility of internal twins. The black solid-line represents the CC relationship where the critical stress required for martensitic phase transformation increases with temperature. However, superelasticity is only observed if the material is deformed between A_f and M_d, where M_d is defined as the temperature at which no/partial superelasticity can be observed. Plastic deformation of austenite takes place before the stress-induced phase transformation occurs when the testing temperature is above M_d, and the high critical stress for slip decreases with increasing temperature due to the increased plastic deformation.

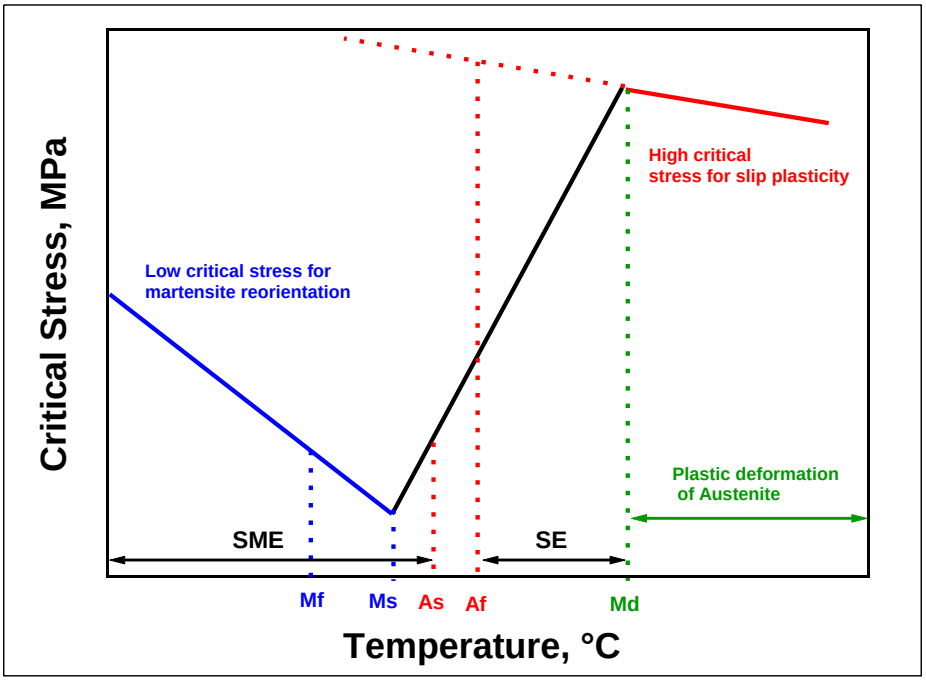

Figure 1.7: Schematic of relationship between critical stress and temperatures in SMAs.

1.3.Background of NiTi-Based Shape Memory Alloys

The shape memory alloy Nitinol (named after Nickel Titanium Naval Ordnance Laboratory) was first discovered in 1959 by William J. Buehler and Frederick E. Wang [34]. As a metallurgist, Buehler discovered the equiatomic nickel-titanium alloy which can produce considerable impact resistance and ductility [35]. The reversible austenite (solid-state parent phase exists in higher temperature regime) to martensite (solid-to-solid shearing phase at lower temperature) phase transition provides unusual properties to SMAs where they can be used in unconventional applications which makes this alloy an exciting research topic for students and scientists [34].

With difficulties in manufacturing (ex. hot working or machining) as well as its expense, getting Nitinol into consumer applications has been a slow and difficult process [36]. Discrepancies between batches of Nitinol impeded the manufacturing of engineering materials, but Buehler and Wang consistently focused on manufacturing process until all imperfections were eliminated [37][38]. In 1969, the first successful Nitinol product came out as couplers for the F-14 fighter aircraft and was also used in similar practical applications in other fields [39]. George B. Andreasen (D.D.S of the University of Iowa) discovered that Nitinol wires have recoverable strain of ten or more times larger than stainless steel which made the alloy a trending material for orthodontic applications [40]. Since then, more applications including actuators, sensors, heat engines, lifting devices, and safety products were introduced [41].

The most well-known shape memory alloy is NiTi because of its ductility and large transformation strains (10 %) which makes it suitable for many commercial applications such as actuators, sealing elements, couplers, stents, biomedical devices, electrical and

mechanical applications in aerospace [1, 2]. However, it is known that TTs of NiTi alloys are usually below 100 °C, and they tend to exhibit low strength and poor cyclic stability [42]. Critical emerging applications of NiTi include micro-electro-mechanical systems (MEMS) have been fabricated to produce functional micro-grippers and micro mirror actuators [43]. Successful use of NiTi in the medical field on surgical tools has provided motivation for more elaborate medical devices which are used in vivo and in vitro conditions [44]. One example of a Nitinol medical device is used to help localize breast tumors and nodules in conjunction with radiology was fabricated as a 'J' hook shape shown in Figure 1.8, the Homer Mammalok ™ [45].

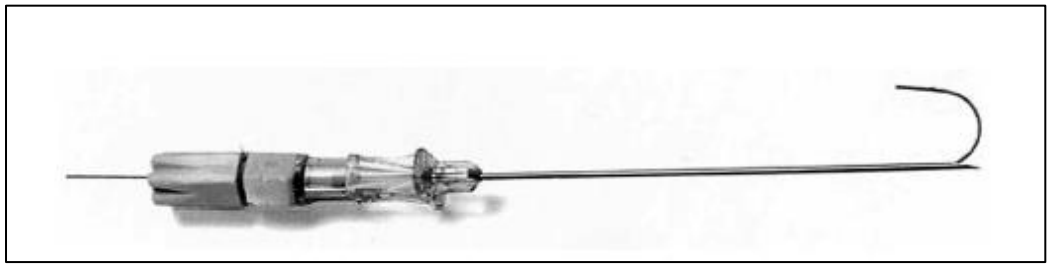

Figure 1.8 The Homer Mammalok ™ Nitinol wire needle localizer [45]**.**

1.3.1. Nickel Titanium Shape Memory Alloys

Near equiatomic NiTi alloys undergo B2 (cubic) to B19' (monoclinic) phase transformation. R-phase exists if there is internal stress in the microstructure due to thermal cycling, and NiTi alloys follow the order of B2—R-phase—B19' transformation [4]. Equiatomic NiTi alloys have low transformation temperatures, low strength and poor cyclic stability [42]. Transformation temperatures of NiTi decrease rapidly when increasing Ni content [4]. However, aging of Ni-rich alloys can improve the strength due to the formation of precipitates.

Ni-rich NiTi shape memory alloys have better superelasticity and shape memory properties when they are compared with near equiatomic NiTi shape memory alloys. High Ni-rich NiTi SMAs are defined if the Ni content is more than 52% [41], in which they show many unique properties such as good corrosion resistance, high toughness, and lower density (an excellent candidate for aerospace and motor industries) than steel. Aging effect of highly Ni-rich $Ni_{54}Ti_{46}$ was revealed on microstructure and shape memory properties by Karaca et al. [5]. In their study, shape memory effect was observed even under an extremely high stress level of 1500 MPa without any prior training in all aged samples, and a very small temperature hysteresis of 8˚C was also obtained for 3 hours of aging at 450˚C. Figure 1.9 shows isothermal stress-strain behavior of four aged materials of Ni-rich $Ni_{54}Ti_{46}$. It has been observed that all aged samples have the perfect superelastic behavior at room temperature except the 600˚C-3h aging specimen. It should be noted that the $Ni_{54}Ti_{46}$ alloy with 500 °C 3hr aging exhibits the superelasticity with a recoverable strain of 2.5 % under the ultra-high stress level of 2100 MPa without any prior training.

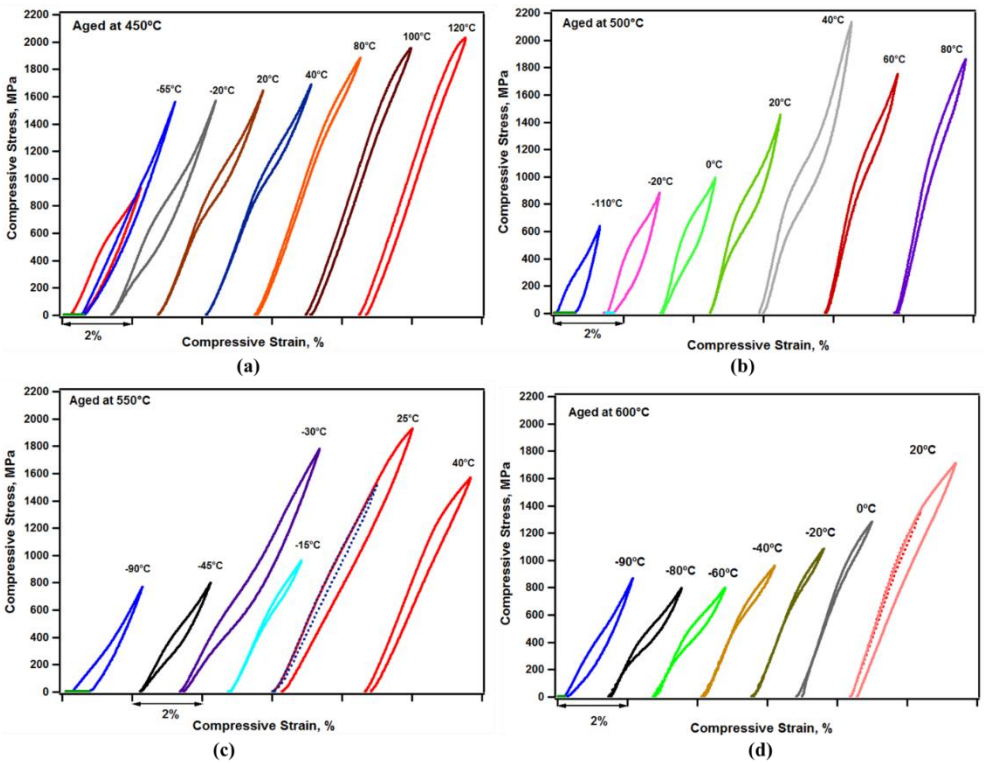

Figure 1.9: The compressive stress-strain response of Ni-rich $Ni_{54}Ti_{46}$ aged samples as a function of temperature [5].

Another important research topic of NiTi alloys was developed on single crystals since the shape memory (transformation strain, hysteresis, CC slopes) and material properties (critical stress for slip, ductility) of SMAs are highly dependent on orientation and heat treatment [46-48]. Figure 1.10 shows the compressive stress-strain responses of aged $Ni_{50.8}Ti_{49.2}$ single crystals in selected orientations [6]. Various correspondent variant pairs (CVPs) were activated during stress-induced martensite transformation in [111] and [112] orientations while only one active CVP was found in [148] orientation. High CVP activation will result in high hardening in the transformation region [46]. Thus, orientation [111] and [112] quickly reach the critical stress for plastic deformation due to high hardening while [148] orientation performs a plateau-like transformation due to the low

hardening. The highest recoverable compressive strain of 9 % was observed along the [148] orientation.

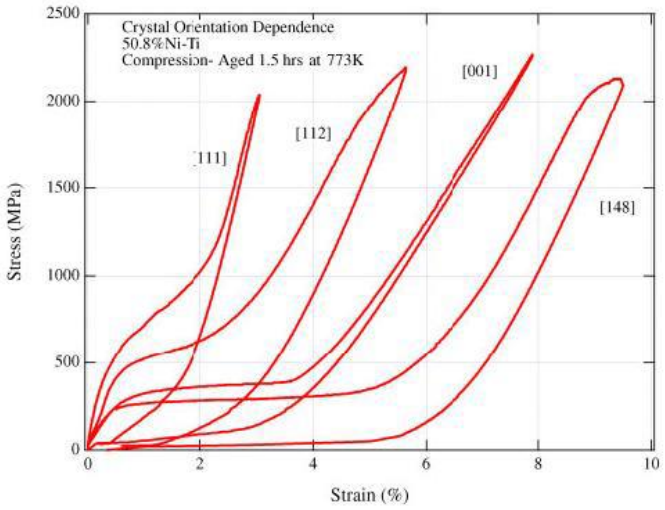

Figure 1.10: Orientation dependence of stress-strain behavior of $Ni_{50.8}Ti_{49.2}$ alloy [6].

Shape memory behavior of $Ni_{51}Ti_{49}$ alloys along with [001], [011] and [111] crystallographic orientations were studied on both homogenized and aged specimens [49]. 1000℃ for 2 hours homogenization was applied to NiTi single crystal and subsequently with an aging of 500°C for 1.5 hours to form precipitates. TTs of homogenized $Ni_{51}Ti_{49}$ single crystal alloy were; M_s = -52°C, M_f = -68°C, A_s = -37°C, A_f = -23°C, and the TTs of aged (500°C 1.5h) $Ni_{51}Ti_{49}$ single crystal alloy were; R_s = 25°C, R_f = 16°C, M_s = -7°C, M_f = -16°C, A_s = 27°C, A_f = 33°C. A perfect shape memory behavior and very narrow temperature hysteresis of 10˚C were observed under the high stress level of 1500 MPa in [001]-oriented aged sample which can be attributed to the high strength of the precipitation-hardened single crystal due to a high density of precipitates [49]. The other two orientations ([011] and [111]) show very low strength compared with [001]. In addition, the stress-strain curves of the aged single crystals along the [001], [011], and [111] orientations were reported at selected temperatures shown in Figure 1.11, and it can be seen that only [001]

orientation shows perfect recoverable superelasticity above room temperature with a total strain of 7 % at high temperature. The other two orientations show relatively weak shape memory properties.

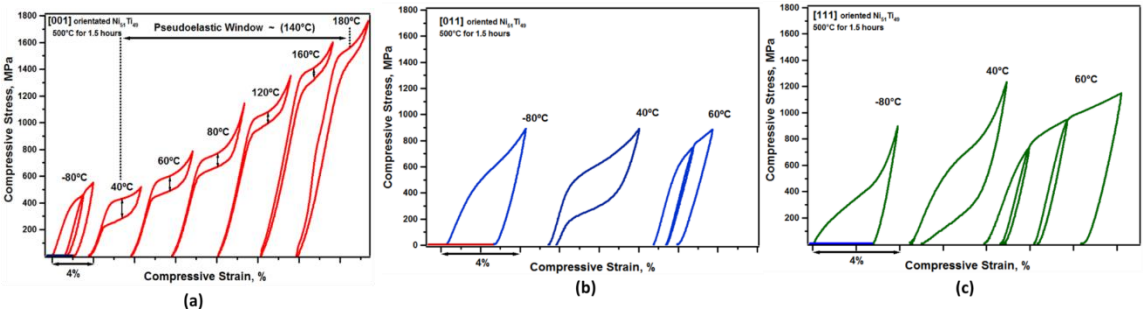

Figure 1.11: The compressive stress-strain response of aged $Ni_{51}Ti_{49}$ single crystals as a function of temperature [49].

1.3.2. Ni-Rich NiTiHf Alloys

Transformation temperatures play an important role on designing SMA products, such as some applications on the core region of an aircraft engine or downhole applications in the oil industry require SMAs with high transformation temperatures (>100˚C) [6]. Thus, NiTi alloys are no longer being considered. In order to obtain high temperature shape memory alloys (HTSMAs), chemical alloying methods have been used to change the TTs of NiTi shape memory alloys. Improved mechanical and functional properties such as transformation strain, oxidation resistance, resistance to plastic deformation can be found at high operation temperatures [6]. Addition of Fe, Al, Co Cu (replacing Ni content) reduces TTs while addition of Hf, Zr, Pd, Pt, Au (replacing Ti content) increase TTs of NiTi alloys [6]. Zr and Hf additions were the best candidates to increase the transformation temperatures of NiTi due to their low cost compared with Au, Pd and Pt [7]. Mechanical properties of these two alloy systems are very similar. Figure 1.12 shows the composition dependence of the martensitic peak temperature M_p as a function of the alloy content.

Figure 1.12a shows that the TTs are insensitive to the Hf content of up to 3 % , and it starts to increase at 5 %. There is an increase by 5 ˚C/at % up to 10 % of the Hf content and then with a rate of 20 ˚C/at % up to 25 % of the Hf content (M_p is 400 ˚C). The change of M_p is similar in NiTiZr system where is starts to increase at 10 % of Zr content with a rate of 10 ˚C/at % and reaches to 250 ˚C at 20 % of the Zr content shown in Figure 1.12b. Therefore, it can be concluded that the Hf system is more effective in changing the TTs compared to Zr system.

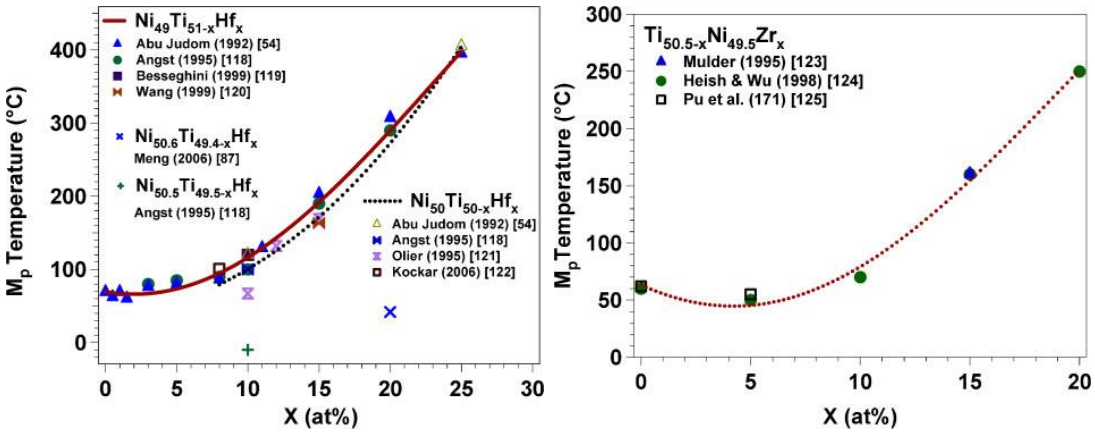

Figure 1.12: Composition dependence of the martensitic peak temperature Mp, as a function of (a) hafnium content in NiTiHf system, (b) Zr content in the NiTiZr alloy system [6].

Composition of $Ni_{49.8}Ti_{50.2-x}Hf_x$ (x=8, 9.5, 11, 15, 20) have been investigated and it was revealed that transformation temperatures increase with increasing the Hf content [8]. Moreover, a systematic aging study of Ni-rich $Ni_{50.3}Ti_{29.7}Hf_{20}$ polycrystalline alloys revealed that the 600˚C-3h aging can increase the martensitic transformation temperature from 120 ˚C to 160˚C [9]. Perfect superelastic behavior with 3% transformation strain was also observed on 550˚C-3h aging at a high temperature of 240˚C shown in Figure 1.13b.

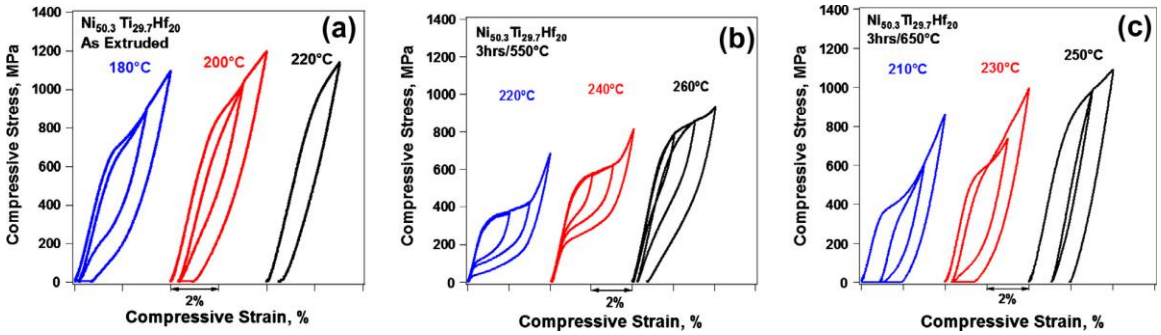

Figure 1.13: Superelastic behavior for the $Ni_{50.3}Ti_{29.7}Hf_{20}$ alloy as a function of temperature, (a) as-extruded, (b) aged 550 ˚C-3h, (c) aged 650 ˚C-3h [9].

Additionally, the shape memory and mechanical properties of Ni-rich NiTi alloys are highly orientation and thermal treatment dependent. Solutionized, 550 °C-3h and 650 °C-3h aged $Ni_{50.3}Ti_{29.7}Hf_{20}$ alloys were investigated under mechanical compressive testing along three selected crystallographic orientations of [001], [011], and [111] [50]. The 550 °C-3h aging introduced coherent precipitates with nano size of 20 nm in the matrix which substantially improved the shape memory and mechanical properties, while the 650 °C-3h aging results in the precipitates coarsened in size between 40-60 nm. Karaca et al. had also observed that $Ni_{50.3}Ti_{29.7}Hf_{20}$ single crystalline alloys along the [111] orientation under the 550 °C-3h aging has good shape memory behavior with 3 % recoverable strain under high strength levels (1000MPa) and perfect superelastic behavior with 5 % recovery at 200 ˚C. [001] oriented single crystals show the highest strength (1500 MPa) during thermal cycling without any plastic deformation. The ultrahigh work output of 30 J cm^{-3} was also reported [51].

1.3.3. NiTiHf –X (X= Cu, Pd) Alloys

Previous review shows that NiTiHf alloys are promising for high temperature applications. However, low strength and high brittleness constraint their practical

applications [9]. Thus, quaternary elements (Nb, Cu, Pd) have been added to NiTiHf shape memory alloys aiming to improve their shape memory and material properties.

Cu was added to NiTiHf in order to improve the thermal stability, but it was found to decrease TTs [52, 53]. Karaca el al. reported shape memory behavior, TWSME and superelastic properties after addition 5% Cu was replaced with Ni of $Ni_{50.3}Ti_{29.7}Hf_{20}$ [54]. In their study, $Ni_{45.3}Ti_{29.7}Hf_{20}Cu_5$ alloys show compressive shape memory strain of 2 % under 700 MPa above 100 ˚C and 0.8 % two-way shape memory strain above 80 ˚C. However, there is no superelastic behavior shown in this study due to high hardening and hysteresis which shown in Figure 1.14

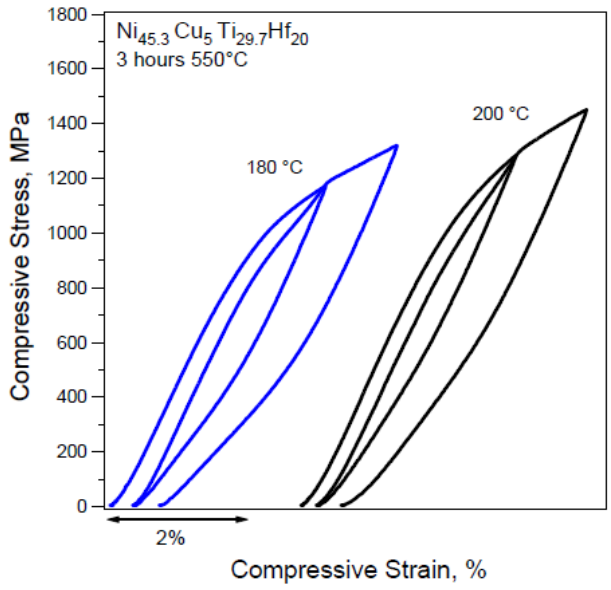

Figure 1.14: Stress-strain response of Ni45.3Ti29.7Hf20Cu5 alloys aged at 550C-3 hours [66].

By adding Pd to NiTiHf, a unique composition $Ni_{45.3}Ti_{29.7}Hf_{20}Pd_5$ was created by Karaca et al. [13]. Figure 1.15a is the superelastic tests of as received specimen which shows a full strain recovery without any plastic deformation under an extreme high stress

level of 2 GPa. Compressive stress-strain curves for the specimen aged at 400°C-3h are shown in Figure 1.15b. Perfect superelastic behavior is obtained in up to 90°C with a recoverable strain of 4 %. No irrecoverable strain is observed of superelastic behavior specimen aged at 550°C-3h which is portrayed in Figure 1.15c, and the work output is smaller than the specimen aged at 400°C-3h. There is no full strain recovery in Figure 1.15d for specimen aged at 650 °C. This unique polycrystalline alloy also presents a very high damping capacity (30-34 J cm^{-3}), high work output (30-35 J cm^{-3}) and high mechanical hysteresis (900MPa) which could lead to applications for high stress operating systems in civil engineering to reduce the damages from earthquakes.

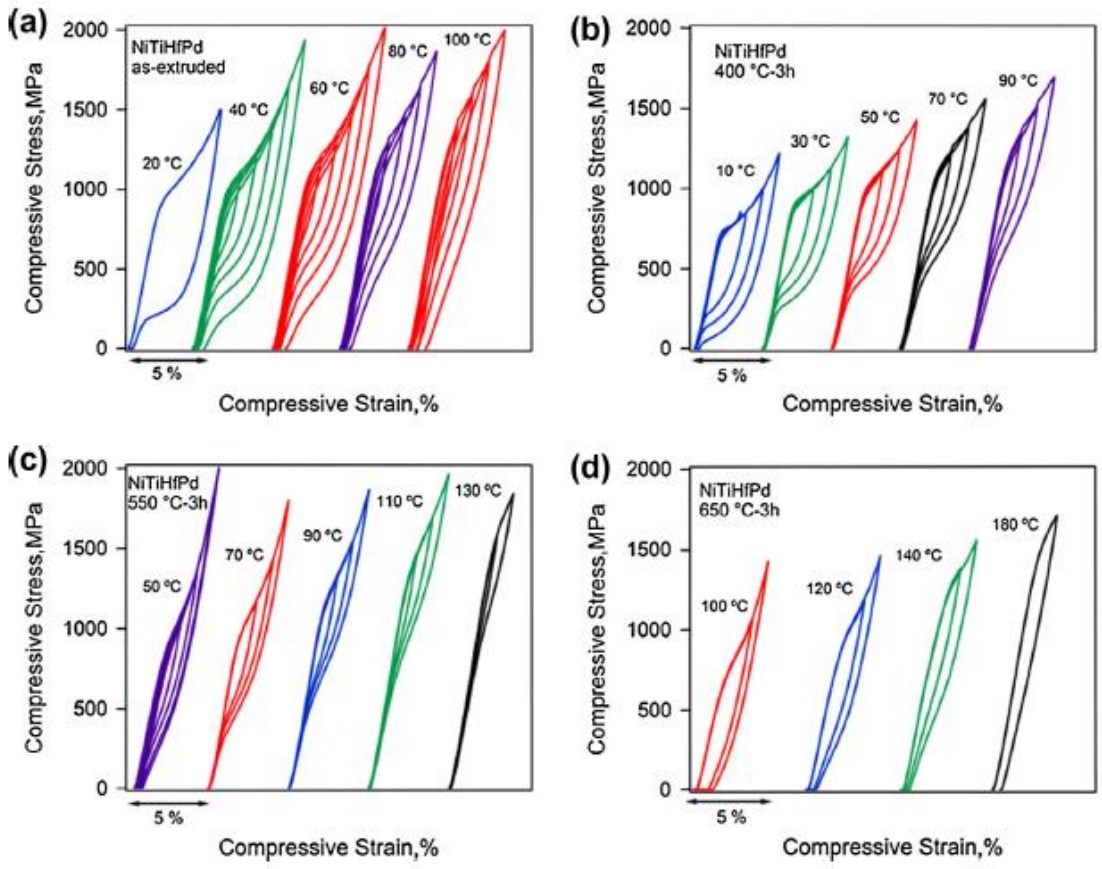

Figure 1.15: Isothermal stress-strain curves for polycrystalline NiTiHfPd (a) as-extruded, (b) aged at 400°C for 3h, (c) aged at 550°C for 3h, and (d) aged at 650°C for 3h demonstrating superelastic behavior [13].

2 LITERATURE REVIEW OF INDENTATION

2.1.History and Overview of Indentation.

In October 1877, at the age of twenty, Heinrich Hertz decided to focus on engineering studies as his profession when the ‘Study of Natural Science” delighted him. Later in the 1880’s, Hertz first investigated the hardness of glass by pressing a hard steel lens to mirror glass, and the beautiful cone-shaped fractures produced in contact between glass lenses [55]. Since Hertz developed the study on contact of elastic solids, indentation mechanics has been popularly used in order to analyze and characterize the fracture and deformation properties of brittle ceramics, metals and other materials [56].

In the period of 1950-1970, Hertzian cone cracks have been extended from hard steel or tungsten carbide to other brittle solids as well as single crystals (especially with the diamond structure) and fine-grain ceramics [57]. With many refinements and reinventions including the Auerbach’s law, Griffith-Irwin fracture mechanics analysis and Oliver-Pharr analysis method [58-60], instrumented indentation techniques have been developed to extract mechanical properties of materials from loading-unloading curves (materials hardness, elastic modulus and stress-strain relationships).

With the discovery of shape memory effect (SME) and superelasticity (SE), the design of shape memory alloys (SMAs)-based micro-electro-mechanical systems (MEMS) and elaborate medical devices have attracted tremendous attentions on the characterization of material performance on small-scale system instead of bulk materials. The reliability of MEMS is determined by the mechanical properties, but also by the size effect and surface effect where their mechanical properties at small-scales may differ from the bulk size [61-63]. Consequently, tools that can quickly and accurately interpret the mechanical properties

on small-scale materials are required to be assembled [3]. Owing to the nature martensitic phase transformation behavior of SMAs, it has been utilized as the bacteriophage T4 virus at nanoscale, where an outer lattice of protein crystals undergo the martensitic phase transformation and provides the uniaxial force in order to deliver foreign DNA to the inner tube [64]. Furthermore, the nucleation and propagation of the martensitic phase transformation behavior shown in micrometer to meter length of NiTi alloys were also investigated on the nanometer scale to reveal the stress-induced martensitic transformation [65], yielding the insight of the necessity for nano/micro scale sized SMA actuators. One method to extract small-scale mechanical properties of ductile or brittle materials was introduced by the instrumented indentation techniques.

2.2.Contact Mechanisms

Indentation testing is a simple method of consistently touching the unknown material by using an indenter whose material properties such as elastic modulus and hardness are known [66]. The analysis of the depth of the impression, in conjunction with the loading-unloading characteristics, were used to determine the mechanical properties. Most indenters are made of diamond due to its high hardness, but it should be kept in mind that it is also very brittle and can be easily damaged. 1000 GPa modulus value of diamond is often used for analyzing nano-indentation data with a Poisson's ratio of 0.07. Indenters may be spherical, pyramidal (e.g. Berkovich), Vickers, rigid conical or even flat-ended cylindrical punches. Spherical indenters are preferred over other sharp indenters due to the non-uniaxial stress fields underneath the indenter and the onset plasticity upon indentation is delayed when the material is subjected to a spherical indenter. In recent years, spherical

indentation techniques have been considered as a standard method of measuring the hardness of materials [66-68].

In the early 1970's, Bulychev, Alekhin , Shorshorov, and co-workers [69][70] started to measure elastic modulus by using instrumented micro-hardness testing machines (Vickers) to obtain indentation load-displacement data as shown in Figure 2.1b. h_f is the final depth, h_c is the contact depth and h_{max} is the maximum indentation depth while the maximum load P_{max} was applied. The stiffness S=dP/dh was measured on the upper portion of the unloading data. A simple illustration of the unloading process in Figure 2.1a shows contact geometry which can determine the contact area between indenter and specimen. Once it is determined, hardness value can be estimated from $H=P_{max}/A_c$, where the A_c is the projected contact area. For a Berkovich/Vickers equivalent cone (α=70.3°), the projected contact area is given by:

$$A_c=\pi\, tan^2\alpha\, h_c^2=24.5h_c^2 \quad (2.1)$$

The contact modulus is considered as the Young's modulus (E) of samples where it can be related with the reduced modulus (E_r) and the elastic constant of the diamond indenter, commonly defined as (2.2)

$$\frac{1}{E_r}=\left(\frac{1-\upsilon^2}{E}\right)+\left(\frac{1-\upsilon_i^2}{E_i}\right) \quad (2.2)$$

where E_i = 1000GPa and ν_i = 0.07 for the diamond indenter. E and υ are the Young's modulus and Poisson's ratio for the specimen, respectively. Equation (2.2) is often used in finite modeling in both Berkovich and spherical contacts. The first improved method of measuring contact areas, hardness, and elastic modulus by instrumented indentation techniques was introduced in 1992 by Oliver-Pharr, known as Oliver-Pharr method, it has

widely been used to characterize the small-scale mechanical properties [60]. Microstructure of monocrystalline silicon has been analyzed after using Berkovich and spherical indenters, and it was found that deformation zones created by these two indenters have very different phase distribution characteristics [71].

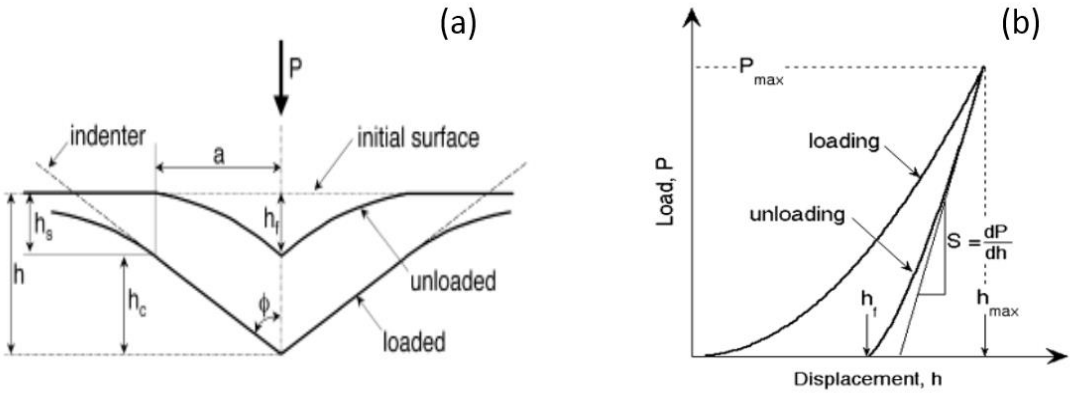

Figure 2.1: Schematic illustration of the unloading process showing parameters characterizing the contact geometry with (a) a Vickers indenter, (b) indentation load-displacement data [72].

Spherical indentation contact problems are of special interest due to the relationship to the present work. In order to understand how elastic-plastic specimen behaved while loading with a spherical indenter, a schematic was shown in Figure 2.2b. Upon initial loading, only a small portion of elastic deformation occurs at low loads followed by an elastic-plastic deformation during high load region, and the elastic unloading is initiated once load is removed. Indentation hardness is calculated at the maximum indentation depth and indentation modulus is analyzed from the unloading curve where it can be determined as the tangent. Figure 2.2a shows the contact geometry of a rigid spherical indenter. The full penetration depth made by a rigid spherical indenter is h_{max} at maximum load P_{max}

where the elastic depth recovery is presented as h_e which results in a residual impression depth h_r, and a is the radius of project area.

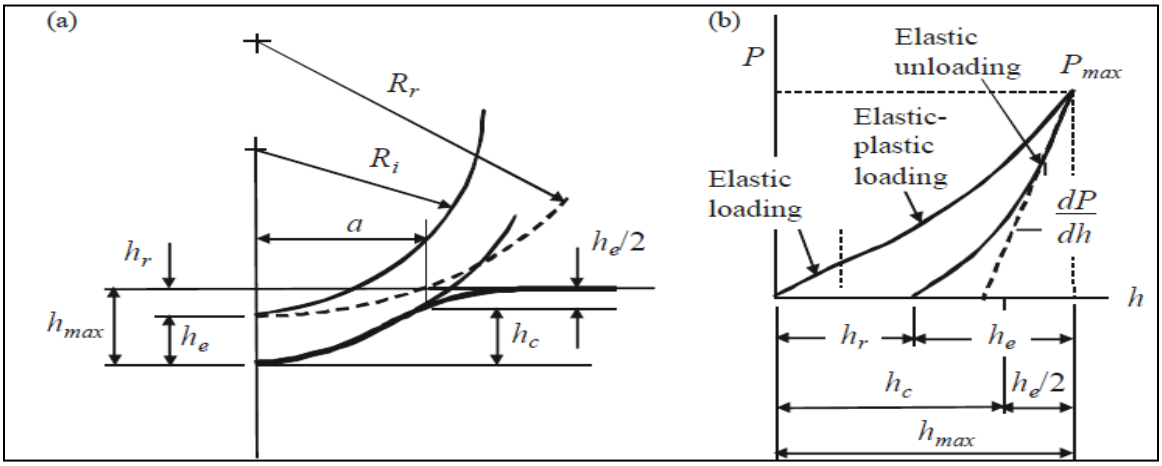

Figure 2.2: (a) Contact geometry of a spherical indenter with a tip radius of R_r, (b) corresponding load-displacement curve for an elastic-plastic specimen loaded with a spherical indenter [66].

A study on elastic-plastic stress distribution behavior under a spherical indenter revealed the distribution of pressure and load by using experimental and finite element methods in 1997 [73]. A mild steel material (E/Y=550) was tested under an indenter with a radius of 3.18 mm, shown in Figure 2.3a, a top view of 1000 N load shows the residual impression in the surface, and Figure 2.3b is the corresponding cross section view of subsurface beneath the indent. In Figure 2.3c, finite element analysis reveals that stress distribution is modified and became more uniform when plastic deformation occurs. Figure 2.3d shows the evolution of the plastic zone compared with experimental results.

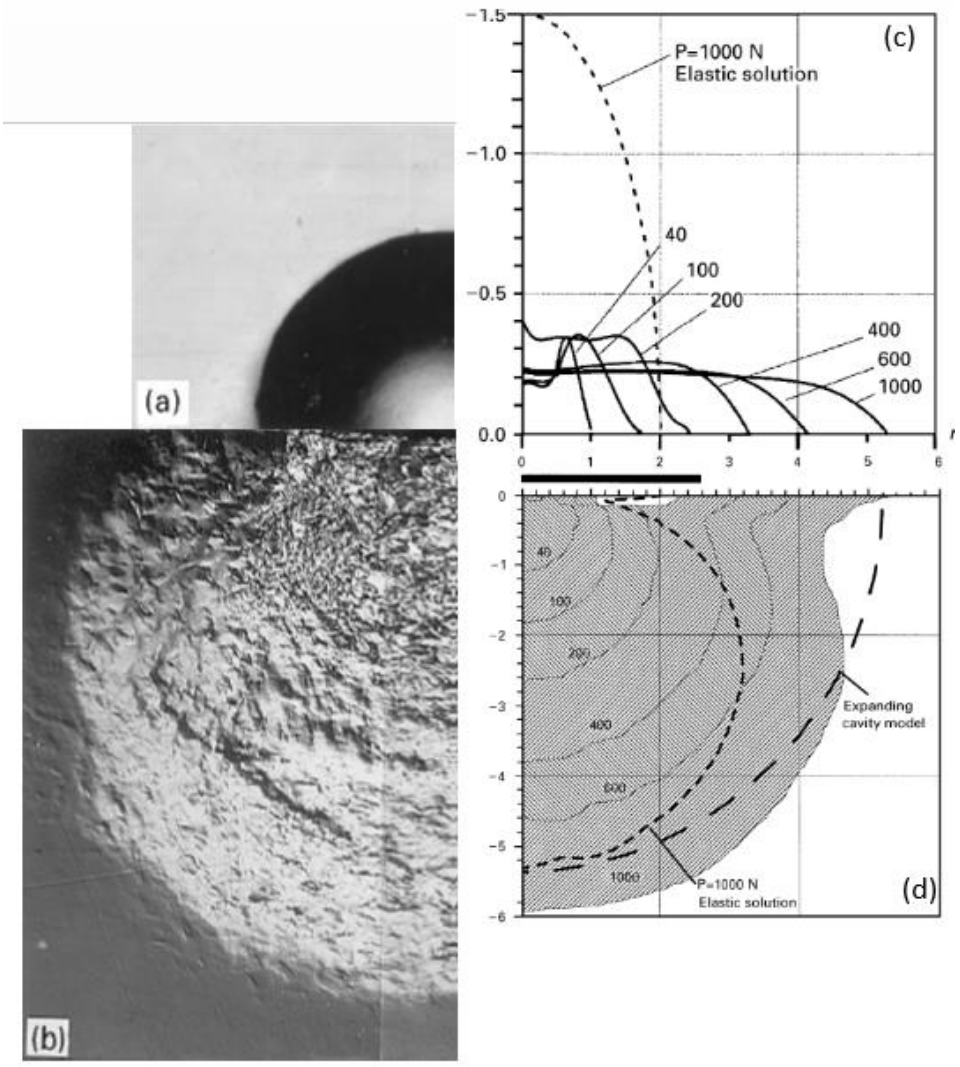

Figure 2.3: Elastic-plastic indentation response of a mild steel material, (a) Top view of residual impression in the surface, (b) Cross section view of subsurface underneath indent, (c) Finite element results of pressure distribution, (d) Finite element results of plastic zone distribution [73].

The elastic contact problem of a sphere pressed by an applied load against an elastic half-space was solved analytically by Hertz [55]. For the contact model of a rigid sphere into an elastic-plastic, Johnson has proposed a semi-analytical spherical cavity model to explain the elastic-plastic indentation process [74]. Detailed finite element analysis of the spherical indentation on elastic-plastic solids confirmed and showed good agreement with the experimental correlations of work hardening materials using the representative strain

[75]. A numerical derivation then was also observed to explain the relationship between these mechanical properties in 1997 by Cheng [76]. Later in 1999, fully elastic-plastic contact of a spherical indenter includes elasticity, strain-hardening, and interfacial friction have been reported by Mesarovich and Fleck [77]. Numerous refinements and reinventions were brought out to understanding the mechanics of elastic-plastic contact as well as the loading and unloading curves, and an update of getting the most accurate mechanical property measurements was also reviewed in 2003 [72]. Indentation hardness and Young's modulus can be obtained from the peak load and the initial slope of the unloading curves by the method of Oliver and Pharr [60] or Doerner and Nix[78]. Both of these methods, and most of the previously proposed methods, depend upon estimating the contact area under peak load. However, it becomes difficult when "piling-up" or "sinking-in" occurs around the indenter. A scaling approach to spherical indentation in elastic-plastic solids with work hardening reveals an approximate relationship between the ratio of hardness to elastic modulus (H/E) and the ratio of irreversible work to total work (W_{irr}/W_t). By extending this relationship, it is possible to circumvent this difficulty (piling-up) of estimating the contact area by using an energy-based method from instrumented spherical indentation experiments, which was proposed and validated on copper, aluminum, tungsten and fused silica [79].

2.3.Indentation in Shape Memory Alloys

Superelasticity and indentation behavior of NiTi was investigated to prove that superelasticity exists not only under bulk testing but also during instrumented indentation tests. The higher performance of superelasticity with the large recoverable depth of NiTi alloys was shown by Liu et al. [11]. Indentation-induced superelasticity was also observed

under complex loading conditions with two selected diamond indenters (spherical and pyramidal) [12] as shown in Figure 2.4. Non-dimensional analysis and indentation depth recoverable ratio as a function of depth under Berkovich and spherical indenters were also shown in Figure 2.4. Depth recovery ratios of 95% and 45% were observed for spherical indenter (2.75 N load) and pyramidal indenter (200 mN load), respectively. It was also revealed that superelasticity can be detected much easier by using a spherical indenter rather than pyramidal indenter. There are several publications which also observed the indentation-induced shape memory and superelastic effects in NiTi thin films [80-82]. Specifically, shallow spherical indents in austenite NiTi specimen can fully recover upon unloading, but indents in martensite only partially recovered while full recovery occurs upon heating to austenite phase.

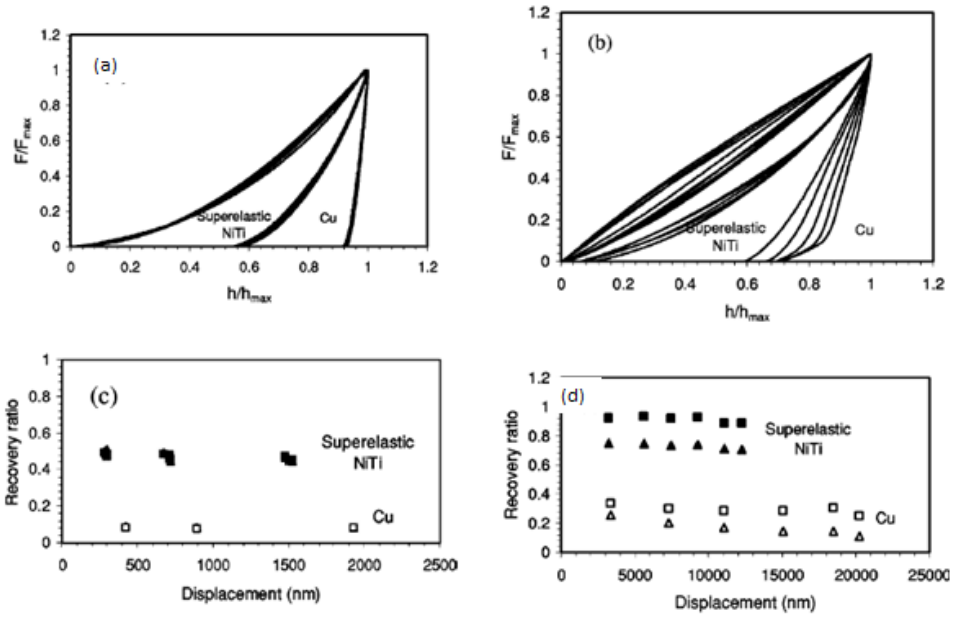

Figure 2.4: (a) Dimensionless load-displacement curve under Berkovich indenter, (b) dimensionless L-D curve under spherical indenter, (c) recovery ratio under Berkovich indenter, and (d) recovery ratio under spherical indenter [12].

Experimental indentation testing using a spherical indenter revealed the "self-healing" effect [14], where Figure 2.5 explains the shape change upon heating to austenite phase. This behavior can also be well explained as the shape memory effect. As shown in Figure 2.5, spherical indents were made in a martensitic NiTi alloy with a tip radius of 213.4 μm spherical indenter at various loads, and corresponding indentation depths were measured with three-dimensional profiles. Results show that the indents on the surface vanished after applying heat to the specimen over 120 °C ($T>A_f$) attributes to the shape memory effect. Similar experiments were also studied under Berkovich and Vickers indenters, where only partial depth recovered upon heating above A_f [80].

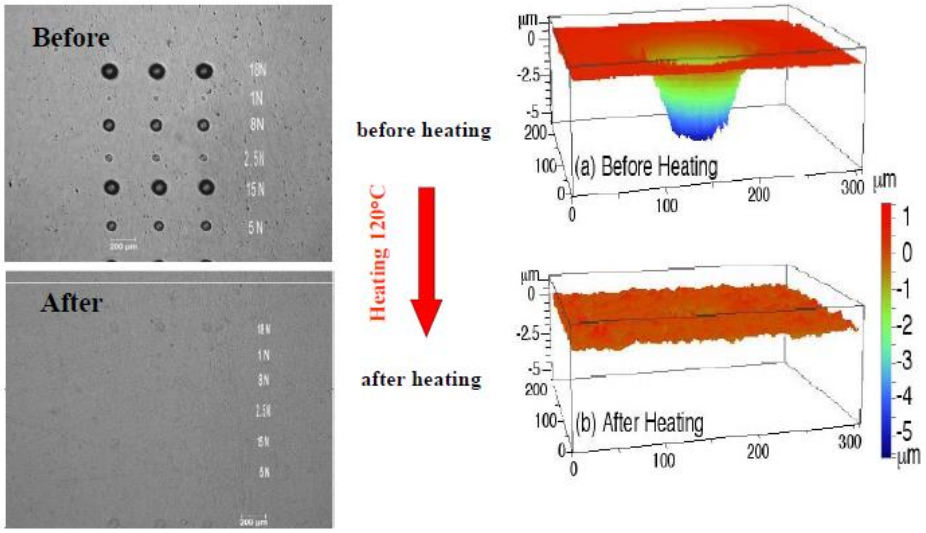

Figure 2.5: Microscopic shape memory effect: spherical indentation in the martensitic NiTi shape memory alloy [14]**.**

Theoretical indentation-induced shape memory and superelastic effects are difficult to achieve due to the plasticity under complex contact loading conditions. Numerous one-dimensional constitutive models have been announced on shape memory alloys [83-85].

One of the famous one-dimensional phenomenological continuum models that simulated both SME and SE is the Ivshin-Pence model [85]. There are also several proposed three-dimensional models for superelastic shape memory alloys [86, 87]. However, these models have been limited to uniaxial loading. Zhang et al. have developed a three-dimensional constitutive model of shape memory alloys with plasticity and uniaxial loading where a simulation of spherical indentation-induced superelasticity in NiTi shape memory alloy was carried out and compared with the experimental result data [88]. Figure 2.6a illustrates three sets of data, the experimental load-displacement data was obtained from Ni et al. [12], and the other two sets of data were created by using two modeling materials (SE1 and SE2). It can be seen that both simulated loading-unloading data match with experimental data very well. Figure 2.6b has a full depth recovery in the SE 1 model only when representative strain is lower than 1.5%, which indicated adjustments were needed to be optimized. Owing to the unique shape recovery phenomenon, deformation of superelastic NiTi alloy made by a spherical indenter is nearly fully recoverable upon heating, while impressions formed by a pyramidal indenter is only partially recovered [14].

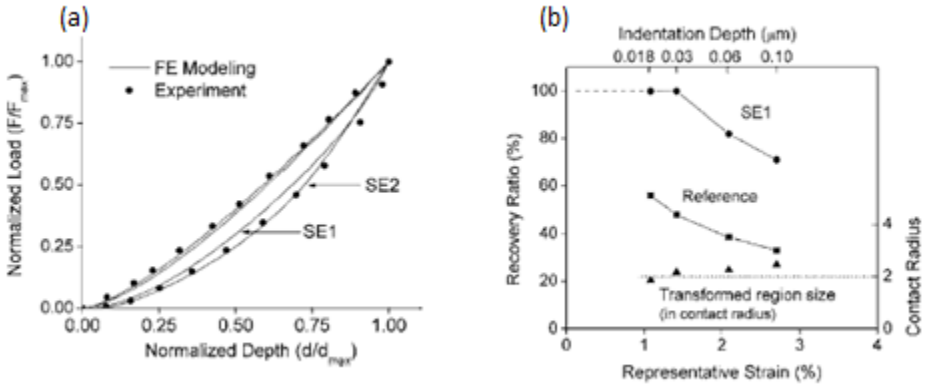

Figure 2.6: (a) Comparison of experimental and FE modeling, (b) recovery ratios vs representative strains at different depths [88].

2.4.Indentation-Induced TWSME

An indentation study with sharp Vickers indenter of a NiTi alloy that can induce two-way shape memory effect (TWSME) reported that all indents become piled-up and show the TWSME even after 10 thermal cycles. With an indentation load of 1000 mN, the volume change in the TWSME is up to 50 μm^3 and recovery ratio of TWSME can be up to 14%, which might be useful as micro-pumps and micro-actuators [89]. Another study on the TWSME of NiTi alloys was discovered by using a spherical indenter, which produced a reversible two-way indent depth change of 45 % total depth. This behavior can be used to make reversible surface roughness, texture, and morphology applications [90]. Figure 2.7a describes the repeatable depth change behavior. Starting with the zero thermal cycle, an indentation depth of -170 μm was measured at martensite phase and it decreased to -80 μm while heating to A_f. Further cooling to martensite phase results in a new indentation depth of -140 μm which was stabilized with further thermal cycling training. As a consequence, the indent depth change ratio stayed constant under thermal cycles shown in Figure 2.7b.

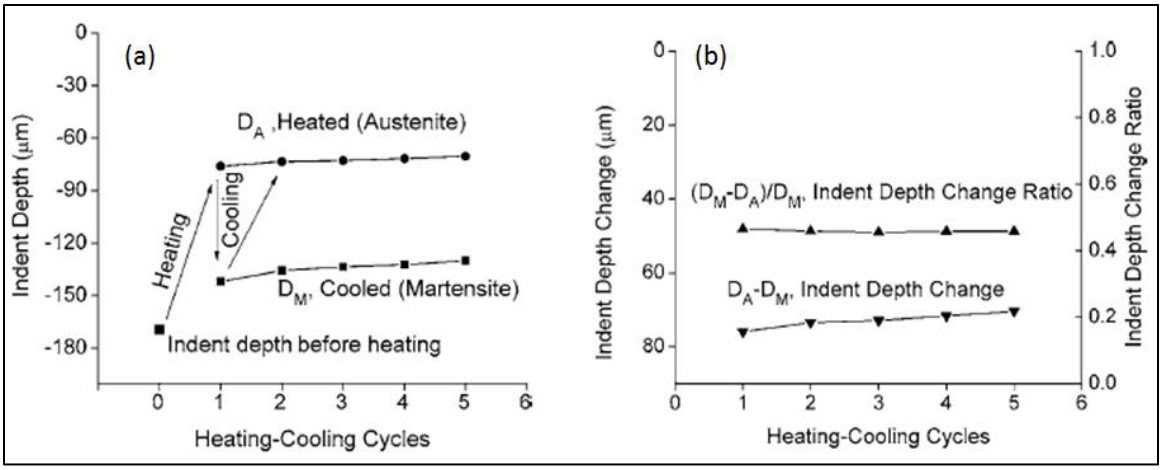

Figure 2.7: Two-way indentation depth change (a) over 5 thermal cycle, (b) indentation depth change ratio and absolute depth change [90].

An advanced study created the "surface form memory" by utilizing TWSME and planarization methods. Fei et al. explained the phase deformation underneath the spherical indenter upon thermal cycling [15]. Figure 2.8 presents a trained two-way shape memory alloy experiencing thermal cycling step by step after the initial indent was formed in the martensite phase. Step (a)-(c) exhibit TWSME, perfect polishing was made until the indent just disappears at the martensite phase (e). Once the polished specimen was subjected to heat (T>Af), a positive indentation depth (protrusion) generated on the surface due to the internal stress-assisted shape change.

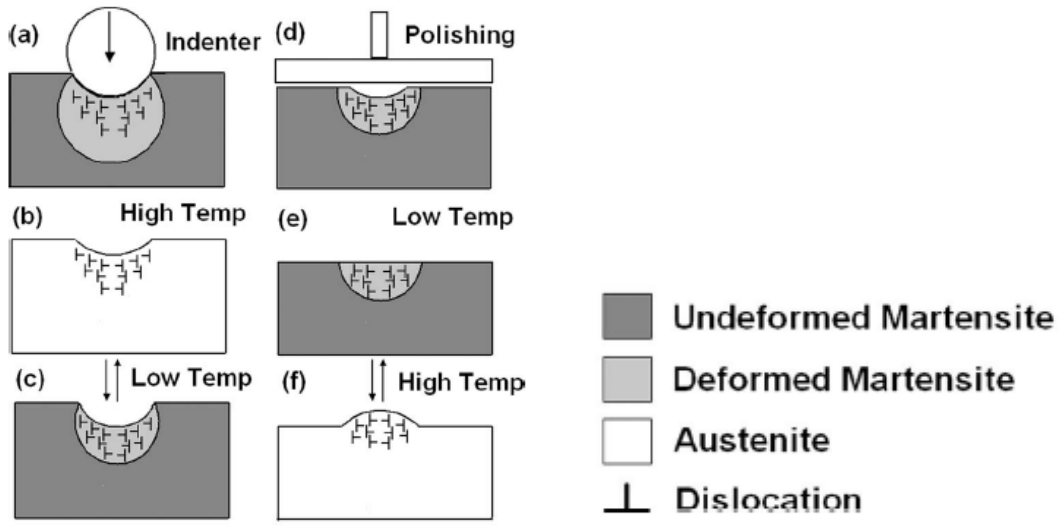

Figure 2.8: Indent training (a-c) and planarization (d) thermal cycling to obtain surface form memory effect (e-f) [15].

Such an invention of SFM has the ability to generate transitions in surface form that can be normalized to a planar state at the same time and also against very high reaction forces, suggesting such an effect can be applied to MEMS actuators, lithography, joining, tribological system, micro-assembly, and even electrical switching devices. This effect may be obtained either from macro/nano scale indents made quasistatically, or by indenting in the dynamical regime using shock waves from laser ablation [15]. Laser Shock Peening (LSP) has been introduced by making indents with shock waves generated by laser ablation of a metal foil on the surface of NiTi alloys. With a 5 ns laser pulse at an intensity of 2.5 GW/cm2 and a beam size of 0.5 mm, indents were made on a 3 mm thick 50.26 at.% NiTi has also been studied on SFM effect using the same procedures as mentioned above. Three-dimensional surface profiles of the indent surface with different temperatures were acquired with a WYKO NT 1000 optical profilometer and shown in Figure 2.9. Figure 2.9a exhibits the shape memory mechanism by recovering 4.9 μm depth from initial indent depth of 5.7 μm (85.9 % shape recovery) and the TWSME upon cooling with a 24.6 %

depth change before planarization. After mechanical grinding of the indent, a positive extent with amplitude of 1.2 μm was observed in Figure 2.9b with inserted 3-D profiles for the thermally reversible and cyclically repeatable protrusion. It was also conclude that the LSP method of producing SFM amplitudes is about five times greater than the quasistatic indentation using spherical indenters [15].

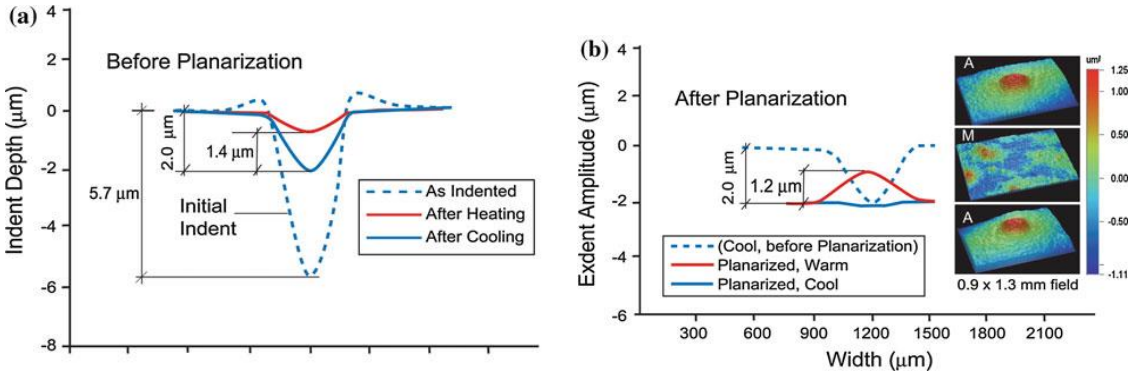

Figure 2.9: Depth measurements of (a) initial indent depth-recovery, and (b) extent-to-flat surface transition during heating and cooling after planarization of the LSP indent [15].

2.5.High Temperature Indentation

Previous nano-indentation studies on SMAs were mostly conducted at room temperature to determine indentation hardness, depth recovery ratio and superelasticity [12, 14, 91, 92]. Recent advances in high temperature indentation instrumentation have stimulated a broad interest in the indentation response of materials over a wide temperature range. In 1995, Poisl et al. performed elevated-temperature nano-indentation by placing a commercial nano-indenter in a temperature-controlled room which could be heated from room temperature to 34 ºC [93]. Later, Suzuki and Ohmura built an optimized high temperature (up to ~ 600 ºC) indentation instrument with a fast heating rate which affects the sensitivity during testing [94]. Commercial indentation equipment was developed to

overcome sample oxidation and system thermal drift, allowing both nano- and micro-indentation measurements up to 750 °C.

High temperature nano-indentation measurements have been conducted on many alloys such as fused silica [95-98], aluminum [97], Titanium [96], copper [97], and Ni-based super alloys [99]. A number of researchers also studied NiTi at elevated-temperatures [82, 100-103]. Both spherical and Berkovich indenters were used for the high temperature nano-indentation study over a range of up to 200 °C [100]. It was found that spherical indenters are more suitable than sharp indenter tips of characterizing shape memory properties. Figure 2.10a represents the load-depth curves at different temperature, and it shows that the maximum indentation depth is temperature dependent. The remnant indent depth ratios (depth after unloading/depth at peak load) were measured as a function of temperature for NiTi alloys under a spherical indenter shown in Figure 2.10b, and it was found that the relative low remnant indent depth ratio is indicative to the occurrence of superelasticity [100] where the sharp drop in this ratio was observed around A_f. Further study with finite element simulations were consistent with the observed experimental results although there were some discrepancies regarding the load-depth curves for the superelastic cases in NiTi alloys.

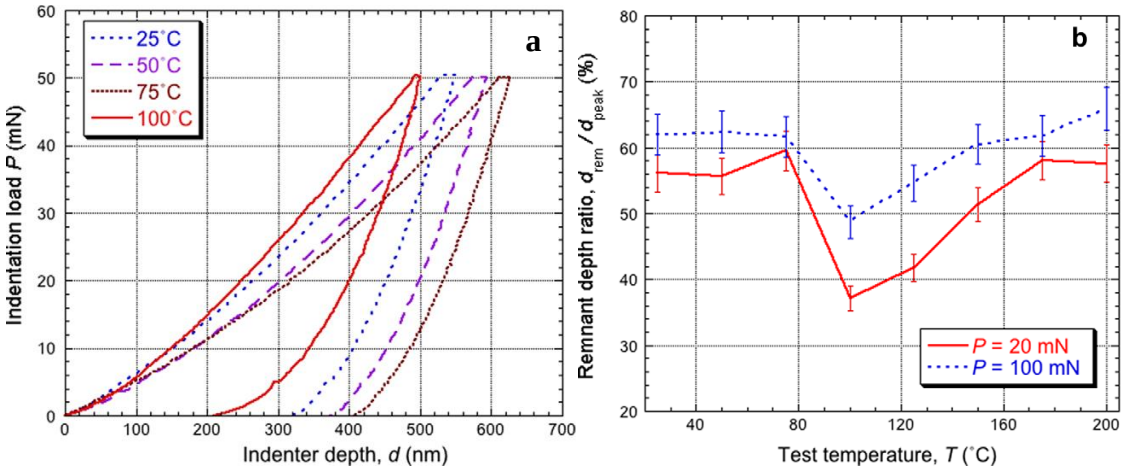

Figure 2.10: Plots of (a) load-depth obtained during indentation at various temperature around and below A_f, (b) remnant depth ratio as a function of indentation temperature at two different loads by using a spherical indenter (r=10μm) [100].

It was confirmed that this procedure could also be applied to evaluate thin films of binary and ternary NiTi-based (Hf, Cu) shape memory alloys over a range of temperatures (up to 400 °C) [101]. The indentation-induced SE effect was also characterized under Berkovich indenter at elevated temperature by Zhang et al. [82], and they observed that the microscopic superelastic behavior of NiTi thin-film occurred at about 100 K above the austenite transformation finish temperature (A_f) which was due to the high hydrostatic pressure under the indenter. Recently, it was found that the phase transformation temperatures and other characteristics of shape memory alloy samples could be estimated by utilizing the instrumented indentation techniques as well as *in situ* nano-compression in a transmission electron microscope (TEM) [104, 105]. In addition, stress-induced phase transformations on shape memory alloys have also been studied at the nano-scale by using multiple nano-indentation techniques [65]. These recent studies clearly show that instrumented indentation techniques can be used to characterize the mechanical response of bulk and thin film NiTi alloys.

2.6.Indentation in Single Crystal

Despite the above progress, previous indentation experimental observations are based on local mechanical testing of polycrystalline shape memory materials which cannot answer some of the fundamental questions related to single crystal alloys due to the complications from the slip systems between grain boundaries which can act as obstacles to dislocation movement in polycrystalline materials. However, in addition to measuring the mechanical properties of materials, instrumented indentation techniques can also be used to illuminate the dislocation phenomenon in single crystal [106, 107]. NiTi single crystals with selected heat treatments were studied by using the instrumented micro-indentation at room temperature, where it shows that indentation hardness and work recoverable energy are a function of the Ti_3Ni_4 precipitate size [3]. The hardness and recoverable energy are maximum for 10 nm precipitates since both the resistance to dislocation motion and stress-induced transformation mechanisms are at maximum, while they both decrease as the precipitate size increased to 100 nm because the former mechanism is decreasing [3]. Later, it was also confirmed on $Ni_{50.9}Ti_{49.1}$ single crystal that the micro-indentation hardness as a function of surface orientation do not correlate with the “yield” strength that was measured from macro compressive mechanical testing, but correlates the best with the resistance to dislocation motion [108]. Another study shows that the nanoindentation response of a [111]-oriented NiTi alloy with a spherical indenter identified the pop-in behavior during the loading process can be fully attributed to the stress-induced formation of martensite [109].

3 EXPERIMENTAL METHODOLOGY

The aim of this chapter is to describe the experimental methodologies used in this study only. Due to various samples including both single crystal and polycrystalline NiTi-based alloys, details of the material thermal processing (homogenization and aging) will be shown in each chapter for clarity. Details of material preparation, calorimetric measurements, mechanical testing, and indentation experiments on both room and high temperature will be presented throughout the chapter, as well as the newly proposed Laser Shock Wave direct ablation experiments.

3.1.Material Preparation

All of the polycrystalline NiTi-based alloys were produced by induction melting or arc melting with high purity elemental constituents. The Bridgeman technique was used to grow alloy single crystals in a Helium atmosphere. The single crystal ingots oriented along [001], [011], and [111] and the extruded rod alloys were cut into compression specimens (4mm x 4mm x 8mm) by electro discharge machining (EDM). EDM is a manufacturing process whereby a desired shape is obtained by using electrical sparks shown in Figure 3.1. Both the single and polycrystalline alloys with high temperature homogenization, over 900 °C, were prepared in vacuum quartz tubes (to avoid oxidation) followed by water quenching. Aging treatments were conducted in the open air using a Lindberg/Blue M BF5114841 box furnace which has a maximum temperature limit of 1200 °C. All specimens were water quenched after any heat treatments or homogenizations.

Figure 3.1: Electrical discharge machining (EDM) to cut specimens into desired shapes.

3.2.Calorimetry Measurements

The differential scanning calorimeter (The Perkin-Elmer DSC Pyris1) method was used to measure transformation temperatures (martensite finish, M_f; martensite start, M_s; austenite start, A_s; and austenite finish, A_f) under the absence of stress. Typical temperature range of the DSC Pyris 1 is from -150˚C to 600˚C. An appropriate heating and cooling rate of 10˚C/minute was used to observe transformation temperatures for all NiTi-based alloys in this study. Figure 3.1 shows the differential scanning calorimeter machine. Prior to the measurements, temperature is calibrated by using the two-point method where the onset temperatures for the melting points of the high purity standard materials, Indium and Zinc, were used. Disposable Perkin Elmer aluminum pans (part number 0219-0041) were used

to hold samples with 20-50 mg in weight. The sample surface must be polished to establish good thermal contact with the inside pan in order to obtain accurate transformation temperatures.

Figure 3.2: Perkin-Elmer Pyris 1 Differential Scanning Calorimeter to measure the stress free phase transformation temperatures.

3.3.Surface Polishing

Prior to any indentation experiments or laser shock wave direct ablation, sample surface roughness needed to be reduced to at least 0.25 μm in order to perform indention on a clean surface. After heat treatment and DSC measurements, the indentation sample was placed in epoxy and polished with the Buehler EcoMet 250 Grinder-Polisher equipped with an AutoMet 250 Power head. Figure 3.3 shows the polishing machine equipped with the power head. It should be noted that a nano-indentation experiment requires near mirror-like smooth surfaces to avoid any affects caused by roughness. Thus, there are six polishing steps used to get the optimum surface roughness of 0.05 μm. The specimen was first polished with a bimetallic plate to remove the major residuals from the cutting edge or heat

treatments. The remaining five steps were started by using 9 µm-grit sized diamond suspensions and followed by 6, 3 µm diamond suspension, during which the polishing processes were held for 4 minutes each. The final two steps were followed by the aluminum pastes (1 and 0.05 µm) to achieve surface roughness of 0.05 µm. With the final step completed, samples were cleaned with alcohol and then taken out of the epoxy.

Figure 3.3: Buehler EcoMet 250 Grinder-Polisher (AutoMet 250 Power head) with chemical polishing.

3.4.Mechanical Testing

The thermal-mechanical and superelasticity experiments were conducted using a MTS Landmark servo-hydraulic test frame with custom compression/tension grips which is shown in Figure 3.4. The applied force was measured by a 100 kN capable load cell and the axial strain was measured by a MTS high temperature extensometer with a gauge length of 12 mm. A PID driven Omega CN8200 series temperature controller with K-type thermocouples were attached to both the specimen and grips to monitor the temperatures.

The experimental setup allows the testing of specimens in compression or tension at a temperature range of 100 to 600 ˚C.

Figure 3.4: The MTS Landmark servo-hydraulic test frame.

3.5.Indentation

A Vickers indentation machine was also used in this study to compare results with nano-indentation results. Vickers hardness values were determined by using the Sun-Tec

model FM-7 micro-hardness test equipment shown in Figure 3.5. Hardness tests were performed with a 100 gf force and 15 seconds dwell time. With ten values at different locations, the hardness value was obtained by taking average of 8 appropriate numbers (the lowest and the highest values were omitted for accuracy).

Figure 3.5: Sun-Tec model FM-7 micro-hardness test equipment.

Nanoscale and microscale-indentation experiments were investigated by using the Nano Test Vantage shown in Figure 3.6. This particular instrumented indentation machine is from Micro Material Ltd (MML) in England. Figure 3.6b shows the inside configurations of each functional part, including two load heads, optical microscope stage, atomic force microscopy (AFM), and the sample stage. The extremely small force and displacement resolutions possible with the MML NanoTest, which are as low as 3 nN and 0.001 nm, respectively, are combined with very large ranges of applied forces (0-500 mN) and displacements (0-50 μm) for the low load head. The high load head greatly expands the capability of the NanoTest Vantage to cover both the nano and micro load range of 0-

20 N where the displacement can be more than 50 µm. with the help of the optical microscopy stage, indentation experiments can be made at specific positions on the specimen such as different grains or even on the boundary.

Prior to indentation, standard load and depth calibrations were conducted. Hardness and elastic modulus were calculated from the initial stage of the unloading curve with curve fitting in the form of power law to the upper 60 % of the final unloading data by using the Nano Vantage Software [110]. Contact compliance and contact depth were calculated from this fit by using the method of Oliver and Pharr [60]. Frame compliance was also taken into account for the contact area and was calibrated on a standard fused silica with a Berkovich indenter.

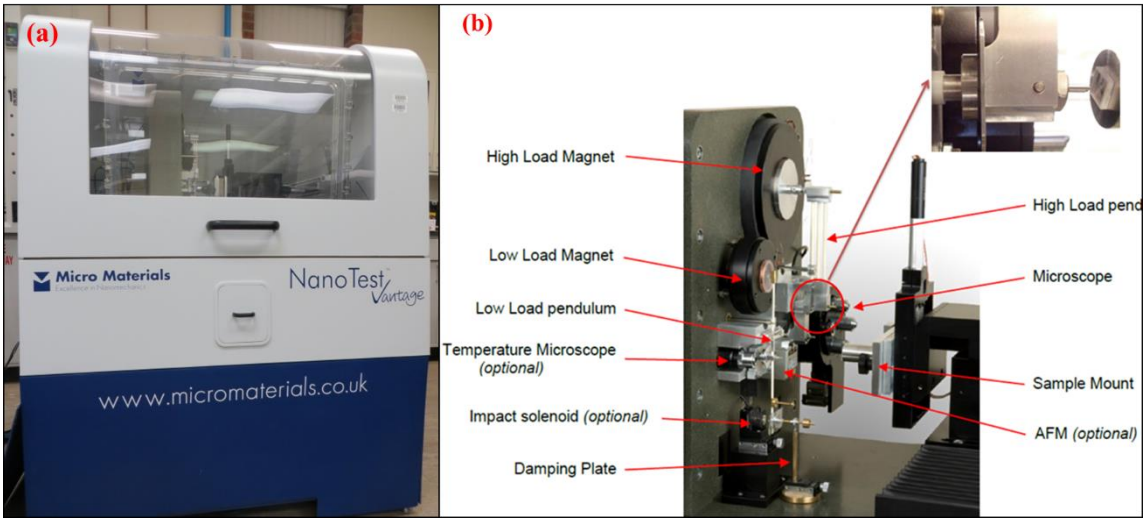

Figure 3.6: Nano Test Vantage Instrumented Indentation Machine (a) the outside figure, (b) detail setup of the inside configurations with low load and high load heads.

This NanoTest Vantage is not only capable of nano/micro-indentation, but also nano-scratch, wear, impact, damping, and fretting experiments. It also has a temperature controller and gas purging system. The sample and indenter can be heated from room temperature up to 750 ˚C with a heating rate up to 8˚C/min. The gas purging system is aimed to protect the sample from being oxidized at high temperatures. Such high

temperature options allow nanoindentation, Nano-scratch & wear, Nano-impact & Fatigue to be performed at temperatures up to 850 ˚C. Unlike other vertically oriented nano-indentation platform systems, Figure 3.7 shows the unique horizontal loading design of the NanoTest Vantage, which ensures no heat flow into the loading head or depth measurement sensors on the left side.

High temperature indentation experiments were investigated from 28 to 340 ˚C. With the high temperature experiments, the platform requires placement in an environmental chamber purged with high purity Argon (such that O_2 levels were maintained <0.01%) to minimize oxidation of both the sample surface and the indenter tip. However, our experiments were investigated without Argon because the alloys are oxidation-free at the temperature of 350 ˚C and diamond indenter is safe below 400 ˚C. The rectangular specimen with surface lengths measuring ~8 mm x 4mm and a thickness of 4 mm was mounted onto a refractory ceramic hot block. Resistance heaters located directly beneath the surface of the ceramic shown in Figure 3.7, and the hot block were used to provide specimen heating. Thermocouples mounted on the surface and directly above the resistance heating element were used to monitor and control specimen temperatures, respectively. To minimize transient thermal fluctuations and heat transfer between the specimen surface and indenter tip during experiments, a separate resistance heater thermal control system was used to provide heating of the indenter. The temperatures of the specimen surface and indenter were controlled to within ~0.1 ˚C.

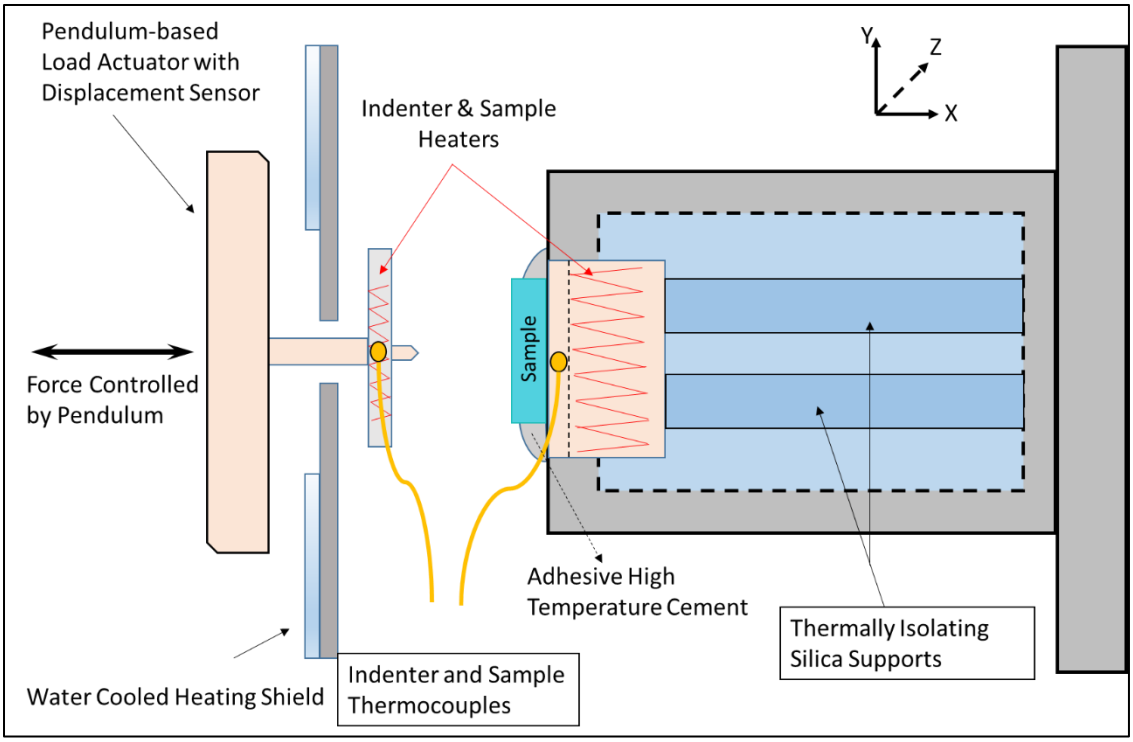

Figure 3.7: The horizontal loading design of the NanoTest Vantage with the high temperature set up.

Various spherical indenters with different tip radius size were used in this study in both room and high temperature phases. Detailed parameters of three different spherical tips were listed in Table 3.1 with calculated theoretical maximum limits on the contact depth, contact force, and contact area. One standard Berkovich indenter was also used in this study. All three spherical indenters have a full cone angle of 60 degrees. A simple sketch of a 5 µm tip spherical indenter is shown in Figure 3.8. The maximum contact depth was calculated at 2.5 µm shown as D_c (in Figure 3.8) which is the maximum sphere contact depth. If indentation depth is greater than 2.5 µm, the contact between indenter and specimen is no longer in the spherical region. A ratio of $D_{max}/R=0.5$ was calculated for this 60 degree indenter shape with a 5 µm tip.

Table 3.1: Spherical indenters with calculated theoretical maximum limit parameters.

Tip radius (60˚ full angle)	Theoretical Max contact depth	Theoretical Max contact force	Theoretical Max contact area
5μm	2.5 μm	471 mN	58.9 μm^2
25μm	12.5 μm	11774 mN	1471.8 μm^2
50μm	25 μm	11774 mN	1471.8 μm^2

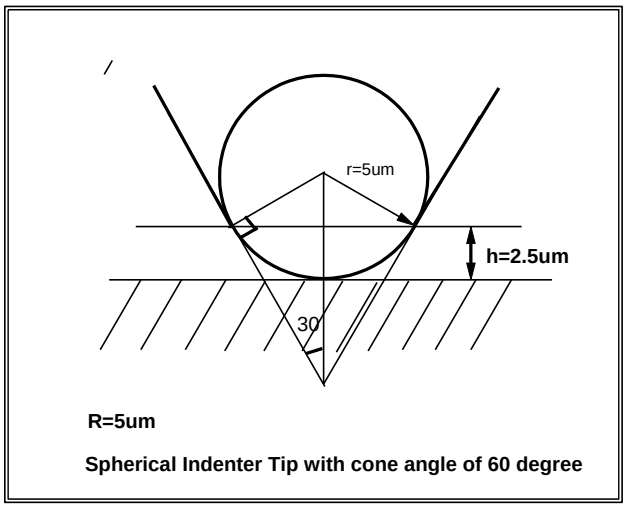

Figure 3.8: An example spherical indenter with a tip radius of 5 μm and a full angel of 60 degree.

A corresponding indentation load-depth curve with important indentation parameters is shown in Figure 3.9. The recoverable work energy W_e , can be obtained by integrating the unloading curve, where L is the applied load, D is the penetration depth, D_{max} is the maximum depth, and D_r is the recovery depth. Total deformation energy W_t is the area under the loading curve. The area between the loading and unloading curve is called irrecoverable work W_{irr} , also known as dissipation energy. The ratio of the recoverable deformation energy to the total deformation energy is defined as η_w, which is expressed in equation (3.1).

$$\eta_w = \frac{W_e}{W_t} = \frac{\int_{D_r}^{D_{max}} Fdh}{\int_0^{D_{max}} Fdh} \tag{3.1}$$

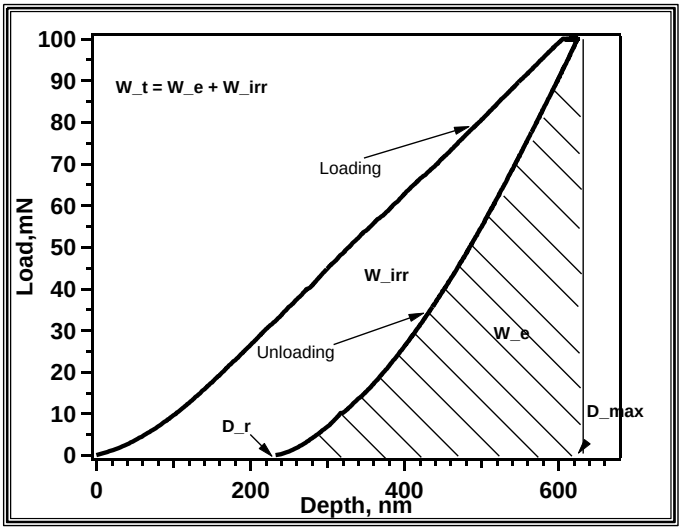

Figure 3.9: Corresponding indentation load-depth curve with important indentation parameters.

4 INDENTATION RESPONSE OF NITI-BASED SHAPE MEMORY ALLOYS AT AMBIENT TEMPERATURE

4.1.Introduction

NiTi alloys have good ductility and large transformation strain (10%) that makes them suitable for many commercial applications such as actuators, sensors, dampers, sealing elements, couplers, biomedical devices and electrical components [1, 2]. However, low transformation temperatures (<100º C) and strength (<700MPa) of near-equiatomic NiTi alloys limit a wider use of their applications in high temperatures or strength environments [4].

Ni-rich NiTi shape memory alloys have better superelasticity and shape memory properties than near equiatomic NiTi shape memory alloys [5]. Aging and composition alteration can be employed to increase the strength and control their transformation temperatures to result in superelasticity at room temperature [5-10]. Ternary alloy Ni rich NiTiHf has higher strength and transformation temperatures than other NiTi alloys [111], and they show superelasticity at high temperatures of about 200 °C [112]. Quaternary element Cu was added to NiTiHf in order to improve the thermal stability, but it was found to decrease TTs [52, 53]. Karaca *et al*. reported shape memory behavior, TWSME and superelastic properties after the addition of 5% Cu was replaced with Ni of $Ni_{50.3}Ti_{29.7}Hf_{20}$ [113] which shows no superelasticity at room temperature with two different aging methods. Recently, quaternary alloy $Ni_{45.3}$-$Ti_{29.7}$-Hf_{20}-Pd_5 (at.%) was developed where full strain recovery in superelasticity and shape memory effect (SME) without significant plastic deformation was observed at high stress levels (> 1 GPa). Moreover, they have high

damping capacity (30-34J cm^{-3}), and their shape memory properties can be controlled by aging and orientation selection [13].

Most nanoindentation studies on SMAs are mostly based on the measurements at room temperature. In particular, indentation hardness and depth recovery ratio have been examined to demonstrate the shape memory effect and superelasticity in SMAs [12, 14, 91, 92]. It was found that the indentation depth imposed by spherical indenters can be almost fully recovered upon heating, while only partial deformation induced by Berkivoch indenter can be recovered [12]. It has been shown that superelastic NiTi alloys have large recoverable depths [11], where the depth recovery ratio of a superelastic NiTi was about 45% for Berkovich (~200mN) and 95% for spherical (~2.75N) indenters [12]. Thus, it can be concluded that extensive plastic deformation can be omitted and superelasticity can be detected much easier by using a spherical indenter [12]. There are several studies on the indentation-induced shape memory and superelastic effects in NiTi thin films [80-82]. The shallow spherical indents in austenitic NiTi can fully recover upon unloading, while indents in martensite can partially recover after unloading [110] and fully recover occurs upon heating to austenite phase, which is also known as 'self-healing' effect [14]. In addition, Li *et al*. [] recently reported that phase transformation temperatures, superelastic and plastic deformation behavior can be determined from the work recovery response as a function of temperature.

In this study, spherical indentation responses of room temperature superelastic (e.g. homogenized $Ni_{50.8}Ti_{49.2}$ and 400°C 3h aged $Ni_{45.3}Ti_{29.7}Hf_{20}Pd_5$) and nonsuperelastic (e.g. $Ni_{49.9}Ti_{50.1}$ and 600°C 3h aged $Ni_{45.3}Ti_{29.7}Hf_{20}Pd_5$) SMAs are revealed as functions of maximum loading level in nano and macro scales. Moreover, Berkovich and spherical

indentation responses of NiTi-based SMAs were investigated at room temperature under load range from 10-500 mN. Spherical indentation hardness, modulus, and work recovery of NiTi-based alloys are revealed as function of indentation depth, and are compared with a Berkovich indenter.

Eight alloys with the compositions of $Ni_{49.9}Ti_{50.1}$, $Ni_{50.8}Ti_{49.2}$, $Ni_{50.3}Ti_{29.7}Hf_{20}$, $Ni_{45.3}Ti_{29.7}Hf_{20}Pd_5$, and $Ni_{45.3}Ti_{29.7}Hf_{20}Cu_5$ were used in this study. $Ni_{50.8}Ti_{49.2}$ was aged at 1000 °C-2hrs, $Ni_{45.3}Ti_{29.7}Hf_{20}Pd_5$ alloys were aged under 400 and 600 °C-3hrs, and $Ni_{45.3}Ti_{29.7}Hf_{20}Cu_5$ were aged under 500 and 600 °C for 3 hrs.

4.2.Stress-Free Phase Transformation Temperatures of NiTi-Based Alloys

The martensite and austenite start and finish temperatures (M_s, M_f, A_s and A_f, respectively) of NiTi-based alloys are determined from DSC response and summarized in Table 4.1. It has been found that 1000°C-2hrs aged $Ni_{50.8}Ti_{49.2}$, as-received and 400 °C-3hrs aged $Ni_{45.3}Ti_{29.7}Hf_{20}Pd_5$ are austenite while other alloys are martensite at room temperature. For simplicity, these alloys will be renamed as shown in Table 4.1. It is instructive to note that A_f of both NiTi-A and NiTiHfPd-A (400) are below room temperature, and NiTiHfPd-A is 20 °C above room temperature, which indicates that these alloys will show superelasticity at room temperature. Table 4.1 also shows the conventional Vickers hardness results of the alloys tested where the original unit of Vickers hardness (HV) was converted to GPa. As shown in the Table 4.1, the Vickers hardness of NiTiHfPd alloys are the highest and NiTi alloys are the lowest among all alloys. These observations agree well with the mechanical results where it was reported that NiTiHfPd alloys [114] have a higher strength than NiTiHf [115] and NiTi [4] alloys.

Table 4.1: Transformation temperatures observed from DSC and Vicker's hardness at room temperature for NiTi-based alloys.

Sample	Aging	Rename	Ms (°C)	Mf (°C)	As (°C)	Af (°C)	Phase at rooom temperature	Vicker hardness (Gpa)
$Ni_{49.9}Ti_{50.1}$	None	NiTi-M	78	45	85	122	Martensitic	2.19
$Ni_{50.8}Ti_{49.2}$	2h-1000°C	NiTi-A	-15	-34	-4	10	Austenite	2.37
$Ni_{50.3}Ti_{29.7}Hf_{20}$	None	NiTiHf-M	117	101	139	153	Martensitic	3.39
$Ni_{45.3}Ti_{29.7}Hf_{20}Pd_5$	None	NiTiHfPd-A	4	-30	27	53	Austenite	6.43
$Ni_{45.3}Ti_{29.7}Hf_{20}Pd_5$	3h-400°C	NiTiHfPd-A(400)	-90	-114	-23	-9	Austenite	5.32
$Ni_{45.3}Ti_{29.7}Hf_{20}Pd_5$	3h-600°C	NiTiHfPd-M(600)	95	63	110	160	Martensitic	4.81
$Ni_{45.3}Ti_{29.7}Hf_{20}Cu_5$	3h-500°C	NiTiHfCu-M(500)	60	36	90	114	Martensitic	4.14
$Ni_{45.3}Ti_{29.7}Hf_{20}Cu_5$	3h-600°C	NiTiHfCu-M(600)	81	44	129	154	Martensitic	3.97

4.3.Shape Memory Behavior of NiTi-Based Alloys

The room temperature compressive response of the alloys are shown in Figure 4.1. The alloys that are austenite at room temperature (NiTi-A, NiTiHfPd-A and NiTiHfPd-A(400)) show superelasticity. It should be noted that NiTiHfPd-A(400) has full strain recovery without any plastic deformation after being loaded to an extremely high stress level of 2 GPa. This unique polycrystalline alloy also presents a very high damping capacity (30-34 J-cm^{-3}), high work output (30-35 J-cm^{-3}) and high mechanical hysteresis (900 MPa) [13]. The alloys that are martensite at room temperature (NiTi-M, NiTiHf-M, NiTiHfPd-M (600), NiTiHfCu-M (500), and NiTiHfCu-M (600)) show martensite reorientation upon loading which does not recover back upon unloading.

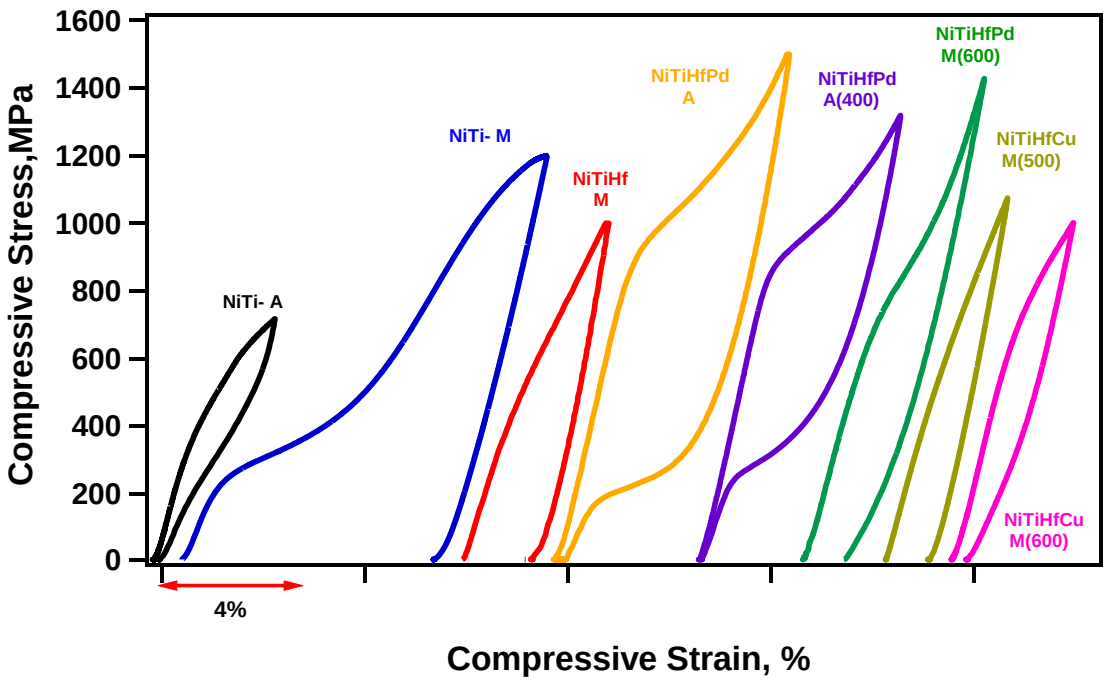

Figure 4.1: Stress-strain relationships of NiTi-based alloys on bulk material at room temperature.

4.4. Spherical Indentation Response of NiTi and NiTiHfPd Alloys

4.4.1. Spherical Indentation Load-Depth Curves

Figure 4.2a shows the selected load-displacement (L-D) curves for the spherical indentation of NiTi-A and NiTi-M alloys where samples were loaded until the selected load levels of 10, 25 and 50mN, and then unloaded at room temperature. Significant differences in the indentation response of the two NiTi alloys are the work recoverable ratio and hardness. The work recoverable ratio of NiTi-M and NiTi-A are calculated to be 32.4% and 50.3%, respectively, under 50mN loading. It clearly shows that NiTi-A with superelasticity (SE) behavior has a higher work recoverable ratio than that of NiTi-M. In superelasticity, austenite transforms to martensite during loading and martensite transforms

back to austenite during unloading, while martensite reorientation occurs during loading and it does not recover back after unloading for the martensitic SMAs tested at temperatures below A_s. Thus, superelastic NiTi-A exhibits a higher recoverable ratio than NiTi-M. Figure 4.2b presents L-D curves of NiTiHfPd alloys at selected loads of 10, 25 and 50mN. The indentation curve demonstrates superelasticity with a hysteresis loop at load level of 10mN, which means that the material that transformed to martensite in the loading process can transform completely back to the original austenite state. Similar behavior was observed previously in NiTi alloys with superelasticity [12, 88, 116, 117] . The work recoverable ratios of NiTiHfPd-M (600) and NiTiHfPd-A (400) were calculated as 65.4%, and 97% at the load level of 10mN. At higher load level (100, 250 and 500mN), load-displacement curves were plotted as Figure 4.2c and Figure 4.2d for the NiTi and NiTiHfPd alloys, respectively. It can be observed that work recovery ratios at high loads are much smaller than the ones at low loads. Figure 4.2c shows deeper indentation depth than Figure 4.2d which indicates that NiTiHfPd alloys are harder than NiTi alloys.

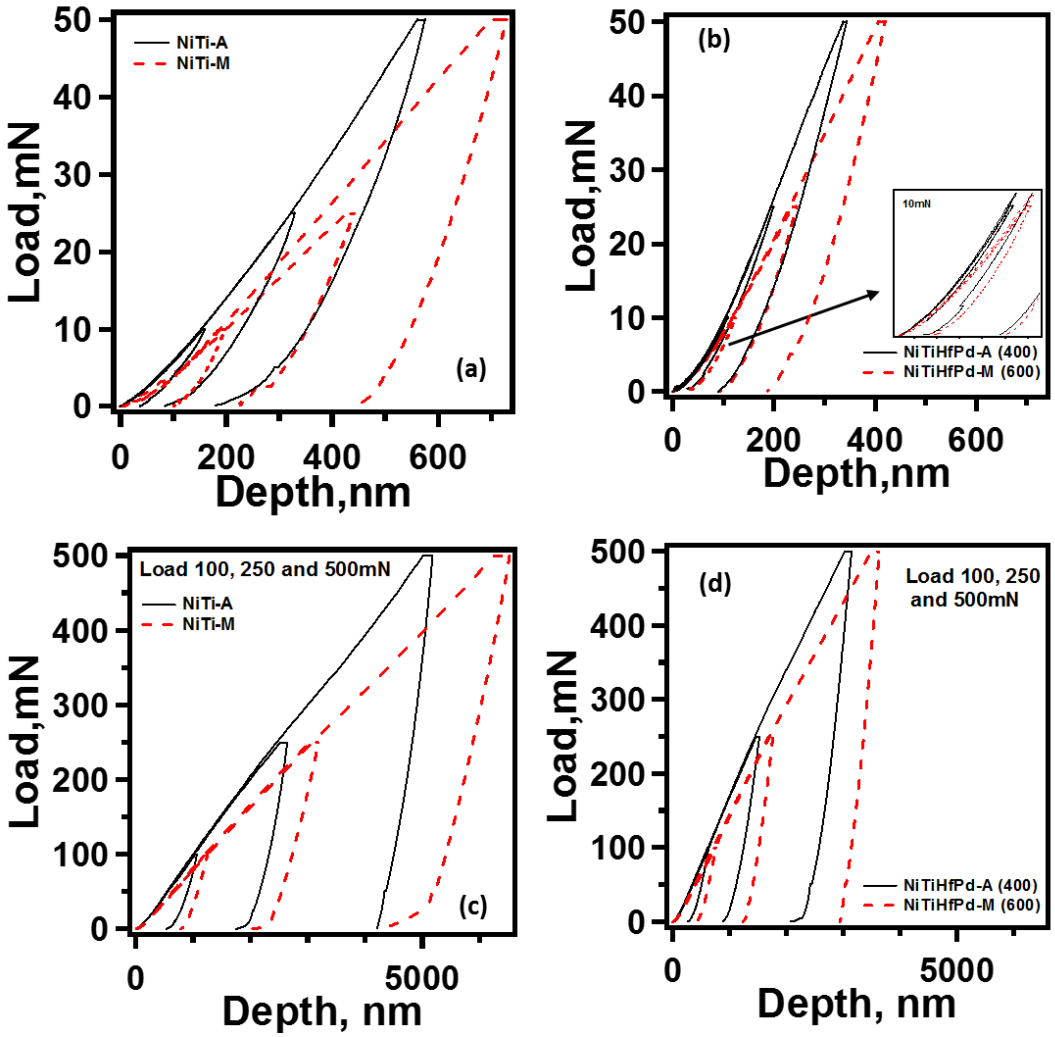

Figure 4.2: Nano-indentation results of typical load-displacement relationships. Load-displacement curve of a) NiTi-M and NiTi-A at 10mN, 25mN, and 50mN b) NiTiHfPd-M (600) and NiTiHfPd-A(400) at 10mN, 25mN, and 50mN (c) NiTi-M and NiTi-A at 100, 250 and 500mN (d) NiTiHfPd-M (600) and NiTiHfPd-A(400) at 100, 250 and 500mN.

With a cone angle of 60 degree on the spherical indenter tip, according to Cheng and Cheng's analysis on tip geometry [118], the spherical tip results in a maximum spherical contact depth of D_c=2.5 µm for the current study. Thus, indentation depths deeper than 2.5 µm will not result in perfect spherical contact. Table 4.2 lists D_{max}/R of NiTi, NiTiHf, NiTiHfPd and NiTiHfCu alloys at selected load levels from 10-500 mN.

If $D_{max}/R < 0.5$, spherical contact.

If $D_{max}/R > 0.5$, conical contact. (4.1)

The results indicated in red in Table 4.2 will not be taken into consideration for the spherical contact.

Table 4.2: Calculated D_{max}/R of NiTi, NiTiHf NiTiHfPd, and NiTiHfCu alloys at selected load level of 10mN, 25mN, 50mN, 100mN, 250mN, and 500mN.

Load(mN) \Dmax/R	NiTi-M	NiTi-A	NiTiHf-M	NiTiHfPd-A	NiTiHfPd-A(400)	NiTiHfPd-M(600)	NiTiHfCu-M(500)	NiTiHfCu-M(600)
10	0.042	0.035	0.021	0.021	0.021	0.025	0.025	0.023
25	0.135	0.066	0.046	0.040	0.040	0.049	0.054	0.049
50	0.147	0.113	0.086	0.068	0.070	0.085	0.094	0.088
100	0.258	0.211	0.169	0.120	0.126	0.153	0.171	0.160
250	0.652	0.534	0.388	0.276	0.300	0.353	0.412	0.382
500	1.311	1.035	0.808	0.557	0.626	0.720	0.858	0.793

4.4.2. Discussion

4.4.2.1. Work/Depth Recovery

Figure 4.3 summarizes the work recovery ratio of NiTi and NiTiHfPd alloys as a function of D_{max}/R. Data was calculated from the typical load-depth curves show in Figure 4.2. It shows that W_e/W_t decreases quickly and then saturates with the D_{max}/R for all the alloys. Moreover, at the same D_{max}/R, it is observed that alloys with SE behavior (NiTi-A and NiTiHfPd-A (400)) have higher work recovery ratio than non-SE alloys (NiTi-M and NiTiHfPd-M (600)). The work recovery ratio of NiTiHfPd-A (400) is the highest. Work recovery ratios saturate to a plateau of 0.2 as D_{max}/R reaches to about 0.5. It should be noted that $D_{max}/R=0.5$ was calculated as a spherical contact limit. This can be attributed to the plastic deformation that impedes martensite to austenite back transformation. At low

load levels, plastic deformation can be avoided which results in high recovery ratio. In the alloys with superelastic behavior, the recovery ratio is higher since in addition to classical elastic recovery they have the ability to demonstrate recovery due to back transformation during unloading. The plastic deformation increases with load levels and prevents the back transformation of stress induced martensite which results in a lower work recovery ratio.

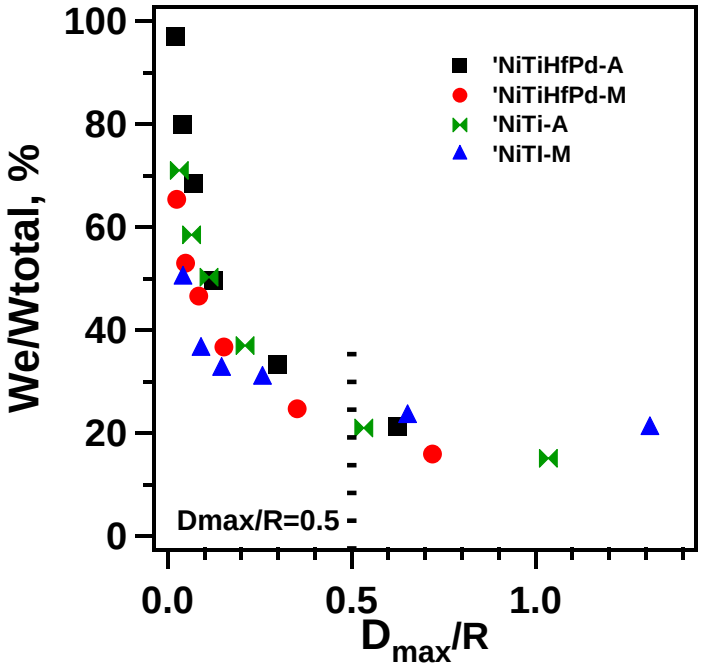

Figure 4.3: Work recoverable ratios as a function of D_{max}/R of NiTi and NiTiHfPd alloys. Data were calculated from six load levels of 10mN, 25mN, 50mN, 100mN, 250mN and 500mN.

Table 4.3 demonstrates the depth recovery ratios of spherical indentation in NiTi and NiTiHfPd alloys. It is clear that depth recovery ratios of NiTiHfPd-A and NiTi-A are higher than NiTiHfPd-M and NiTi-M, respectively. The depth recovery has the same behavior as work recovery where it decreases as a function of indentation depth. Such a decrease was also reported for SE NiTi spherical indents by using FEM modeling and experiments [88].

Table 4.3: Depth recovery ratio of spherical indents on NiTi and NiTiHfPd alloys at selected load levels.

Indentation load (mN)		10	25	50	100	250	500
Depth recovery ratio %	NiTi-M	46.6	43.1	39.6	37.4	37.7	34.9
	NiTi-A	77.3	71.9	64.7	50.1	31.8	18.7
	NiTiHfPd-M(600)	74.8	62.0	54.9	41.7	30	18.9
	NiTiHfPd-A(400)	95.2	86.5	74.2	58.3	43.7	27.9

Figure 4.4 shows the depth recovery ratio of current NiTi and NiTiHfPd alloys and the modeling results from Zhang et al [88] as a function of maximum indentation depth. Depth recovery ratios of those four alloys behave the same way as work recovery ratios where they initially decrease and then saturate beyond the maximum spherical indentation depth of 2.5 μm. The experimental results are in good agreement with the modeling results of superelastic NiTi alloy.

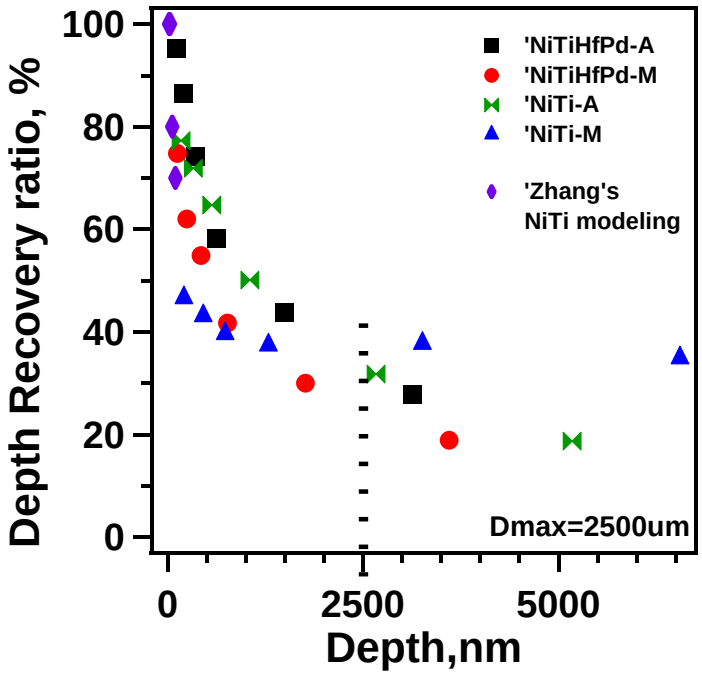

Figure 4.4: Depth recovery ratio as function of maximum indentation depth for NiTi and NiTiHfPd alloys. Zhang's results from modeling of superelastic NiTi were added for comparison [88].

4.4.2.2. Dimensionless Analysis of Load-Depth.

Figure 4.5 shows the non-dimensionalized load-displacement curves which correspond to load-displacement results shown in Figure 4.2. Dimensional analysis provides a better understanding of unloading curves than the traditional load-depth curves. Figure 4.5a, b, and c are the dimensionless L-D curves of NiTi alloys at selected load levels of 10, 25, and 50 mN, respectively. F_{max} is the maximum force applied during loading, D_{max} is the maximum depth the indenter reached during the indentation processing. F and D represent the applied load and depth, respectively. It clearly shows from Figure 4.5a, b and c that NiTi-A has a larger depth recovery during unloading than NiTi-M which results in higher work recoverable ratio. Figure 4.5d, e and f present dimensionless L-D curves of NiTiHfPd alloys at selected load levels of 10, 25, and 50mN. Similar to NiTi, NiTiHfPd-A (400) has a larger work recovery ratio than NiTiHfPd-M (600). It should also be mentioned that almost perfect shape recovery observed in NiTiHfPd-A (400) at load level of 10mN (Figure 4.5 d), which proves the perfect SE behavior. Increasing load level results in reduced work recovery for NiTi and NiTiHfPd alloys.

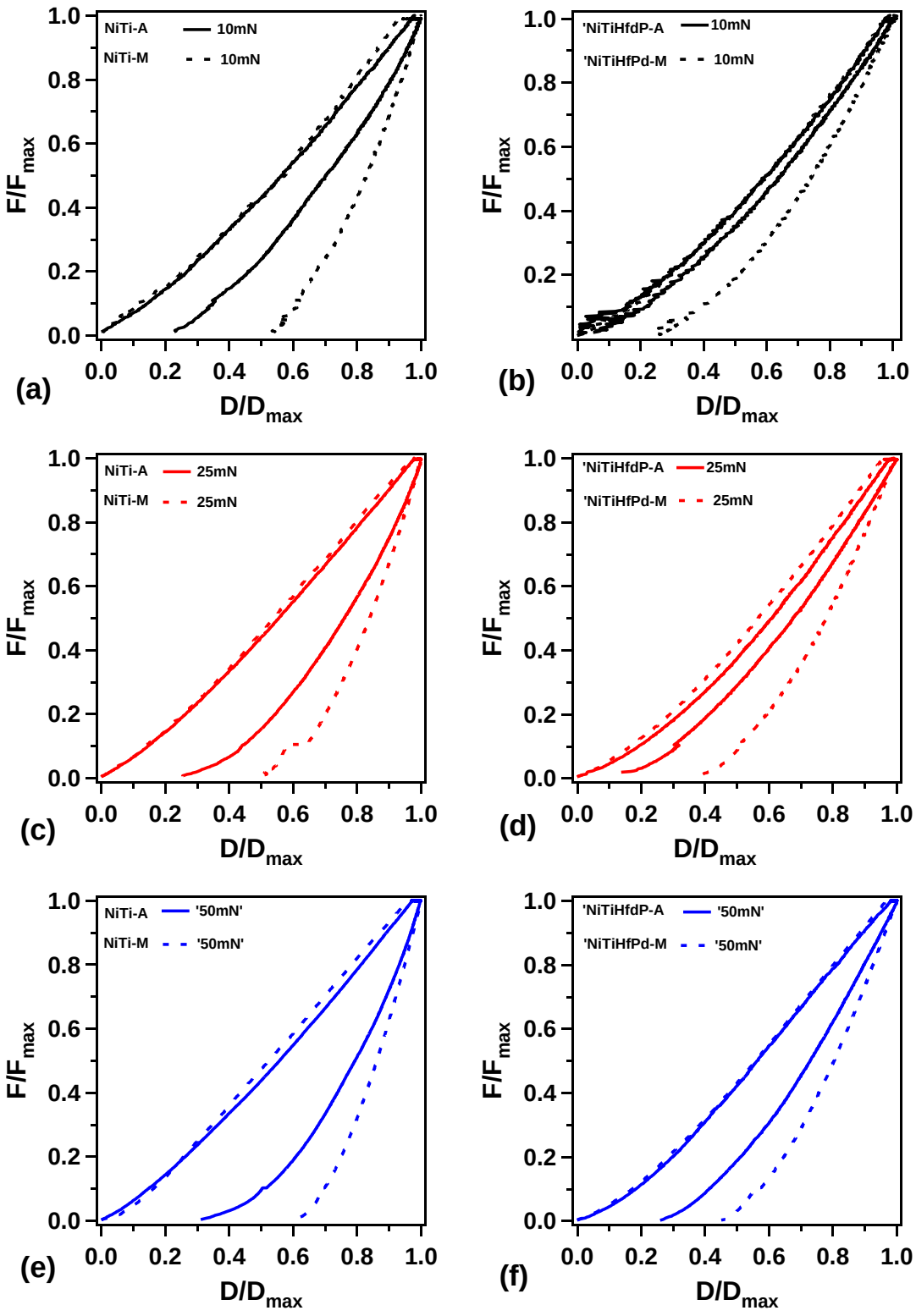

Figure 4.5: The corresponding dimensionless load-displacement curves (a) NiTi alloys at 10mN, (b) NiTi alloys at 25mN, (c) NiTi alloys at 50mN, (d) NiTiHfPd alloys at 10mN, (e) NiTiHfPd alloys at 25mN, (f) NiTiHfPd alloys at 50mN.

4.4.2.3. Indentation Hardness

Figure 4.6 shows the spherical hardness as a function of maximum indentation depth. It shows the hardness values of NiTi and NiTiHfPd alloys as a function of indentation depth that is calculated from the load-displacement curves from Figure 4.2. It should be noted that the maximum depth is proportional to the applied maximum load. The spherical hardness significantly depends on the indentation depth and the average hardness value increases with increasing indentation depth, and saturates at higher loads. This depth dependent behavior of spherical hardness of NiTi SMAs is the opposite of the hardness values obtained by sharp indenter[119]. The increase in the spherical hardness can be explained by the increase in the transformed region and plastic deformation during loading. Eq (4.2) is the well-known Hertz's theory for a purely elastic contact on a material without any phase transition, where the spherical hardness H can be expressed as:

$$H=\frac{4}{3\pi}\ \frac{E}{1-\nu^2}\ \sqrt{\frac{D}{R}} \tag{4.2}$$

where E is the elastic modulus, ν=0.3 is the Poisson's ratio, and R is the spherical tip radius, h is the indentation depth. Evidently, Eq (4.2) indicates that spherical hardness increases with the square root of indentation depth ($D^{0.5}$) for a purely linear elastic material. Eq (4.2) cannot be directly applied to NiTi SMAs due to the phase transformation. However, a recent report revealed that the spherical hardness of NiTi is proportional to indentation depth (D) if the phase transformation involved occurs during indentation loading [120].

The spherical hardness of NiTi and NiTiHfPd alloys show a good agreement with literature where hardness increases with indentation depth, but the increase is not proportional to D or $D^{0.5}$. Indentation at austenite phase can result in phase transformation to martensite, and hardness of both phases contributes to the overall hardness. In this study, both NiTi and NiTiHfPd alloys have higher hardness in austenite than martensite. NiTiHfPd-A (400) has the highest hardness and NiTiHfPd alloys are harder than the NiTi alloys at the selected indentation depth. This observation is in good agreement with the mechanical results where the extremely high strength levels were observed in NiTiHfPd alloys as shown in Figure 4.1. Vickers hardness results were also included in Table 4.1. It also shows that NiTiHfPd alloys have higher Vickers hardness values than the NiTi alloys, and indeed, NiTiHfPd-A (400) possess the highest Vickers hardness. These observations from Vickers hardness experiments are in good agreement with the nanoindentation hardness.

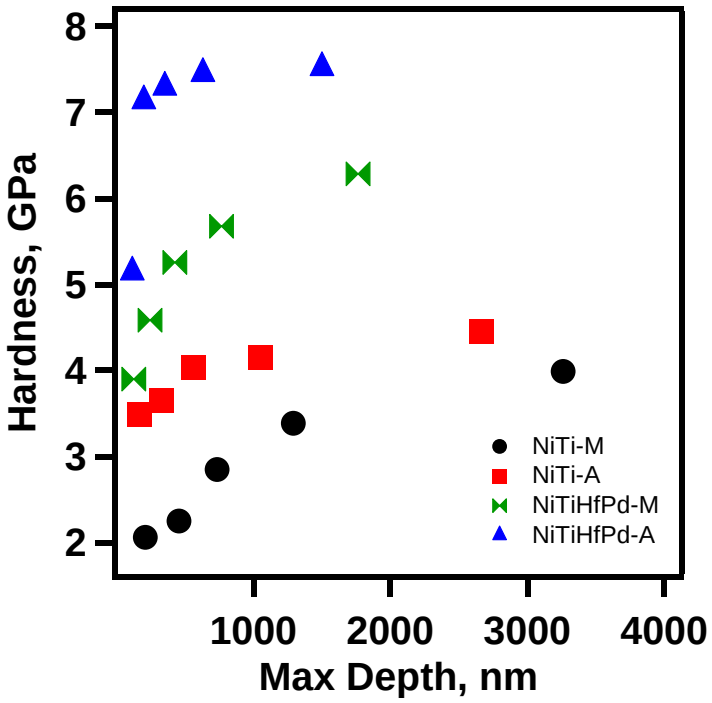

Figure 4.6: Hardness vs. maximum depth relationship of NiTi and NiTiHfPd alloys. Data were calculated at selected load of 10mN, 25mN, 50mN, 100mN, and 250mN.

4.4.3. Conclusion

1. At low load level of 10mN, almost perfect work recovery (97%) and depth recovery (95.2%) is obtained in NiTiHfPd-A, and NiTiHfPd-M shows 65.4% work recovery and 74.8% depth recovery. In addition, NiTi-M has the lowest work recovery (50%) and depth recovery (46.6%) while NiTi-A shows 71% work recovery and 77.3% depth recovery.
2. Alloys with SE behavior (NiTi-A and NiTiHfPd-A (400)) have higher hardness and work recoverable ratio than non-SE alloys (NiTi-M and NiTiHfPd-M (600)) at the same indentation depth.
3. The highest spherical indentation hardness was observed in NiTiHfPd-A (400) which has an extremely high strength of 2GPa.
4. The work recoverable ratio decreases with increasing D_{max}/R due to the fact that at shallow indentation depths (corresponds to low loads) mainly elastic deformation (and reversible phase transformation) takes place which results in high recovery ratio. For deep indentations, plastic deformation impedes the back phase transformation and results in partial work recovery.

4.5. Load and Indenter Effect of NiTi-Based Shape Memory Alloys

4.5.1. Spherical and Berkovich Indentation Load-Depth Curves of NiTi-Based Alloys

The spherical and Berkovich load-depth (L-D) responses of these NiTi-based alloys are separated into two group of load levels (i) 10 mN, 25 mN, 50 mN, and (ii) 100 mN, 250 mN, 500 mN. It is clear that group (ii) loads are ten times higher than group (i). Figure 4.7 shows the selected L-D curves of NiTi-based alloys for load levels of 10 mN, 25 mN, and 50 mN. The solid line represents the L-D curves obtained by using the spherical indenter, while the dash line are the results by using the Berkovich indenter. The spherical indentation responses of NiTi, NiTiHfPd-A(400), and NiTiHfPd-M(600) were extracted from our previous report [110]. Samples were loaded till the selected peak load and hold for 10 seconds, and then unloaded at room temperature. It should be noted that Berkovich indenter is sharp and increased plastic deformation is expected when it is compared to spherical indenter.

Figure 4.7a and Figure 4.7b are the indentation responses of NiTi-M (non-superelastic) and NiTi-A (superelastic), respectively. For the same load level, D_{max} of NiTi-M is higher when Berkovich indenter is used while D_{max} of NiTi-A is same for both indenters under 50 mN load. D_{max} of NiTi-M is higher than the D_{max} of NiTi-A with both indenters, which demonstrates that NiTi-A has higher hardness than NiTi-M.

It has been reported that the spherical indentation response of superelastic NiTi alloy has higher work recoverable ratio than the non-superelastic NiTi alloy due to the fact that superelastic alloys experience the reversible phase transformation upon unloading [110]. Comparing the unloading curves of Berkovich responses shown in Figure 4.7a and

Figure 4.7b, it can be concluded that NiTi-A shows more pronounced recovery than the NiTi-M. NiTi-A has higher work/depth recoverable ratio than the NiTi-M although it was previously reported that Berkovich indenter cannot easily and clearly detect the superelasticity due to the extensive plastic deformation underneath the sharp geometry [12]. Detail of work recovery and mechanical results will be discussed later.

Figure 4.7c presents the L-D curves of NiTiHf-M which is non-superelastic alloy at room temperature. The D_{max} of NiTiHf-M are lower than the values obtained from NiTi-M for both spherical and Berkovich indenters, resulting in higher hardness of NiTiHf alloys which is in good agreements with the Vicker's hardness and mechanical testing results [111]. However, it seems indistinct to compare the strength of materials by only using the D_{max} from Berkovich L-D results since the D_{max} of NiTiHf-M shown in Figure 4.7c is higher than NiTi-A under Berkovich indenter, which violates the previous mechanical findings. Such odd observation may be due to the following facts: 1) under "sharp" Berkovich indenter, SIM phase transformation from austenite to martensite still can be observed partially in NiTi-A, thus the deformation of remained austenite phase, transformed martensite phase, and plasticity of all phases could impede the displacement motion, results in lower D_{max} than NiTiHf-M, 2) shape memory properties of NiTiHf-M alloy is weak compare with other aged NiTiHf alloys, while NiTi-A shows relative high strength than most of NiTi alloys.

Figure 4.7d, Figure 4.7e, and Figure 4.7f are the L-D curves of NiTiHfPd-A, NiTiHfPd-A(400) and NiTiHfPd-A(600). It should be noted that NiTiHfPd-A and NiTiHfPd-A(400) are superelastic while NiTiHfPd-M (600) is non-superelastic at room temperature. NiTiHfPd alloys show the lowest D_{max} under both indenter tips, thus they

have the highest hardness and strength. To be noted in Figure 4.7d, under a spherical tip, perfect reversible depth recovery from NiTiHfPd-A under the peak load of 10 mN with no hysteresis loop is observed, indicating no energy loss during loading and unloading. Similar result was also obtained in NiTiHfPd-A (400) under 10 mN in Figure 4.7e, but with a 3 % irrecoverable work loss. Indentation L-D responses of NiTiHfPd-A and NiTiHfPd-A (400) are very similar under both indenters due to the similar shape memory behavior, while the NiTiHfPd-M (600) does not behave such high work/depth recovery ratio and has higher D_{max}, due to its lower strength than NiTiHfPd-A and NiTiHfPd-A (400).

Figure 4.7g and Figure 4.7h are the L-D curves of NiTiHfCu alloys with different aging conditions of 500 °C-3hrs and 600 °C-3hrs, accordingly. The D_{max} of NiTiHfCu-M (500) at each peak load are slightly deeper than NiTiHfCu-M (600) in both spherical and Berkovich, but very close to NiTiHf-M alloy in Figure 4.7c. However, the L-D curves of NiTiHfCu alloys show lower strength and work/depth recovery than NiTiHfPd alloys. Another feature need to be noted is that D_{max} is higher for Berkovich than spherical indentation for the same peak load level. Similar observation was reported in indentation response of a superelastic NiTi alloy with a spherical tip radius of 213.4 μm and a Berkovich diamond tip [12].

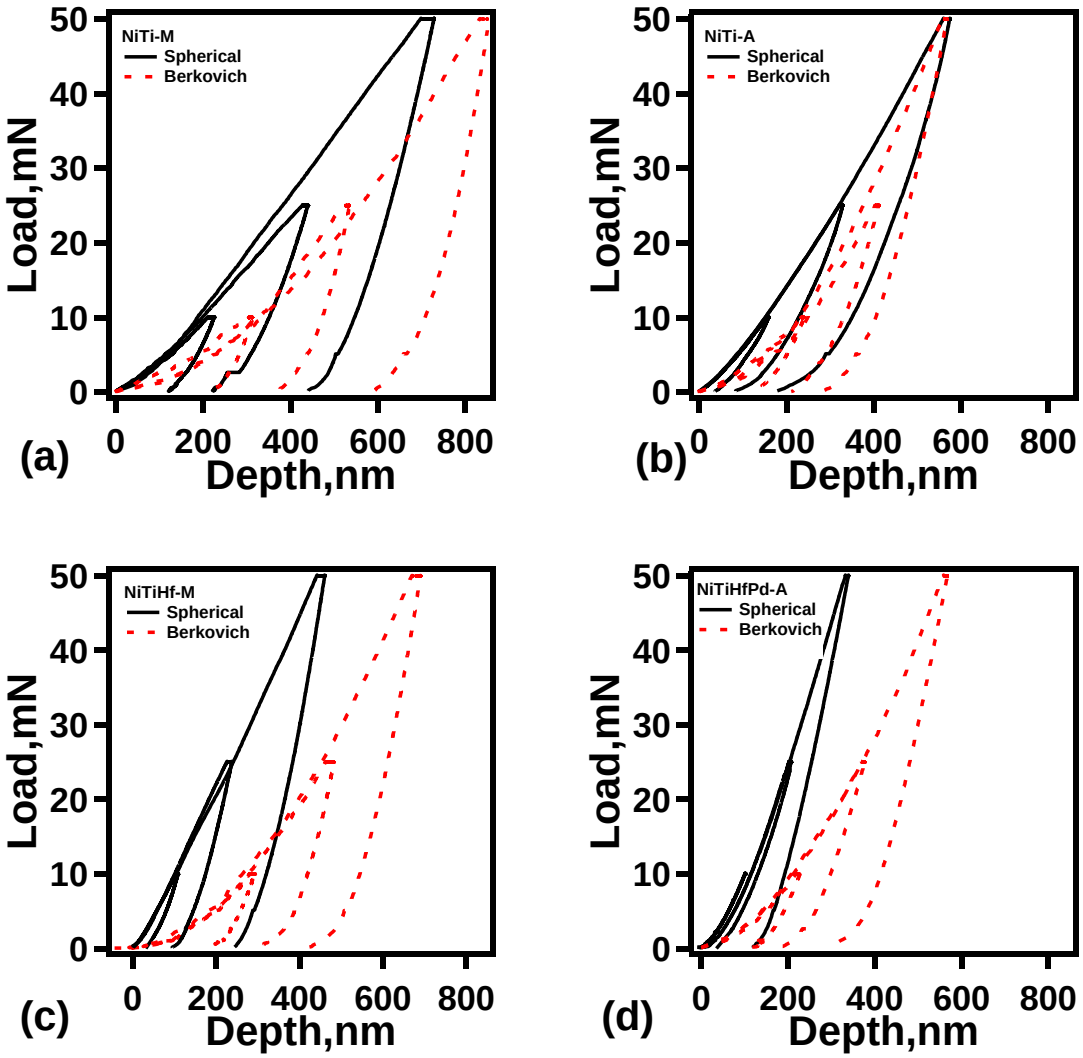
NiTi-M
Spherical
Berkovich
Load,mN
Depth,nm
(a)
NiTi-A
Spherical
Berkovich
Load,mN
Depth,nm
(b)
NiTiHf-M
Spherical
Berkovich
Load,mN
Depth,nm
(c)
NiTiHfPd-A
Spherical
Berkovich
Load,mN
Depth,nm
(d)

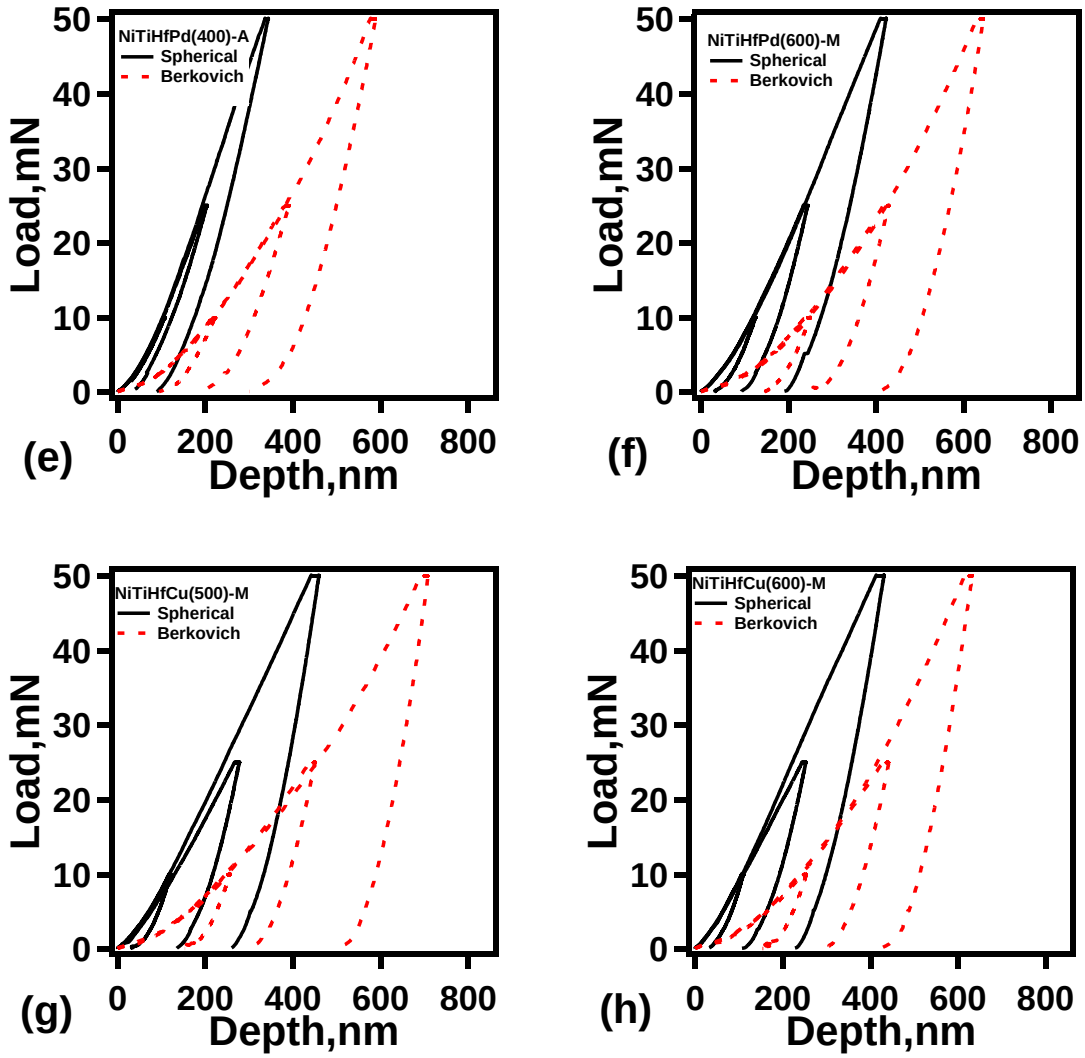

Figure 4.7: Spherical and Berkovich nano-indentation L-D response under load 10 mN, 25 mN, and 50 mN of (a) NiTi-M, (b) NiTi-A, (c) NiTiHf-A, (d) NiTiHfPd-A, (e) NiTiHfPd-A (400), (f) NiTiHfPd-M (600), (g) NiTiHfCu-M (500), and (h) NiTiHfCu-M (600) alloys. The solid line represents the spherical indentation data, while the dash line is from Berkovich indentation response.

Figure 4.8 shows the L-D curves of these eight specimens under high load levels from 100 to 500 mN. Comparing two NiTi alloys, Figure 4.8a and Figure 4.8b show that D_{max} of NiTi-A is lower than NiTi-M under both indenters even though higher loads were applied, which agrees well with low load results in Figure 4.7. D_{max} of NiTiHf-M at all peak loads in Figure 4.8c are lower than the ones of NiTi-M under both indenters, but

slightly higher than NiTi-A when comparing the Berkovich results. At higher load level, the L-D curves of NiTiHfPd alloys in Figure 4.8 shows similar behavior as in Figure 4.7, where the D_{max} of NiTiHfPd-A and NiTiHfPd-A (400) at each peak load are the lowest among all the alloys, and NiTiHfPd-M (600) shows slightly higher D_{max}. The L-D curves shown in Figure 4.8g and Figure 4.8h also indicate a higher D_{max} than NiTiHfPd alloys at each load level. However, the L-D curves of NiTiHfCu-M (500) and NiTiHfCu-M (600) alloys are almost same at each peak load under both indenters shown in Figure 4.8. The deformation behavior of two similar martensitic (non-superelastic) alloys under high indentation load are mainly plastic deformation that results in similar indentation depth.

As shown in Figure 4.8, the spherical indentation response of these alloys during unloading do not show high work/depth recovery above 100 mN, and the unloading curves are linear-like type. It is clear that work/depth recovery at high loads shown in Figure 4.8 is lower than the ones at low loads shown in Figure 4.7. Such difference is mainly due to the increased plastic deformation at higher loads. It should also be noted that as the load increased, D_{max}/R ratio increases and gets closer to the spherical contact limit of 0.5. Table 4.2 lists D_{max}/R of NiTi, NiTiHf, NiTiHfPd and NiTiHfCu alloys at selected load levels from 10-500 mN, and the results with $D_{max}/R > 0.5$ are marked in red and they exceed the spherical contact limit. With the spherical indenter tip radius of 5 μm, above 250 mN, it is difficult to compare the material strength using the D_{max} due to the increased plasticity.

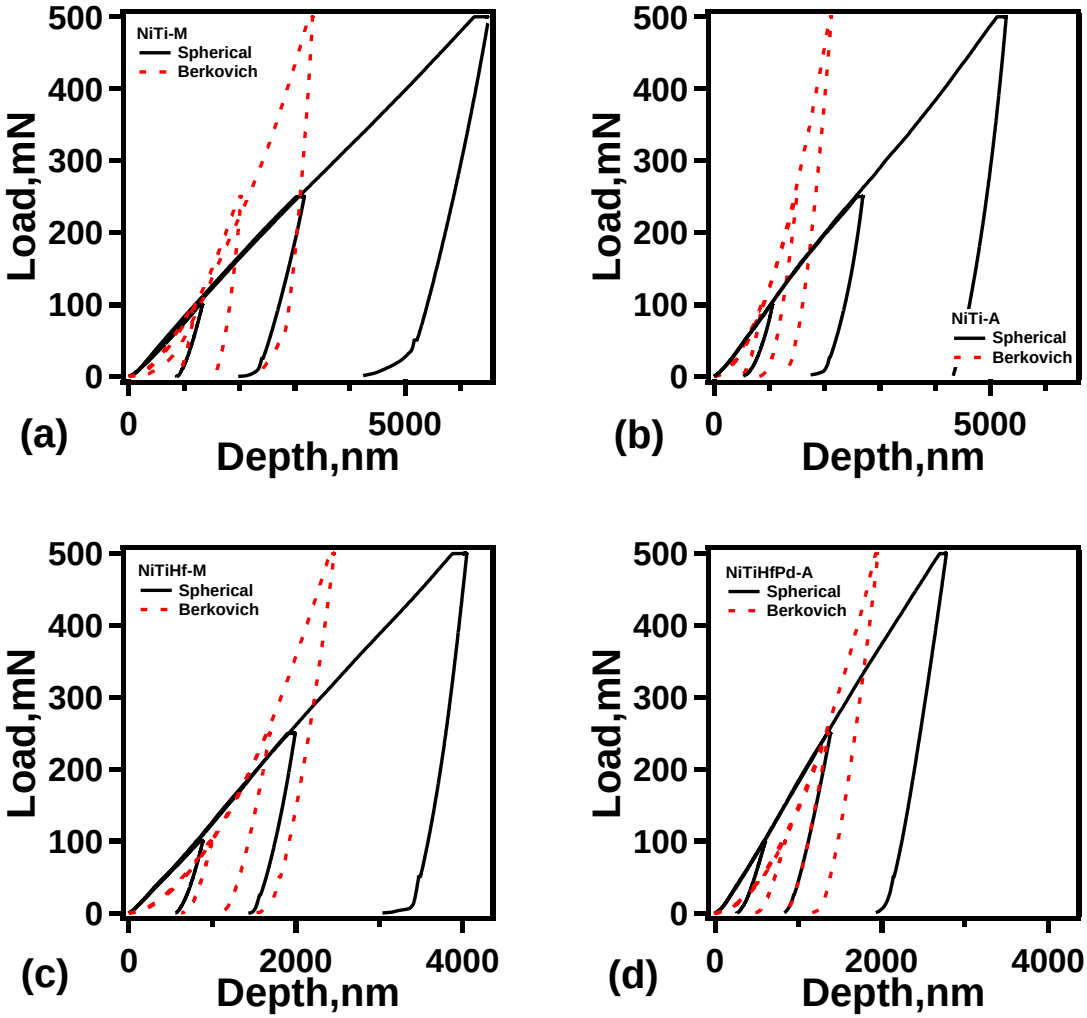
NiTi-M
Spherical
Berkovich
Load,mN
Depth,nm
(a)
NiTi-A
Spherical
Berkovich
(b)
NiTiHf-M
Spherical
Berkovich
(c)
NiTiHfPd-A
Spherical
Berkovich
(d)

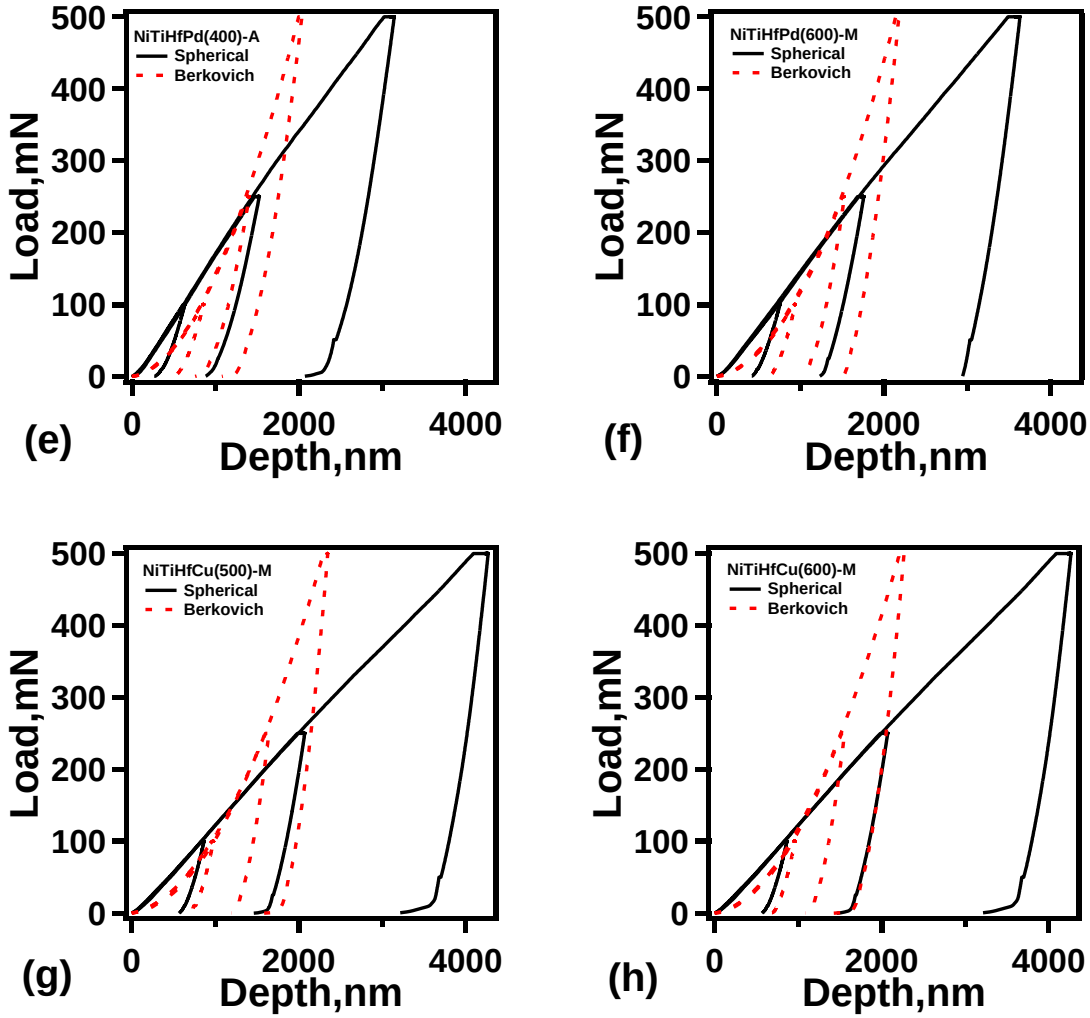

Figure 4.8: Spherical and Berkovich nano-indentation L-D response under load 100 mN, 250 mN, and 500 mN of (a) NiTi-M, (b) NiTi-A, (c) NiTiHf-A, (d) NiTiHfPd-A, (e) NiTiHfPd-A (400), (f) NiTiHfPd-M (600), (g) NiTiHfCu-M (500), and (h) NiTiHfCu-M (600) alloys. The solid line represents the data from spherical tip, while the dash line is from Berkovich tip.

Another feature that needs to be noted in Figure 4.8 is that the L-D curves of Berkovich indentation response start to converge at load levels above 100 mN, results in a lower D_{max} than spherical response at each peak load. In order to observe the detail indentation depth change with load and indenter tip shape, Figure 4.9a and 4.9c show the D_{max} and D_r of theses alloys as a function of selected load levels, respectively, for both spherical and Berkovich results. The 2.5 μm depth marked in Figure 4.9a indicates the

maximum spherical contact depth limit. It can be easily observed that all alloys show spherical contact when load is below 250 mN except NiTi alloys. In order to observe detail information of depth change on the low load level, Figure 4.9b shows the zoom of D_{max} and Figure 4.9d is the zoom of D_r. The D_{max} and D_r of all alloys from Berkovich and spherical indenters are increase with indentation loads shown in Figure 4.9. Compared to spherical results in Figure 4.9a, D_{max} from Berkovich are higher for load levels up to100 mN, and lower at higher loads. The converge behavior from Berkovich in D_{max} is well observed in Figure 4.9d. However, in Figure 4.9d, the D_r of spherical are higher than Berkovich except the case in NiTi-A. Thus, higher depth recovery under spherical than Berkovich can be concluded.

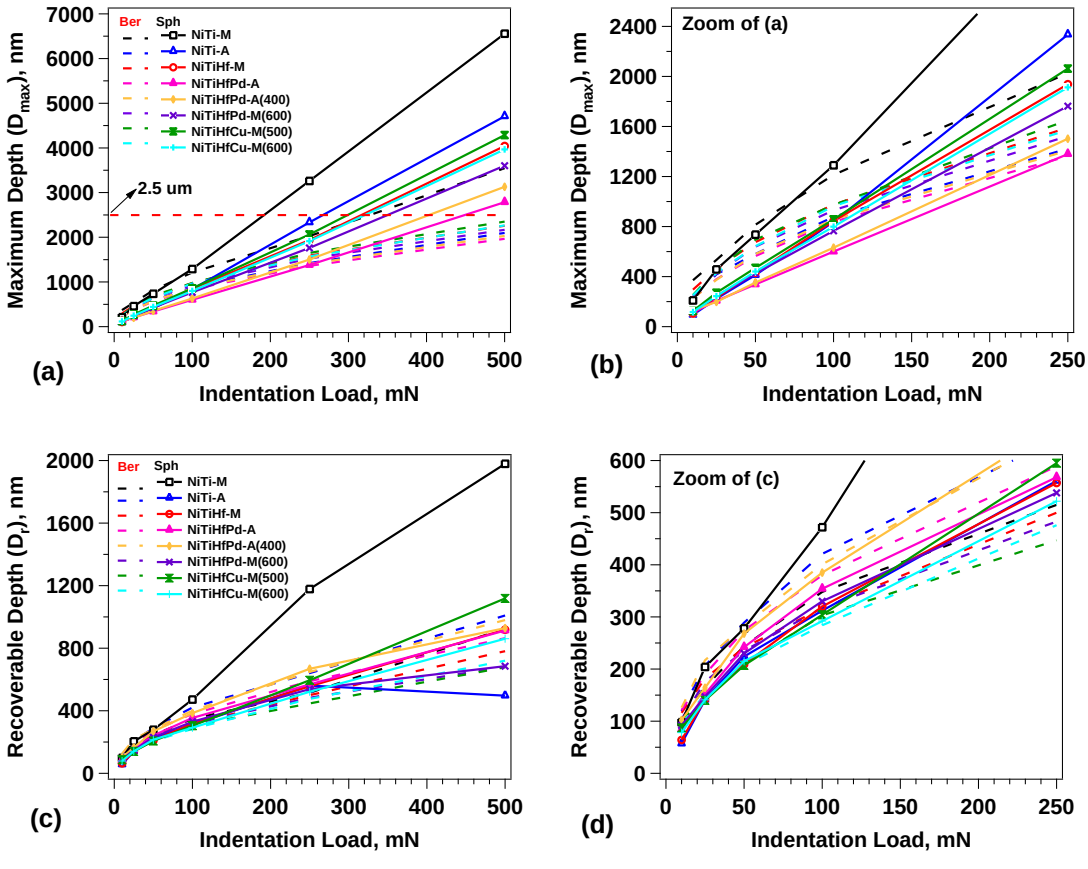

Figure 4.9: (a) Maximum indentation depth (D_{max}), (c) recoverable depth (D_r), of all alloys as a function of selected loads under both spherical and Berkovich indenters. (b) is the zoom of (a) till load level of 250 mN, and (d) is the zoom of (b) at same load level.

4.5.2. Discussion

4.5.2.1.Indentation Hardness

Figure 4.10a shows the indentation hardness (H) response as a function of D_{max}/R under spherical indenter tip. The dimensionless scale of D_{max}/R is used to so that the results shown in Figure 4.10a does not depend on indentation tip radius. As shown in Figure 4.10a, spherical indentation hardness (H_{Sph}) of fused silica increases with depth from 2.72 to 8.35 GPa as the load increases from 10 to 500 mN. This is in good agreement with previous results [79]. Depth/load dependent spherical indentation hardness behavior of NiTi and NiTiHfPd alloys were reported in our previous study [110] where it was demonstrated that hardness increases with indentation depth due to the increase in the transformed region and plastic deformation during loading. It was studied that hardness increases with indentation depth for spherical indentation in elastic-plastic solids with work hardening [121]. However, the spherical indentation response of iridium alloys show that the spherical indentation size effect on hardness was not expected to depend on indentation depth but to the tip radius based on the strain gradient plasticity theory analysis [122].

Figure 4.10a shows that the indentation hardness increases with D_{max}/R and then saturates at loads higher than 250 mN. H_{Sph} of NiTiHfPd-A is the highest with the values ranging from 5.5 to 8.9 GPa, while NiTi-M shows the lowest H_{Sph} values from 2.0 to 6 GPa. H_{Sph} of NiTiHfPd alloys are higher than the other alloys. NiTiHf-M have lower H_{Sph} than NiTiHfPd alloys but higher H_{Sph} than the other alloys. The spherical hardness values

of NiTi-based alloys agree well with the Vickers hardness results shown in Table 4.1, and the mechanical response. Copper shows the lowest hardness of around 1 GPa, and the hardness slightly increases with indentation depth. It is instructive to note that the H_{Sph} of SMAs under each load (e.g. 100 or 250 mN) may be governed in a curve fitting as the dash lines shown in Figure 4.10a. The curve fitting was only applied to the loads above 100 mN for the sake of clarity.

Figure 4.10b shows the indentation hardness response as a function of D_{max} under Berkovich indenter tip. The Berkovich hardness (H_{Ber}) decreases with D_{max} for all NiTi-based alloys. This is the opposite behavior observed from spherical hardness results. H_{Ber} of SMAs decreases dramatically till the load level of up to 50mN or D_{max} of up to 1000 nm. Further increase in depth or load results in modest decrease in hardness. The reduced H_{Ber} with indentation depth was firstly observed in single crystal copper [123], where the hardness decreases dramatically first from 2.7 to 0.9 GPa as the depth changes from 100 to 1000 nm, and then it saturates with depth. A simple model was provided to explain the observed behavior by using the geometrically necessary dislocations combined with the theory of strain gradient plasticity on Cu and Ag [124]. It has also suggested that the H_{Ber} of a material is less depth dependent if the material is intrinsically hard (e.g. fused quartz, where the hardness is about 9 GPa at depth of 200 nm and 8.97 GPa at depth of 600 nm, shows independence depth behavior shown in Figure 4.10b). In this study, both the spherical and Berkovich hardness of copper used were found to be depth independent. The indentation hardness of a Berkovich indenter can be defined as Eq (4.4):

$$H = \frac{P_{max}}{A_c} = \frac{P_{max}}{24.5{D_c}^2} \tag{4.4}$$

Where, A_c is the projected contact area at peak load P_{max}, D_c is the contact depth. Pile-up is observed if $D_c/D_{max} > 1$, while sinking-in is observed if $D_c/D_{max} < 1$. Although D_c/D_{max} depends on the ratio of yield stress to Young's modulus (Y/E) and work hardening component "n" under a Berkovich tip [79], it was found that sinking-in always observed for Hertzian elastic contacts whereas piling-up occurs for rigid-plastic contacts [121]. Numerical studies also show that the piling-up does not occur in SMAs when the martensite plastic yield stress is over 1300 MPa [125]. The current study of NiTi-based SMAs under both indenters showed only sink-in behavior ($D_c/D_{max} < 1$). The equation (2) suggests that the measured hardness values under Berkovich indenter (Figure 4.10b) are larger than the real values.

Table 4.4 summarizes the minimum and maximum hardness of SMAs from spherical and Berkovich indentation responses. It can be observed that most of the minimum or maximum indentation hardness values from Spherical indentation are slightly higher than the ones measured from Berkovich indentation. The Vickers hardness values shown in Table 4.1 are very close to the minimum values measured from Berkovich at high loads. This is expected since the Vickers is also a test with sharp indenter as the indentation with Berkovich tip. The H_{Ber} values measured at low load 10 mN shows the highest hardness values, and it is higher than the Vickers hardness. This behavior can be attributed to the fact that the measurement of H_{Ber} depends on the projected contact area A_c at peak load, while the Vickers hardness measurement depends on the residual projected area A_r. The A_c is always smaller than A_r [126] even at the same peak load.

The H_{Ber} of NiTi-A is close to the hardness of NiTiHfPd-A (400). The high H_{Ber} of NiTi-A is inconsistent with either the mechanical bulk measurements or the Vickers

hardness results. Moreover, the L-D curves in Figure 4.7 and Figure 4.8 under Berkovich indenter cannot provide a clear relationship between strength level by using the D_{max}, therefore, it is not recommend to use Berkovich indenter to characterize the hardness behavior of materials with high elasticity. Another feature need to be noted is that H_{Ber} of all SMAs lies in between fused silica and copper, while it was not observed in spherical response.

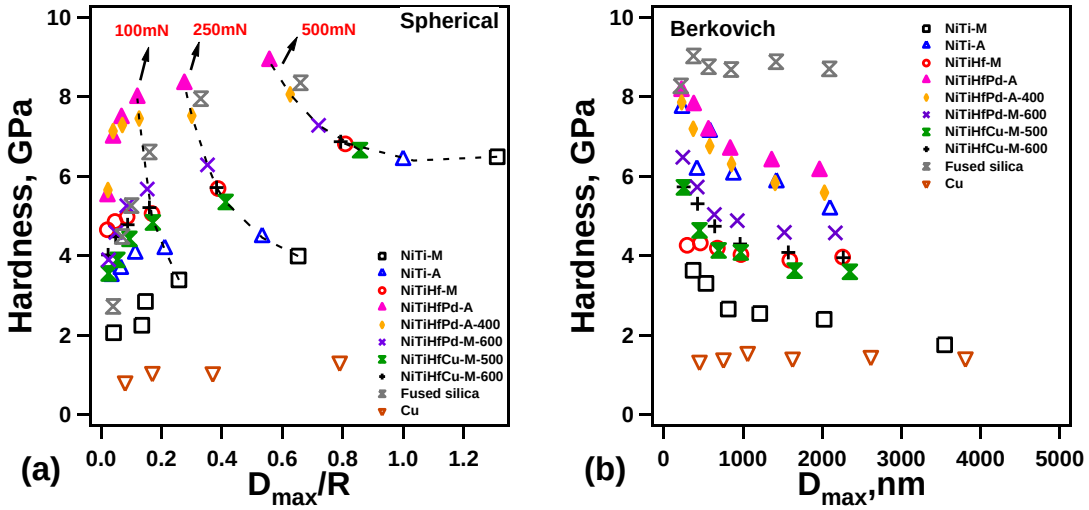

Figure 4.10: (a) Indentation hardness vs. D_{max}/R relationship of all alloys under spherical tip, and (b) hardness vs. maximum depth D_{max} relationship of all alloys under Berkovich tip. Data was calculated at selected peak load of 10, 2, 50, 100, 250 and 500mN. To be noted, H vs. D_{max}/R shows indentical trend with H vs. D_{max}, thus, it is comparable with other results under different tip sizes.

Table 4.4: The minimum and maximum indentation hardness of eight alloys from spherical and Berkovich indentation response, and also the hardness measurements from Vichkers.

Hardness (Gpa) min/max	NiTi-M		NiTi-A		NiTiHf-M		NiTiHfPd-A		NiTiHfPd-A(400)		NiTiHfPd-M(600)		NiTiHfCu-M(500)		NiTiHfCu-M(600)	
Spherical	2.01	6.48	3.47	6.39	4.95	6.81	5.48	8.88	5.65	8.06	3.9	7.28	3.54	6.66	4.01	6.87
Berkovich	1.75	3.63	5.14	7.7	3.88	4.31	6.11	8.13	5.58	7.86	4.57	6.48	3.59	5.72	3.95	5.73
Vickers	2.19		2.37		3.39		6.43		5.32		4.81		4.14		3.97	

4.5.2.2.Work Recoverable Ratio

A proportional linear relationship between the ratio of W_{irr}/W_t and D_f/D_{max} was proposed by finite element calculation, and such behavior was also confirmed by spherical indentation experiment results on standard materials such as Cu, Al, and W [79]. However, for SMAs, the work recoverable ratio η_w (w_e/w_t) can more accurately predict the superelasticity and shape recovery than the measurement of D_f/D_{max} as the former was integrated from loading and unloading curves, whereas the latter was determined from single point measurements. The η_w is 1 for a pure elastic response and 0 for the pure plastic behavior.

Figure 4.11a shows the average work recoverable ratio of NiTi-based alloys under spherical tip and plotted as a function of D_{max}/R. It shows a dramatically decrease in work recovery for $D_{max}/R< 0.2$, followed with a gradually decrease till $D_{max}/R=0.5$, and then it is almost depth independent due to high plastic deformation at high load levels. Work recoverable ratios of NiTiHfPd-A and NiTiHfPd-A (400) are about 1 at the low load of 10 mN as they show pure elastic response. Since the spherical indentation response of work recovery of selected eight SMAs overlap each other in a decrease trend, a curve fit was employed and used in the figure. It should be noted that the behavior shown in Figure 4.11a could be tip radius dependent. Nevertheless, it provides a simple way to predict work recovery ratios. The results from fused silica and copper were also shown in the figure. Their work recovery ratios decrease with depth as well. At the low load of 10 mN, fused silica shows full recovery as NiTiHfPd-A, while copper has very low η_w of 0.09. The η_w of copper with a 10 μm spherical indenter tip were previously reported and are added to the Figure 4.11a for comparison. It is clear that η_w increases with decreased depth.

As the sharp rigid Berkovich indenter is forced into the surface of material, the geometrically necessary dislocations and plastic deformation are required for the shape change. η_w decreases slightly with depth till 500 nm that might be attributed to the limitations of Berkovich tip manufacturing and the wear. The indenter tip might not be in a perfect sharp shape but instead it can be approximated as an spherical tip when the indentation depth is very small [127]. Therefore, the Berkovich results at low loads/depths can be assumed to be closer to spherical indentation results and include more elastic deformation compared to the indents at high loads/depths. As shown in Figure 4.11b, for all the alloys, after the initial drop, the η_w from Berkovich indentation is almost independent with indentation depth/load. The results are in good agreement with the previous results reported in superelastic NiTi alloys [12]. Fused silica has higher η_w but the same behavior as SMAs, while copper shows depth independent behavior for all the load levels. Ni *et al*. [92] also studied depth dependent Berkovich response of copper, where their results are in good agreement with the current work. It is instructive to mention, under both spherical and Berkovich responses shown in Figure 4.11, fused silica is the highest limit and copper is the lowest limit, while SMAs lie in between.

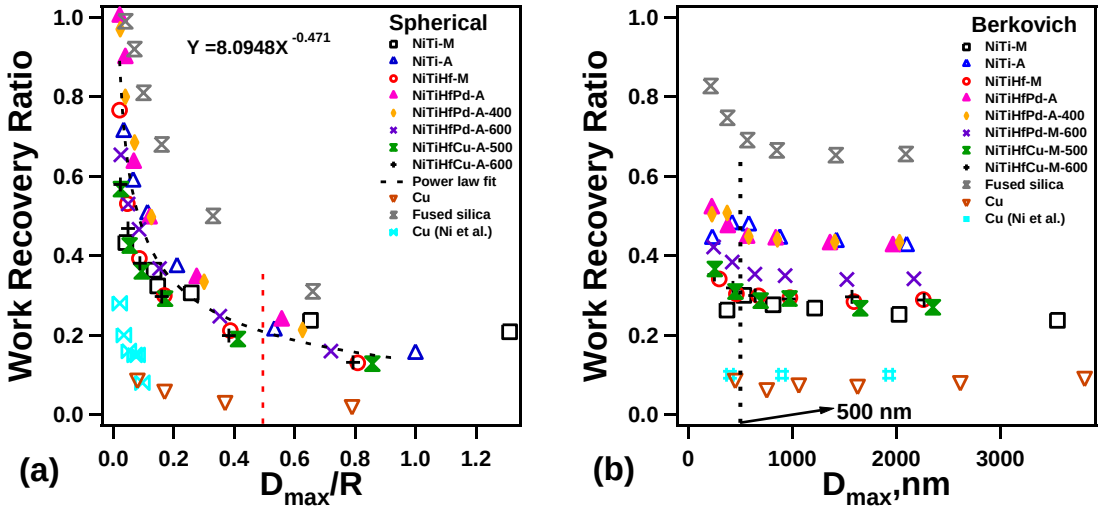

Figure 4.11: Indentation work recovery ratio against the (a) D_{max}/R of all alloys under spherical tip, as well as the copper from Ni et al [79], (b) D_{max} of all alloys under Berkovich tip, as well as the copper from Ni et al [92]. Data was calculated at selected peak load of 10, 2, 50, 100, 250 and 500mN.

4.5.2.3.Young's Modulus

For a typical superelastic SMA, there are four deformation stages during spherical indentation; i) indentation of a single austenite phase at low loads/depth, and the measured modulus is expected to be equal to E_A; ii) a partial transformation zone where austenite partially transforms to martensite; iii) a fully transformed martensite zone is surrounded by partially transformed martensite but still enclosed in austenite; iv) plastic deformation of existing phases. Contact mechanism differs during spherical indentation of a non superelastic and martensitic SMA, where it has three deformation stages: 1) a single martensite phase at low loads/depths and the measured modulus is expected to be close to E_M; 2) a zone where martensite reorientation occurred; 3) plastic deformation of existing zones. Thus, the modulus change with depth is expected if the existing phases of the material have different moduli.

Figure 4.12 shows the indentation modulus of NiTi-based alloys as a function of depth. Equation 4.5 is the relationship between the indentation modulus E and the reduced modulus E_r (measured from indentation unloading curve).

$$E = \frac{(1-\nu^2)}{\frac{1}{E_r}-\frac{(1-\nu_i^2)}{E_i}} \tag{4.5}$$

where υ is Poisson's ratio for the specimen. E_i and υ_i are respectively the elastic modulus and Poisson's ratio of indenter. In this study, E_i of 1000 GPa and ν_i of 0.07 were used for the rigid diamond indenters.

Figure 4.12a shows the indentation modulus as a function of D_{max}/R from spherical indentation experiments for all NiTi-based alloys. Prior to the yield point of spherical contact at $D_{max}/R=0.5$, indentation contact modulus of NiTiHf-based alloys initially decreased till $D_{max}/R=0.2$, and then became depth insensitive, while modulus of NiTi alloys were almost depth independent. The initial modulus decrease of NiTiHf can be attributed to the stress-induced phase transformation and the difference of the elastic moduli of austenite and martensite phases. Such depth dependent behavior of indentation modulus was studied by finite element analysis on superelastic NiTi alloys [128], where it was reported that the measured indentation modulus strongly depends on the elastic moduli of the two phases, indentation depth, forward transformation stress, transformation hardening coefficient and the maximum transformation strain. The depth independent behavior of NiTi alloys can be attributed to the low strength and high plastic deformation. The decrease of modulus with indentation depth of martensitic SMAs may be attributed to difference of moduli of twinned and detwinned martensite phases and indenting multiple grains instead of single grain at small indentation depths. It was shown before that elastic moduli of

austenite and martensite phases are orientation dependent for NiTiHfPd alloys [129]. However, it should be noted that the modulus of a SMA measured from indentation experiment is neither the elastic modulus of austenite nor martensite phase, but depends on various parameters such as indentation depth [128], tip radius, E_M , and E_A. The modulus of copper as a function of depth was also shown in Figure 4.12a where it shows a similar behavior as SMAs. However, the modulus of fused silica increases with depth till $D_{max}/R=0.2$, and then saturates at 60 GPa at higher depths.

Figure 4.12b shows the Berkovich indentation modulus as a function of indentation depth, where indentation moduli of all alloys initially decrease with depth (or with load till up to 50 mN) and then saturate. The modulus decrease rate under Berkovich indenter is not as sharp as spherical response. The decrease of modulus under Berkovich indenter can be attributed to the geometry of sharp tip, where plastic deformation inevitably occurs during indentation. Furthermore, as discussed in section 4.5.2.2, the Berkovich tip might not be in a perfect shape, that results in the modulus decrease at low load levels, as observed in spherical indentation results. The Berkovich modulus of fused silica is depth insensitive and has a constant value of 72 GPa which agrees well with the values reported in literature [95] while the modulus of copper decreases slightly with depth.

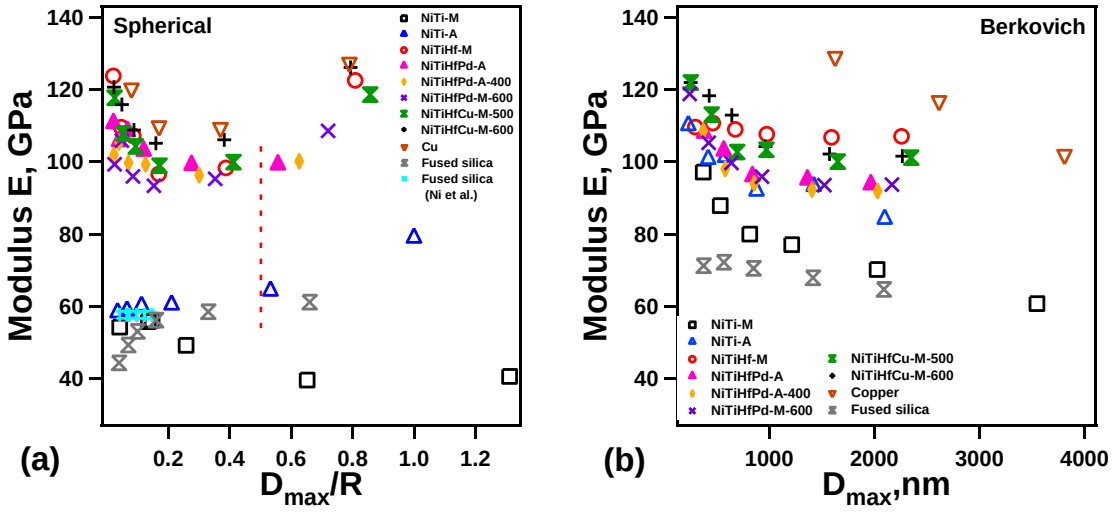

Figure 4.12: Calculated indentation modulus E as a function of (a) D_{max}/R of all alloys, as well as fused silica and Al from Ni et al [79], (b) D_{max} of all alloys under Berkovich indenter. Data was calculated at selected peak load of 10, 25, 50, 100m, 250 and 500mN.

4.5.3. Conclusion

1. The spherical and Berkovich indentation responses of NiTi-based alloys are highly load/depth and composition dependent. Moreover, the indentation responses also depend on whether the material show superelasticity or not.

2. Spherical indentation hardness of NiTi-based alloys increase with indentation depth due to the increase in the transformed region and plastic deformation during loading, while Berkovich indentation hardness decreases with depth due to increased plastic deformation. Vickers hardness of NiTi-based alloys are close to the Berkovich hardness (minimum value) since Vickers measurement is a test with sharp tip. Moreover, spherical indenter shows the highest hardness values compared with sharp indenters (Vickers and Berkovich).

3. All three indenter tips show good agreement on indentation hardness that superelastic NiTiHfPd alloys are the strongest, and martensitic NiTi is the weakest. It can be concluded that superelastic behavior of SMAs can help to increase the indentation

hardness within the same family.

4. Indentation work recoverable ratios of NiTi-based alloys are extremely depth dependent in spherical indentation and they decrease substantially with indentation depth while they are depth independent under Berkovich indenter.

5. Superelasticity increases the work recoverable ratio can be observed under both spherical and Berkovich indenters. Moreover, spherical indenter can produce more work recoverable ratio than Berkovich, where a perfect work recoverable ratio (spherical) was obtained on superelastic NiTiHfPd alloys under low load. The lower load, the higher work/depth recovery can be observed.

6. The modulus from spherical and Berkovich indentation responses of NiTi-based alloys initially decrease with indentation depth and then saturates at larger depth/load. Both measurements show similar value in contact modulus for all alloys, except NiTi alloys. Moreover, superelasticity does not affect on the modulus under both spherical and Berkovich indenters.

5 TEMPERATURE DEPENDENT INDENTATION RESPONSE OF AGED NITIHF SHAPE MEMORY ALLOYS

5.1.Introduction

Indentation techniques have been performed on shape memory alloys during the last few decades due to their unique properties of shape memory effect (SME) and superelasticity (SE). Previous nanoindentation studies on SMAs were mostly conducted at room temperature to determine indentation hardness, depth recovery ratio and superelasticity [12, 14, 91, 92]. It was found that in superelastic SMAs, the indentation depth imposed by spherical indenters can be almost fully recovered upon heating, while deformation induced by a Berkovich indenter can only be partially recovered [12]. Moreover, the instrumented indentation method was also used to demonstrate indentation induced two-way shape memory effect [130]. The potential and current applications of NiTi alloys include electronic devices, medical tools, and biomedical applications due to the relatively low TTs (near body temperature) [131]. The low hysteresis is desired for actuator applications [132], while the high hysteresis is suitable for coupling [133] and damping applications [134]. Thus, precise tools need to be characterized in nano/micro scale since the mechanical properties are different between nano/micro and macro size measurements [135].

High temperature nanoindentation measurements have been conducted on, for example, fused silica [95-98], aluminum [97], Titanium [96], copper [97], NiTi [82, 100-103], and Ni-based super alloys [99]. A number of researchers have studied the indentation response of NiTi at elevated-temperatures to identify mechanical characteristics. Shastry *et al*. [104] demonstrated the differences between indentation responses of the austenite

and martensite of two NiTi alloys as a function of temperature. The indentation-induced SE effect was also characterized under Berkovich indenter at elevated temperature by Zhang et al. [82], and they observed that the microscopic superelastic behavior of NiTi thin-film occurred at about 100 K above the austenite transformation finish temperature (A_f) which was due to the high hydrostatic pressure under the indenter. The ternary NiTiHf and NiTiCu thin films were also tested in regards to nano-indentation at high temperature where it confirms that the superelastic behavior can exhibit up to 20 at.%Hf because the microstructure of above 20 at.%Hf might contain a high volume fraction of non-transformable precipitates [101]. The addition of Hf to NiTi alloys can stabilize the SMA and SE behaviors to higher temperatures and it has been quite widely investigated with the mechanical bulk testing. However, the difficulty and cost of alloying bulk NiTi alloys with ternary additions have made indentation technique more efficient and economical for characterizing local mechanical properties of ternary NiTi-based SMAs, especially when the compositional study in these systems are employed.

In this chapter, $Ni_{50.3}Ti_{29.7}Hf_{20}$ alloy was selected since it has higher strength than other NiTi-based alloys and shows superelasticity at high temperatures of about 200 °C [111, 112, 136, 137]. The main aim of this study is to characterize the mechanical behavior of NiTiHf alloys as a function of temperature under a spherical indenter in micro-scale and compare that with compression experiments at macro-scale.

A tip radius of 25 µm diamond spherical indenter was mounted on a heating shield which reduces the heat transfer from indenter to the surrounding. All specimens were bounded to the hot stage using a thermally conductive ceramic paste. When the temperatures of the indenter and the specimen were stabilized, indentation was made using

a peak load (500 mN and 2000 mN) with a loading rate of 5mN/s. Following a dwelling period of 10s at the peak load, the indenter was unloaded at the same rate of 5mN/s. The spherical indenter and the specimen were heated simultaneously with a maximum heating rate of 8 °C/ min. The temperature range of indentation experiments was from 30 to 340 °C with 10 °C intervals, while 5 °C intervals were used between the phase transformation temperatures range to obtain accurate phase transformation behavior. Detailed information can be found in each section of this study. At each temperature, indentation experiments were repeated three times at the same load. Figure 5.1 is the optical microscope image of the indentation location and indentation size. The average indent size is about 20 μm and the space between each indent is around 200 μm.

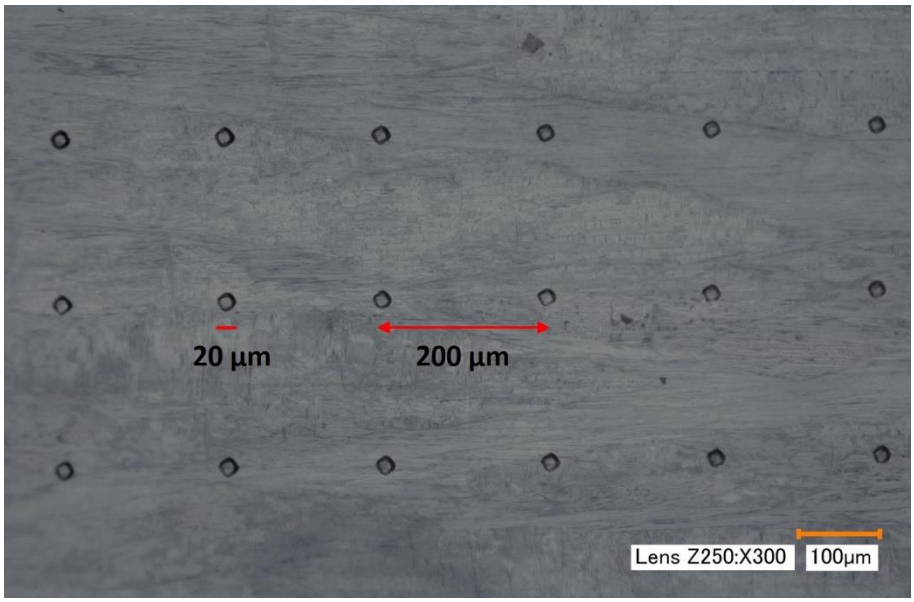

Figure 5.1: Optical microscopy image of aged $Ni_{50.3}Ti_{29.7}Hf_{20}$ after indentation experiments.

5.2.Shape Memory Behavior and Phase Diagram of aged $Ni_{50.3}Ti_{29.7}Hf_{20}$

A typical SMA exhibits phase transformation between martensite and austenite phases, depending on applied stress and temperature. There are typically five stages of deformation: I) ($T<M_f$) martensite reorientation (MR), no recovery; II) ($M_f<T<A_f$) phase transformation (PT) behavior or variant reorientation (VR) with no or partial recovery; III) ($A_f<T<T_{SE}$) superelastic (SE) behavior with full recovery; IV) ($T_{SE}<T< M_d$) phase transformation with plastic deformation (PD) results in partial recovery or no recovery; V) ($M_d<T$) plastic deformation of austenite with no recovery. Here, the M_d temperature is defined as the maximum temperature at which SMAs can no longer transform to martensite. It should be noted that in all stages, the recovery amount will depend on the level of maximum loading strain/stress. The stages above were determined by assuming that the loading is only continued until the end of phase transformation.

The compressive response of NiTiHf as a function of temperature is shown in Figure 5.2a and a detailed phase transformation diagram of bulk NiTiHf alloy is presented in Figure 5.2b, where critical stresses for martensite reorientation, martensitic transformation or slip are shown as a function of temperature. Critical stresses, σ_c^T, are extracted from Figure 5.2a by using the tangent method. It should be noted that one sample was tested from 120 to 400 °C with temperature intervals of 20 °C. At 120 °C, which is below M_f of 171 °C, no strain recovery was observed upon unloading. However, SME strain was attained once heating the sample above the A_f. As shown in the Figure 5.2a, the critical stress for the martensite reorientation decreases with increasing temperature from 120 °C to 180 °C, presumably due to the increased mobility of internal twins and martensite plate boundaries. Only partial/no recovery was observed upon unloading below M_s and

deformation can be fully recovered while heating above A_f. At the temperature close to M_s of 186 °C, the stress-strain curve after the initial linear elastic deformation starts to exhibit a plateau like response at 180 °C which can be attributed to the initial stage of stress-induced martensite (SIM) being formed during loading, and followed by a small amount of elastic recoverable strain upon unloading. Between temperatures of 200 to 240 °C, the stress required for martensite transformation increases with temperature, and perfect superelasticity is observed due to the superelasticity. However, partial recovery occurs at 260 °C since the martensite transformation and plastic deformation occurs simultaneously while the testing temperature is approaching M_d. From 280 to 320 °C, the sample shows no recovery, but critical stress increases, suggesting that there is still phase transformation. Beyond 320 °C, σ_c^T decreases and no recovery is observed due to the fact that plastic deformation of austenite takes place before martensite transformation, thus shape recovery cannot be found. The slope of the plateau region (due to phase transformation and/or plastic deformation), m_p, is positive from 180 to 300 °C. At 320 °C, it is almost zero and then it is negative at higher temperatures. The critical stress decreases with temperature due to the conventional softening in metals at high temperature. Thus, the M_d temperature was determined to be around 300-320 °C, as it was the highest temperature that phase transformation was still observed. Due to the difficulty of determining the temperature where only plastic deformation takes place in stress-strain curves of SMAs, the intersection method is generally used. The M_d can determined to be 280 °C by this method.

Figure 5.2b can be divided into five stages (I, II, III, IV, V) based on the deformation behavior. The transformation temperatures obtained from DSC measurements are also shown in Figure 5.2b, where the M_s is very close to the intersection (lowest) point

between the line of low critical stress and stress induced phase transformation. From M_s to T_{SE}, σ_c^T increases linearly with temperature. From T_{SE} to M_d, σ_c^T increases and above M_d, σ_c^T decreases with temperature. The decrease of the stress can be explained by the increase in plasticity of austenite and dislocation mechanisms start to dominate.

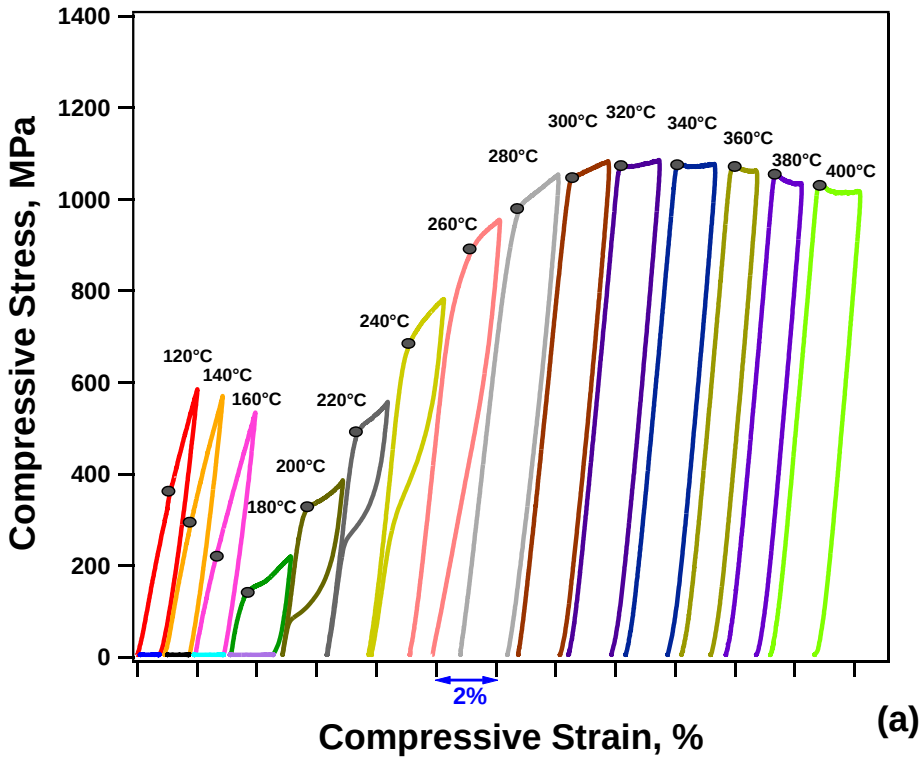

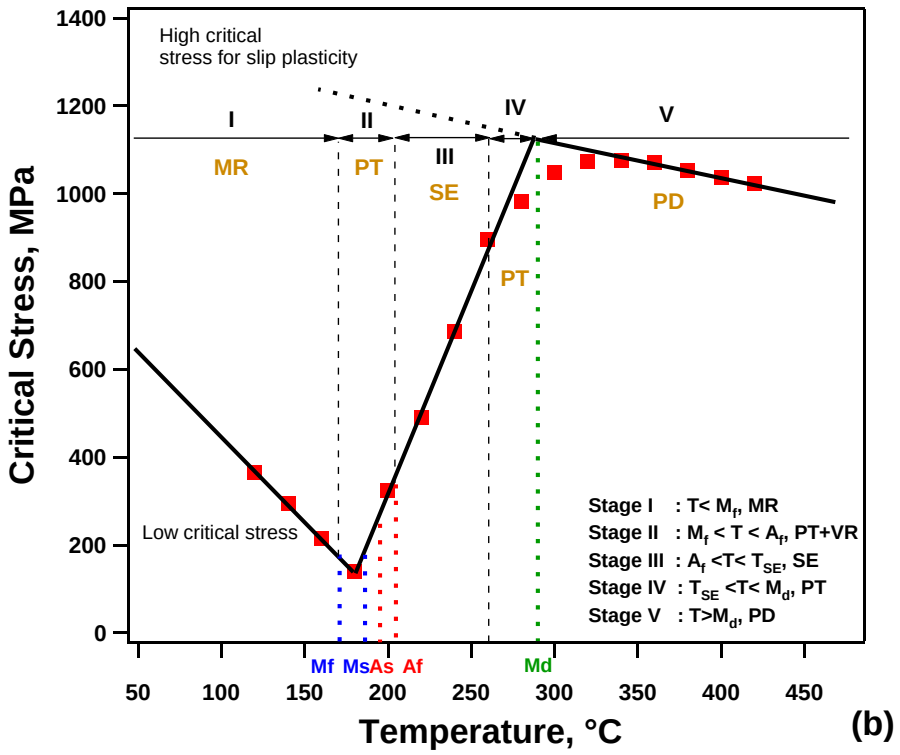

Figure 5.2: Phase transformation diagram of aged $Ni_{50.3}Ti_{29.7}Hf_{20}$. The stress-strain curves showing temperature dependency of the critical stress (a); relationship of critical stress and transformation temperatures (b).

5.3.Load-Depth Curves of Aged NiTiHf Shape Memory Alloys under Heating and Cooling

Figure 5.3 shows the load-displacement (L-D) curves for the spherical indentation response of the NiTiHf alloy at temperatures between 30 and 340 °C. The data obtained at other temperatures are omitted in the figure for clarity. Figure 5.3a and Figure 5.3b are the L-D curves during heating and cooling processes, respectively. Most of the recent indentation studies with elevated temperatures only focused on the heating process [99, 101, 105, 138, 139] to characterize the austenite start and finish temperatures of NiTi alloys and the cooling process has not been studied. Thus, a systematically and stepwise cooling process was followed after heating at 340 °C to identify the martensite phase

transformation temperatures during cooling. At each temperature, indentations were repeated three times at different locations. For clarity, the first indentation load-displacement curve obtained at each temperature is displayed. The aged NiTiHf alloy starts in the pure martensitic phase in heating and austenite phase in cooling. It is instructive to note that these TTs extracted from the indentation response are not expected exactly match the TTs obtained from DSC as they would depend on the applied indentation force. Thus, the TTs obtained from indentation response will be named as M_s^I, M_f^I, A_s^I, and A_f^I throughout the text.

In the beginning of the heating process as shown in Figure 5.3a, the maximum indentation depth (D_{max}) slightly increases with temperature from 120 to 200 °C, and then increases substantially at 205 °C due to the phase transformation. The increase of the maximum indentation depth indicates that the material is becoming softer which is consistent with the indentation hardness value displayed in Figure 5.3 at each temperature. However, the hardness value does not change much with temperature, which might be due to the complex phases during phase transformation. Wood *et al*. [101] also observed an increase in D_{max} below A_f^I. Above 205 °C, in Figure 5.3a, austenite phase was formed completely and both the maximum depth of indentation and the remnant depth (D_R) decreased, suggesting that the superelastic strain recovery mechanism was operating upon unloading only around A_f^I, but was absent at lower temperatures (below A_s^I). Meanwhile, the indentation hardness increased dramatically from 205 °C (2.8 GPa) to 230 °C (3.47 GPa), indicating austenite phase formation. Thus, we conclude that the 205 °C is the austenite finish temperature, which matches with the A_f^I (205 °C) measured from DSC of the bulk aged NiTiHf. The L-D curve at 230 °C provides the clearest evidence of the

transition between superelastic and non-superelastic behavior, since it exhibits more depth recovery than the ones observed below 205 °C. With further increase in temperature to 330 °C, the maximum indentation depth decreases dramatically, resulting in an increase in hardness due to dislocation-mediated plastic deformation.

Figure 5.3b shows the L-D relation as a function of temperature during the cooling process. Starting at 330 °C, either the hardness or the maximum indentation depth is the same as that measured during the heating process. This may be caused by the variations in indentation locations or grain orientations. However, during the cooling process, the sample was in pure austenite initially and deformed plastically because the temperature was above M_d. The maximum indentation depth increased slightly as the temperature decreased to 225 °C, where a small decrease in indentation hardness synchronously appeared even though temperature dropped by 100 °C. A sudden increase in D_{max} and decrease in hardness happened when the temperature decreased to 180 °C, where the lowest value of hardness and modulus were observed during the cooling process. Such a decrease also indicates the decrease in superelasticity. Furthermore, temperature below 180 °C shows an increase in D_{max} with decreasing temperature, corresponding to the decrease in hardness. Here, 180 °C is the M_S^I during cooling, which is in good agreement with the M_s (185 °C) measured from DSC. These predictions from the indentation L-D response of heating and cooling process will be discussed further in the next section.

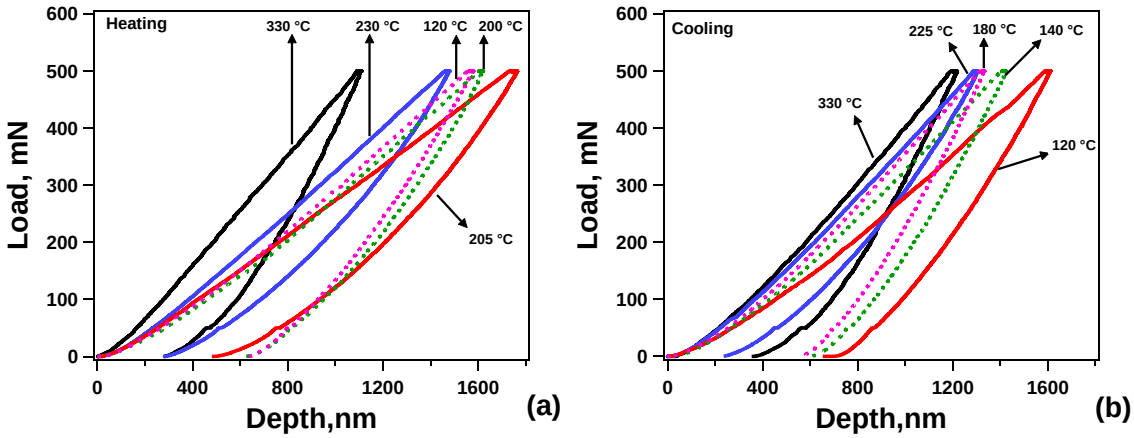

Figure 5.3: Spherical indentation responses of typical load-displacement relationships at selected temperature. Load-displacement curves of NiTiHf under load 500 mN with (a) heating process from 28 °C to 340 °C, and (b) cooling process from 340 °C to 28 °C.

5.4.Work Recoverable Ratio Vs. Temperature

To gain further understanding of the L-D curves, we evaluate indentation hardness, modulus and recoverable ratio as a function of temperature. Indentation response of measured hardness and elastic moduli values are not the same as that of either martensite or austenite phases. Although indentation can cause phase transformation under the indenter, hardness and elastic moduli with a wide range of temperature cannot define the actual state of transforming phases or other stages (SE, plasticity, and martensite reorientation) accurately. However, the work/depth recovery or remnant depth recovery as a function of temperature are often used to characterize the transformation temperature and superelasticity [91, 101]. In this article, the work recovery method was used to define the stages of mechanical deformation.

Figure 5.4a and Figure 5.4b show the temperature dependent spherical indentation response on work recovery and maximum indent depth (D_{max}) of NiTiHf under peak load

500 mN, respectively. With a complete thermal cycling between 30 and 340 °C, indentation data was collected and the average work recovery ratio and maximum indent depth were analyzed from three repeated experiments. In order to interpret the data more accurately, error bars representing the standard deviation were shown at temperature. Based on the general behavior of SMAs under stress and temperature, the indentation work recoverable ratio of aged NiTiHf alloy as a function of temperature can also be separated into stages during heating and cooling, shown in Figure 5.4a.

Starting with the heating process in pure martensite, martensite variant reorientation takes place during indentation with a peak load of 500 mN. The work recoverable ratio slightly decreases from 0.61 to 0.54 while the temperature increases from 30 to 180 °C (this temperature range was selected as stage I). In this temperature range, the maximum depth increased incrementally in Figure 5.4b. An enormous increase (15 %) of work recovery was observed from 190 to 225 °C. Such an increase in the work recovery ratio is due to the increased volume fraction of austenite phase in the matrix that results in SIM. As shown in Figure 5.4a, the work recoverable ratio exhibits a sudden jump between 200 and 205 °C, manifesting the completion of austenite phase transformation at 200 °C. Therefore, the temperature range from 190 to 200 °C was selected as stage II (PT/VR), and 190 °C is the A_s^I, since it shows the lowest work recoverable ratio and it starts to increase at higher temperatures. It should be noted that D_{max} increased abruptly from 180 to 205 °C, as shown in Figure 5.4b. It suggests that the volume fraction of the material that undergoes VR or SIM increased in this section. This observation can be attributed to the low critical stress requirement for SIM or VR around the transformation temperatures as shown in Figure 5.2. Since the applied force is kept constant, lower critical stress resulted in larger

volume fraction of transformation or variant reorientation. Above A_f^I, a dramatic increase in work recovery was observed, where the highest value indicates the best superelastic behavior upon unloading at 225 °C (T_{SE}). Thus, the range 205-225 °C was defined as the superelastic region (stage III). Comparing with the superelastic behavior of the bulk sample, perfect superelasticity was found from 200-240 °C, as shown in Figure 5.2a, which agrees well with the indentation results. It should be kept in mind that although the stress is constant in the compression test of the bulk sample, the stress is distributed in spherical indentation tests. Thus, in spherical indentation, a range of stress is applied to the material. It can also be argued that the end temperature of region III (T_{SE}) will depend on the indenter size and the applied load. The higher load and lower indenter diameter will result in lower T_{SE}. It was observed in another NiTiHf sample that when the applied load was increased from 500mN to 2000mN, T_{SE} was decreased by 25 °C (the results are not shown here). From Figure 5.4b, it can be determined that D_{max} decreases above 205 °C and the intersection method can be used to find that 225 °C is the deflection point, above which the decrease in D_{max} is linear. Above 225 °C, the work recoverable ratio starts to decrease with temperature up to 300 °C, and then saturates to a constant work recoverable ratio of 0.61. Such a decrease is attributed to the increased plastic deformation of austenite phase with partial superelasticity, and it also indicates phase transformation. It should be noted that 300 °C was determined to be the M_d since there is no phase transformation at higher temperatures. Therefore, 225-300 °C was selected as stage IV (SIM+PD) and 300-340 °C is the stage V where only the plasticity will occur. D_{max} decreases linearly from 205 to 320 °C and then increases with temperature.

Following the heating experiments, the work recovery ratio as a function of temperature with cooling process was also divided into five stages as shown in Figure 4a with triangle marks. During cooling from 340-225 °C, the indentation work recoverable ratio shows almost identical hysteresis with the heating experiments as the material is completely austenite. On the other hand, D_{max} during cooling is lower than the D_{max} during heating. The difference can be attributed to the fact that since indentation measures local properties, orientation of grains could affect the results. Heating and cooling experiments are conducted at two different regions of a polycrystalline sample, thus, D_{max} will depend on the orientation of the grains. Since work recoverable ratio is almost identical, this behavior indicates the deformation of austenite has a good agreement of heating and cooling experiments. Therefore, the stage V and IV of cooling process are in the same temperature range as with the heating process. Between 225 -205 °C, the work recovery ratio decreases linearly while D_{max} increases with decreasing temperature and the results are identical to the heating curve. This stage was selected as stage III (SE). The results between 205 to 180 °C are similar to the previous region, however, the changes are more pronounced as the results deviate from to heating curve. This behavior is expected since during cooling, initially, austenite is stable fully from A_f^I to M_s^I and partially from M_s^I to M_f^I, while during heating, martensite is stable from M_f^I to A_s^I and then partially from A_s^I to A_f^I. Thus, decreasing temperature in this region, increases the volume fraction of austenite phase that goes through SIM but decrease of martensite to austenite back transformation. At 180 °C, the lowest work recovery ratio and the maximum D_{max} were observed during cooling experiments, and it was selected as the M_s^I where SMAs show the lowest critical stress. From 180-160 °C, the work recoverable ratio increases sharply and maximum depth

decreases pronouncedly compared to the values below 160 °C. Such a temperature range was determined as stage II (PT). The martensite finish temperature M_f^I was determined to be around 160 °C because the work recoverable ratio below that temperature (160 °C) did not increase much which means that the martensite phase transformation was fully completed. The smooth and steady curve below 160 °C shows a similar behavior as the heating process where martensite reorientation takes place, named as stage I. Comparing with the heating and cooling loops in Figure 4a, the small hysteresis between 175 to 205 °C attributes to the thermal hysteresis of austenite and martensite.

It should be noted that shape memory and material properties are highly orientation dependent [112, 129]. The average grain size of the tested material was around 50 μm, the indenter tip radius was 25 μm, the maximum contact diameter was around 20 μm and the distance between indent centers was 200 μm. Thus, it is possible that some indents will occur inside the grains while others could hit the grain boundaries. Therefore, the indentation response at three varied locations gives different L-D results depending on the grain orientations. It is clear that the error bars in stage IV and V are relatively higher than other stages, especially during the heating process. Thus, it might be suggested that grain orientations are affecting the plastic deformation more than the shape memory response. There are only a few exceptions to this where the error bar at A_s^I during heating is large since the indentation response will highly depend on whether, the material is austenite, martensite or mixed phase.

Nevertheless, the transformation temperatures of M_s^I, M_f^I, A_s^I, $A_f^I$from indentation response of work recovery can be determined as 180 °C, 160 °C, 190 °C, 200 °C, respectively. Moreover, T_{SE} can be determined as 225 °C but it should be noted that it will

depend on the loading level as well as indentation tip radius. Lastly, M_d can be determined to be around 300 °C by using indentation technique. These values are in good agreement with the DSC and bulk mechanical compression results. However, it should be noted that, indentation techniques can be used to determine local properties. Such a new method of characterizing shape memory properties has several advantages than the conventional method: i) the programming interface of indentation technique makes the experiments easier and saves time for researchers, ii) it can be employed as nondestructive testing of bulk SMAs, iii) the small scale measurement economically saves material, iv) it can precisely determine local properties at nano or macro scales, v) the purging system avoids oxidization at high temperature.

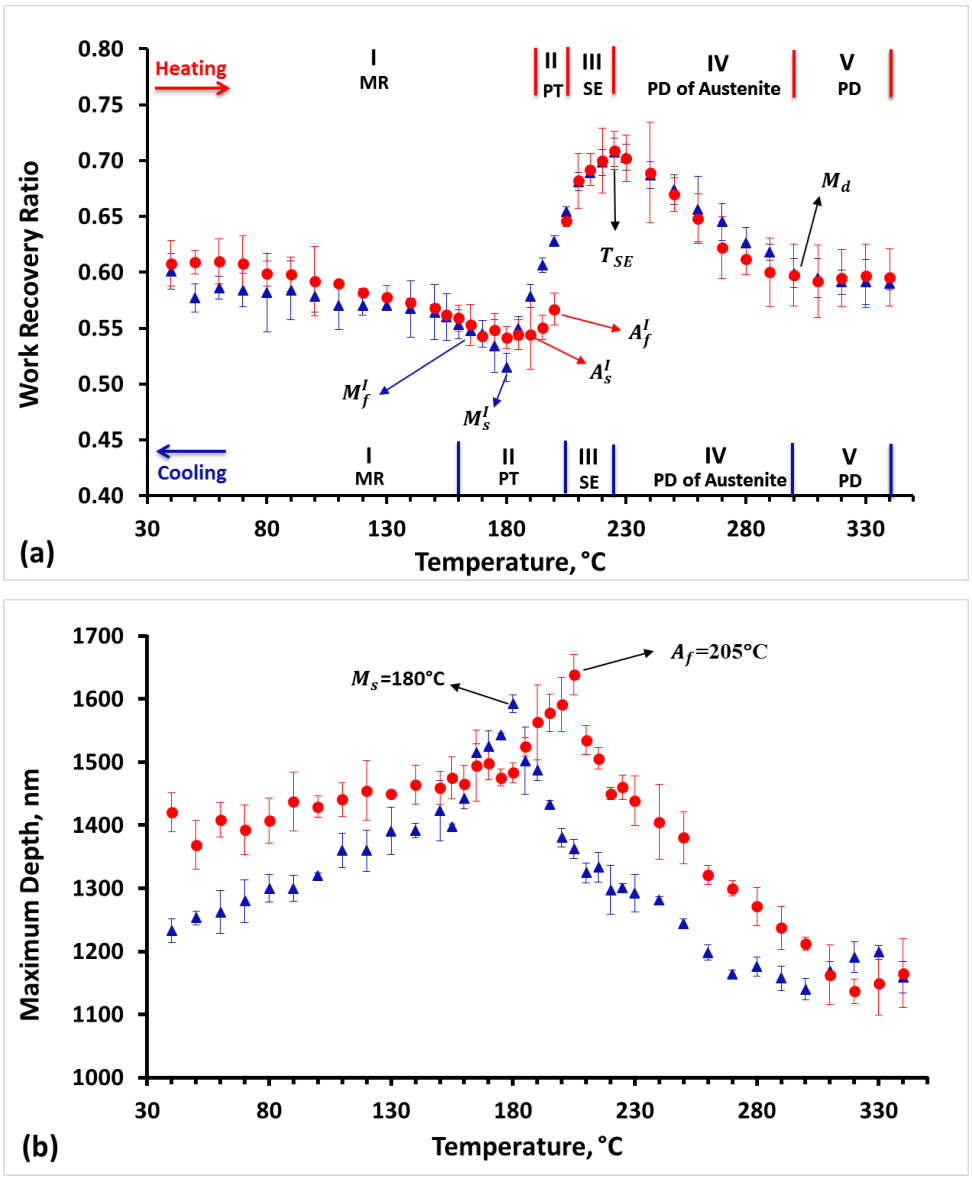

Figure 5.4: Spherical indentation response of work recovery ratio (a), maximum indentation depth D_{max} (b) as a function of temperature under 500 mN of NiTiHf with heating process from 28 °C to 340 °C marked as circle and cooling process from 340 °C to 30 °C marked as triangle.

5.5.Conclusion

1. Spherical indentation technique was used to determine the temperature-dependent behavior of an aged high temperature NiTiHf shape memory alloy. This method can be used for detecting the transformation temperatures and deformation stages.
2. The temperature, which shows the highest D_{max} during heating and cooling, corresponds to A_f^I and M_s^I, respectively, while the temperature at the lowest work recoverable ratio during heating and cooling corresponds to A_s^I and M_s^I, respectively.
3. The temperature with the highest work recoverable ratio is the T_{SE}, and M_d can be determined at the temperature where the work recoverable ratio starts to saturate after T_{SE}.
4. This simple indentation technique is capable of quantitative characterization at micro- and nano-meter scales of shape memory materials.
5. The results obtained using the indentation method are in a good agreement with the phase transformation behavior performed on bulk materials under compression and transformation temperatures obtained by DSC.

6 LOAD AND TEMPERATURE DEPENDENT INDENTATION RESPONSE OF NITI-BASED SHAPE MEMORY ALLOYS

6.1.Introduction

In our previous study, it has been shown that the temperature dependent work recoverable ratio response can be used to measure local superelastic deformation and determine phase transformation temperatures of an aged NiTiHf alloy. In this chapter, in addition to temperature, the effects of applied load on the indentation response of an unaged $Ni_{50.3}Ti_{29.7}Hf_{20}$ alloy are investigated. Moreover the change of work recoverable ratio, hardness and modulus as functions of temperature and load level were revealed. The unaged NiTiHf used in this study has lower strength than the aged NiTiHf alloys, but it has higher strength and TTs than NiTi alloys [111]. For this alloy, a fully recoverable SME strain of 2.4 % was observed at 500 MPa, while almost 3 % of superelastic strain was found at 180 °C with associated stress as high as 1000 MPa [112].

Shape memory behavior of $Ni_{49.9}Ti_{50.1}$, $Ni_{50.8}Ti_{49.2}$ and $Ni_{50.3}Ti_{29.7}Hf_{20}$ alloys were investigated as a function of temperature at two different load levels, and compared with Ti-6Al-4V only with cooling process. NiTi alloys were selected based on whether the material was predominantly martensite ($Ni_{49.9}Ti_{50.1}$) or austenite ($Ni_{50.8}Ti_{49.2}$) at room temperature. The main aim of this study is to characterize the local mechanical behavior of NiTi-based alloys as a function of temperature under a spherical indenter in nano- and micro-scale and compare that with compression experiments at macro-scale.

The nominal compositions of the NiTi-based alloys were $Ni_{50}Ti_{50}$, $Ni_{50.8}Ti_{49.2}$ and $Ni_{50.3}Ti_{29.7}Hf_{20}$. Ti (Ti-6Al-4V) (McMaster, USA) was selected as a standard material for

comparison since its mechanical properties are known. The $Ni_{50.3}Ti_{29.7}Hf_{20}$ alloy was inductively melted using a graphite crucible and cast into a 1 inch diameter copper chill mold. The ingot was homogenized at 1050 °C for 72 h and extruded at 900 °C with a 7:1 reduction in area. For simplicity, Ti-6Al-4V, $Ni_{49.9}Ti_{50.1}$, $Ni_{50.8}Ti_{49.2}$ and $Ni_{50.3}Ti_{29.7}Hf_{20}$ are denoted as (Ti), (NiTi), (50.8NiTi) and (NiTiHf), respectively, throughout the text.

The start and finish temperatures of martensite and austenite (M_s, M_f, A_s, A_f, respectively) of NiTi and NiTiHf alloys are measured from DSC responses and shown in Table 6.1. Vickers hardness values of the alloys measured at room temperature are also added to Table 6.1. NiTi and NiTiHf are martensite while 50.8NiTi is austenite at room temperature.

Table 6.1: Transformation temperatures observed from DSC and Vickers hardness at room temperature for Ti, NiTi, 50.8NiTi and NiTiHf alloys.

Sample Name	**Ms** (°C)	**Mf** (°C)	**As** (°C)	**Af** (°C)	Phase at room temperature	Vickers hardness (GPa)
$Ni_{49.9}Ti_{50.1}$ (NiTi)	78	45	85	122	Martensite	2.19
$Ni_{50.8}Ti_{49.2}$ (50.8NiTi)	-15	-34	-4	10	Austenite	2.37
$Ni_{50.3}Ti_{29.7}Hf_{20}$ (NiTiHf)	120	109	140	150	Martensite	3.39
Ti-6Al-4V(Ti)	--	--	--	--	--	2.66

6.2. Temperature and Load Effect of as-received NiTiHf Shape Memory Alloy under Spherical Indenter

6.2.1. Load-Depth Curves of as-received NiTiHf Shape Memory Alloys under Heating and Cooling

Figure 6.1 shows the selected load-displacement (L-D) curves for the spherical indentation of the NiTiHf at temperatures between 30-320 °C. Figure 6.1a and Figure 6.1b are the L-D curves during heating and cooling processes under low load of 500 mN, respectively, while Figure 6.1c and Figure 6.1d are corresponding to the high load of 2000 mN for heating and cooling, respectively.

As shown in Figure 6.1a under 500 mN, the maximum indentation depth (D_{max}) slightly increases with temperature from 30 to 160 °C, and then increases substantially at 180 °C. The increase in D_{max} can be attributed to the fact that the alloy transforms from martensite to austenite with increased temperature (A_s=167 °C from DSC). The increase of the maximum indentation depth results in decreased indentation hardness. Above 180 °C, austenite phase was formed completely and both the D_{max} and the remnant depth (D_R) decreased dramatically with temperature, resulting in increased in hardness. The D_{max} at 240 and 320 °C are almost identical as shown in Figure 6.1a, however, the D_R at 240 °C is smaller than at one at 320 °C, which implies higher work/depth recovery at 240 °C. The temperature of the maximum indentation depth can be selected as the A_f [140]. In this study, the maximum D_{max} was obtained at 180 °C which is in good agreement with the A_f obtained from DSC (186 °C). The slight difference can mainly be attributed to the fact that large temperature interval of 20 °C was used during indentation experiments.

Figure 6.1b shows the selected L-D curves of spherical indentation during cooling from 320 to 30 °C under 500 mN. At 320 °C, the sample was austenite initially and deformed plastically because the temperature was high and above M_d [140]. D_{max} increased slightly as the temperature decreased from 320 to 260 °C. With further cooling, D_{max} increased sharply till 160 °C and resulted in the highest D_{max} (lowest hardness). The temperature (160 °C) which resulted in maximum D_{max} is the martensite start temperature which is in good agreement with the M_s (160 °C) determined from DSC. When the temperature decreased from160 to 140 °C, D_{max} decreased dramatically and further cooling to 30 °C resulted in slight decrease of D_{max}. The indentation temperature 140 °C can be selected as the martensite finish temperature which is in good agreement with the M_f (134 °C) obtained from DSC measurement.

Spherical indentation response of NiTiHf was also investigated with higher load level (2000 mN) for both heating and cooling and results are shown in Figure 6.1c and Figure 6.1d, respectively. The L-D curves obtained under 2000 mN (Figure 1c and 1d) results in a similar behavior as in low load cases but with higher depth levels. It has been determined that maximum D_{max} is at 180 °C during heating and 160 °C during cooling under high load which are the same temperatures under low load.

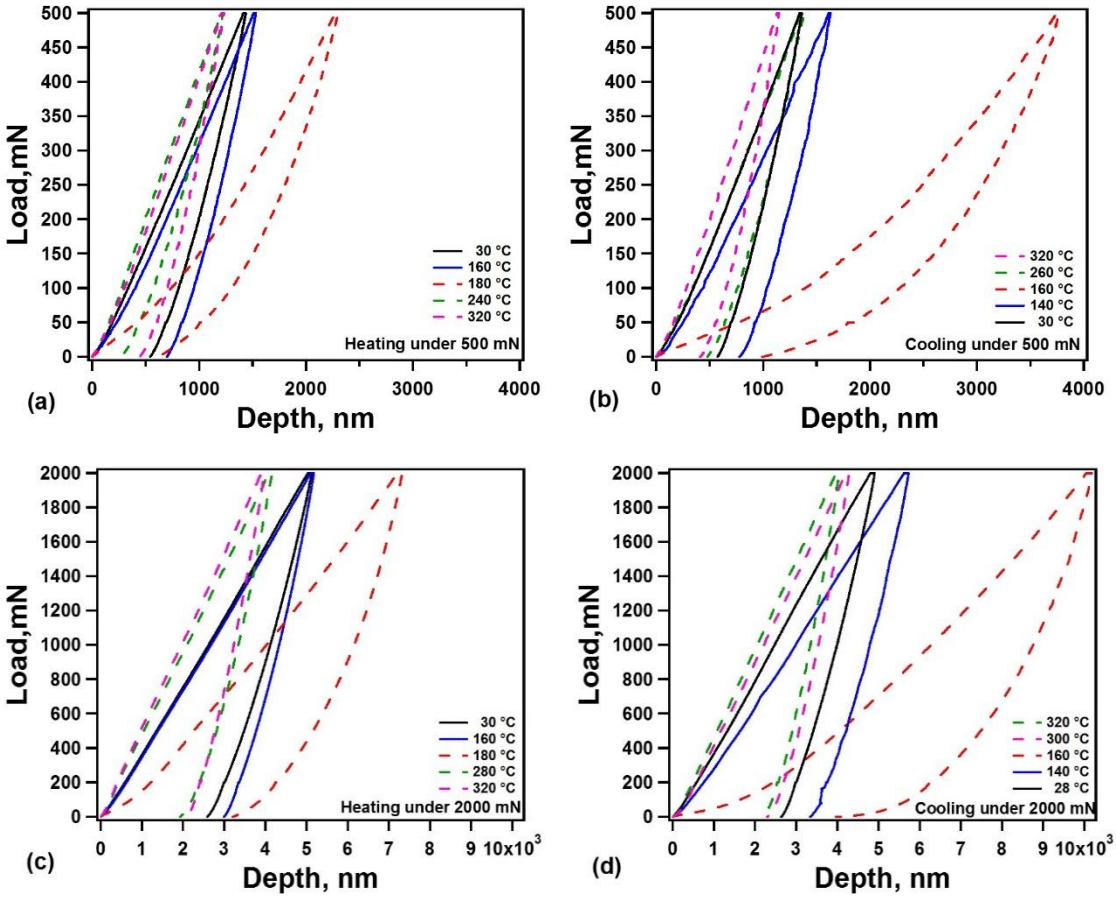

Figure 6.1: Spherical indentation responses of typical load-displacement relationships at selected temperature. Load-displacement curves of NiTiHf under load 500 mN with (a) heating process from 30 to 320 °C, (b) cooling process from 320 to 30 °C; and under 2000 mN with (c) heating process from 30 to 320 °C, (b) cooling process from 320 to 30 °C.

6.2.2. Discussion

The indentation hardness, modulus and recoverable ratio of NiTiHf were determined as functions of temperature and load. It should be noted that hardness and elastic moduli values of martensite or austenite phases are different. The work/depth recoveries are often used to characterize the transformation temperatures and superelasticity [91, 101, 140].

6.2.2.1.Indentation Work Recovery

Figure 6.2a and Figure 6.2b show the temperature dependent η_w of NiTiHf under peak loads of 500 mN and 2000 mN, respectively. During heating, the η_w slightly decreases from 0.54 to 0.49 when the temperature increases from 30 to 160 °C (this temperature range was selected as stage I). A large increase (16 %) in η_w was observed from 160 to 220 °C. This increase of η_w can be explained by the increased volume fraction of austenite phase in the matrix that results in stress-induced martensitic (SIM) phase transformation. The sudden jump of η_w between 160 and 180 °C manifests the completion of phase transformation (PT) at 180 °C. Temperature range from 160-180 °C was selected as stage II (PT/VR), and the temperature with the lowest η_w during heating can be selected as A_s^I which is 160 °C while 180 °C can be selected as the A_f^I. From 180 to 220 °C, η_w increases, the highest η_w during heating was observed at 220 °C (T_{SE}) indicating the best superelastic behavior. Thus, the range 180-220 °C was defined as the superelastic region (stage III). Above 220 °C, the η_w decreases with temperature up to 280 °C, and then saturates to a constant value of 0.59. The decrease in η_w is attributed to the increased plastic deformation resulting in partial superelasticity. The 280 °C was determined to be the M_d since there is no phase transformation or superelasticity can be observed at higher temperatures. Therefore, temperature range from 220-280 °C was selected as stage IV (SIM+PD) and 280-320 °C was denoted as the stage V where only the plasticity will occur.

The work recoverable ratio results during cooling are shown by the triangle marks. As shown in Figure 6.2a, the cooling process follows the same path as the heating except the temperature hysteresis between 120 and 180 °C. During cooling from 320 to 180 °C, the η_w values are the same as the ones obtained during heating as the material is completely

austenite in both cases. Therefore, the stages III, V, and IV of cooling process are in the same temperature range as the heating process. The η_w decreases from 0.62 to 0.47 when indentation temperature decreases from 180 to 140 °C. The lowest η_w was obtained at 140 °C which can be selected as M_s. With Further cooling from 140 to 120 °C, a sudden increase in η_w occurred at 120 °C (select as M_f) due to the martensite phase transformation. Thus, temperature range from 180 to 120 °C is selected as stage II during cooling, and temperature below 120 °C is stage I.

The temperatures with the lowest η_w during heating and cooling can be selected as A_s^I and M_s^I, respectively, while the temperature with the highest D_{max} (lowest hardness) during heating and cooling are determined as A_f and M_s, respectively [140]. Thus, M_s^I, M_f^I, A_s^I, A_f^I are determined as 140°C, 120°C , 160 °C and 180 °C from the indentation results under 500 mN.

At the higher load level of 2000 mN, shown in Figure 6.2b, heating and cooling curves are very similar to the ones obtained under low load level of 500 mN. However, the deformation stages are not clear as under 500 mN and it is difficult to determine the phase transformation temperatures, T_{SE} and M_d. During heating, work recovery slightly decrease with temperature till 160 °C and increase sharply from 160-180 °C. Above 180 °C, it decreases again with temperature till to 320 °C, and the work recovery ratio at 320 °C is same as the one measured at 30 °C. The cooling process follows the same path as the heating except the temperature hysteresis between 140 and 180 °C. Thus, from Figure 2b, it is possible to determine M_s^I as 140 °C, A_s^I as 160 °C, and T_{SE} as 180 °C, but not M_d. Under 2000 mN, the T_{SE} is lower than the one observed under 500 mN, which suggest that the end temperature of region III (T_{SE}) will depend on the applied load [140]. The higher

load will result in lower T_{SE}. M_f cannot be identified under 2000 mN since sudden increase in η_w was not observed during cooling. The high load level of 2000 mN and large indentation temperature interval are the main reasons for not being able to determine M_f and A_f^I. The η_w decreases with temperature above 180 °C for both cooling and heating, and it does not saturate to a constant value even at a high temperature of 320 °C. As shown in Figure 6.2, the η_w under 2000 mN is lower than the ones under 500 mN due to the additional plasticity at higher load level. The hysteresis loop between the temperatures 140 to 180 °C is well observed in SMAs.

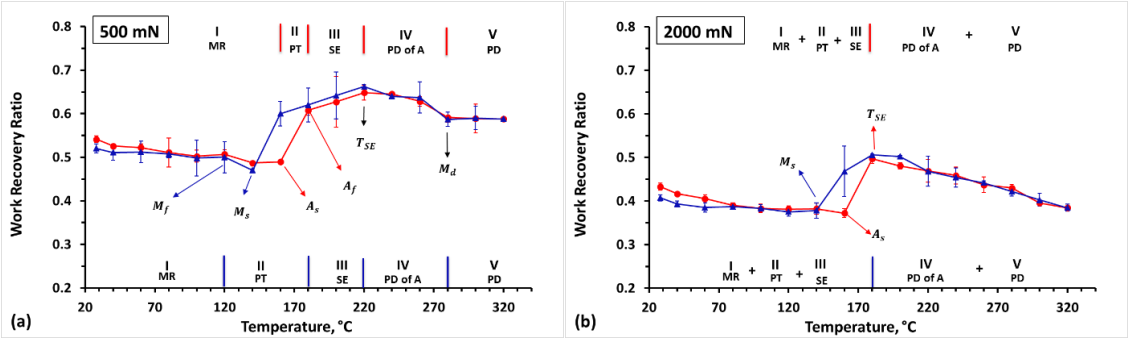

Figure 6.2: Spherical indentation response of work recoverable ratio as a function of temperature for as-received NiTiHf alloy under load (a) 500 mN, (b) 2000 mN.

6.2.2.2. Indentation Hardness

The change in indentation hardness of NiTiHf with temperature and load is studied. It should be noted that the indentation hardness is inversely proportional to the maximum indentation depth, where the lowest hardness occurs at the highest D_{max}, and vice versa.

Figure 6.3a and Figure 6.3b are the temperature dependent indentation hardness response of NiTiHf under 500 mN and 2000 mN, respectively. During heating (marked as circle) from 30 to 160 °C, hardness slightly decreases. At 180 °C, hardness drops

considerably. The sudden decrease in hardness can be related to the phase transformation from martensite to austenite. Thus, 160 °C can be selected as A_s^I, and 180 °C can be considered as A_f. These temperatures are in good agreement with the A_s^I and A_f^I determined from work recovery ratio results shown in Figure 6.2. Above 180 °C, the hardness increases dramatically until 260 °C due to the increased volume fraction of transformed austenite phase. The highest hardness value of 4.3 GPa is observed at 260 °C (T_{SE}). With further heating, hardness decreases due to increased plastic deformation and decreased volume fraction of phase transformation.

The hardness results during cooling are shown by the triangle marks. During cooling from 320 to 260 °C, the hardness values are the same as the ones obtained during heating as the material is completely austenite in both cases. Therefore, the stages V and IV of cooling process are in the same temperature range as the heating process. The hardness decreases from 4.28 GPa to 1.30 GPa when the temperature decreases from 260 to 160 °C. The lowest hardness occurs at 160 °C, at M_s^I as it shows the highest D_{max} during cooling. With further cooling from 160 to 120 °C, the hardness increases suddenly due to the martensite phase transformation. Thus, 120 °C is chosen as M_f^I. Below 120 °C, indentation hardness is almost constant at 3.3 GPa (stage I). M_s is determined as 140 °C by using the work recovery ratio method, but it is determined as 160 °C by using the hardness method. Thus, it can be argued that the M_s^I would occur in between the temperature range of 140-160 °C. It should be noted that work recovery ratio depends on the elasticity and superelastic response of the alloys during the entire loading and unloading process while hardness is only determined by the maximum depth at the end of loading. Thus, the methods used here are different in nature and same results are not expected.

The hardness values at high load are determined to be slightly higher than the ones under low load which is in good agreement with previous observations in NiTi-based alloys [110]. It is clear to see the transition points shown as M_s^I, M_f^I, A_s^I, and A_f^I are identical with the ones found under 500 mN. However, it is not possible to distinguish the stages III and IV under high load. This can be attributed to the increased plastic deformation at higher load that impedes the superelasticity.

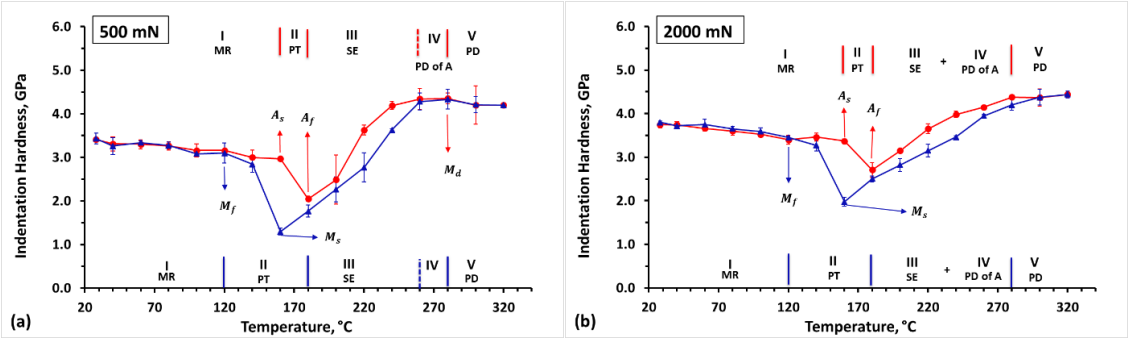

Figure 6.3: Spherical indentation response of hardness as a function of temperature for as-received NiTiHf alloy under load (a) 500 mN, (b) 2000 mN.

6.2.2.3. Indentation Contact Modulus

Figure 6.4 shows the contact modulus of NiTiHf alloy as functions of temperature and load. During heating from 30 to 160 °C, the modulus is almost constant as only variant reorintation of marteniste occurs (selected as stage I). Modulus drops dramatically at 180 °C which can be attributed to the phase transformation of sample from martensite to austenite. Thus, 160 °C is selected as A_s^I where the modulus starts to decrease with temperature, while 180 °C is selected as the A_f^I which shows the lowest modulus during heating. These two values match well with the findings from work recoverable ratio and hardness results. Above 180 °C, the modulus incrementally increase with temperature. It

should be noted that the modulus of conventional materials such as Al, Cu, Ti decreases with increasing temperature due to the material softening [141-143]. The increase in modulus of NiTiHf with temperature can be attributed to the increase of elastic constants and anisotropy factors [144-146]. It was found that the elastic constants decrease with decreasing temperature prior to the forward martensitic transformation, mainly due to the elastic constant softening. Such a decrease of contact modulus with temperature is also observed during cooling process in Figure 4a from 320-160 °C. Therefore, 160 °C is chosen as the M_s^I, where it shows the lowest indentation modulus. With further cooling, modulus shows a sudden jump from 160-120 °C, and it saturates at about 58 GPa with further cooling. The M_f can be selected as 120 °C. As shown in Figure 6.4a, the deformation stages of contact modulus cannot be easily distinguished, but transformation temperatures can be determined and are in good agreement with the previous methods.

At higher load under 2000 mN, contact modulus is lower than the ones obtained at low load due to increased plastic deformation that impedes phase transformation. The trends of heating and cooling curves in Figure 6.4b are more overlapping with each other than Figure 6.4a and still the hysteretic behavior can be observed. Phase transformation temperatures (M_s^I, M_f^I, A_s^I, A_f^I) can be determined as the same way as under 500 mN and they are found to be 160, 140, 160, and 180 °C, respectively. It can be concluded that the indentation contact modulus is temperature dependent, but it cannot differentiate the superelastic and plastic deformation behavior accordingly under both loading levels.

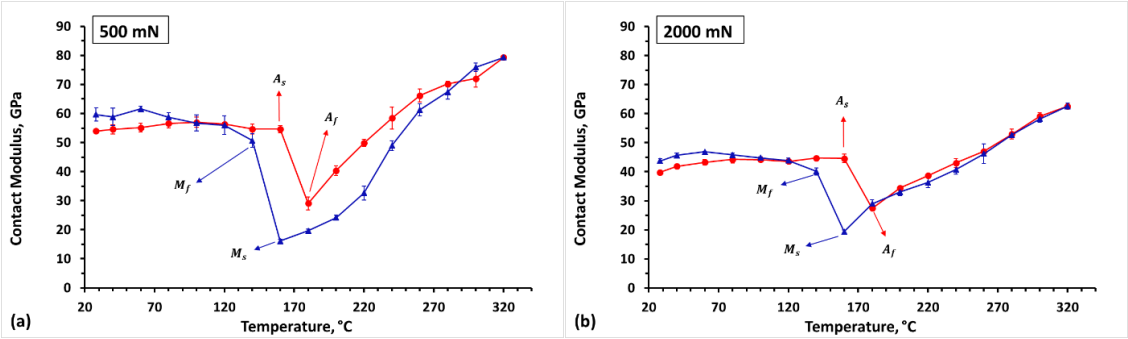

Figure 6.4: Spherical indentation response of modulus as a function of temperature for as-received NiTiHf alloy under load (a) 500 mN, (b) 2000 mN.

Table 6.2 shows the TTs obtained by using the temperature dependent work recovery ratio, hardness, and modulus results under 500 and 2000 mN, as well as the TTs obtained from DSC. It is shown that work recovery ratio method under 500 mN can be used to determine TTs, T_{SE} and M_d clearly, as well as it can distinguish deformation stages. However, the indentation hardness method cannot determine the T_{SE} accurately. Such conclusion can be understood by that work recoverable ratio depends on the elasticity, superelastic behavior, and plastic deformation during both loading and unloading paths, however, the indentation hardness response is only rely on the displacement caused by indenter at the end of loading path. Thus, due to the nature difference, same results (e.g.) are not expected from these two methods. Indentation contact modulus as a function of temperature can only characterize transformation temperatures since the measurement of modulus was made at the initial state of unloading path.

Load of 2000 mN is relatively high for the current spherical tip with a radius of 25 μm as it produces increased plasticity than the low load that impedes superelasticity. It should be noted that the stress distribution under spherical indent is not uniform. Thus, when the load is applied in superelastic region, there will be only elastic deformation regions, phase transformation regions with low plasticity and phase transformation regions

with high plasticity. Only the combined effects can be observed by the indentation experiments. The T_{SE} of NiTiHf shape memory alloys from work recovery response are stress/load dependent, where it decreases 40 °C when the load is increased from 500 mN to 2000 mN.

The hysteretic behavior is the signature of SMAs, and it has been observed in all methods. The results are similar to the thermal cycling under stress responses of SMAs where the shape memory properties are stress and plastic deformation dependent. However, thermal cycling under stress results cannot provide information about the superelastic region or the M_d. Superelasticity responses can be determined as a function of temperature to provide information about T_{SE} and M_d. However, those experiments require the testing of bulk materials and also time consuming. Indentation can provide the basic information in a reliable, faster and inexpensive manner.

Table 6.2: Shape memory properties observed from DSC, indentation work recovery, hardness, and modulus at varied load levels.

	Methods	M_s^I (°C)	M_f^I (°C)	A_s^I (°C)	A_f^I (°C)	T_{SE} (°C)	M_d (°C)
Load level	**DSC**	**160**	**134**	**167**	**186**		
500 mN	Work recovery	140	120	160	180	220	280
	Hardness	160	120	160	180	140-260	280
	Modulus	160	120	160	180		
2000 mN	Work recovery	140		160		180	
	Hardness	160	120	160	180		
	Modulus	160	120	160	180		

6.2.3. Conclusion

1. Temperature dependent of indentation work recoverable ratio, hardness, modulus were investigated between 30 and 320 °C under two load levels, and it was found that indentation response of work recovery ratio, hardness and modulus are highly temperature, and load dependent.
2. Work recoverable ratio under low load of 500 mN shows the TTs and deformation stages clearly. However, the high load of 2000 mN cannot identify detail information completely such as superelastic and plastic deformation due to the plasticity generated at higher load.
3. Temperature dependent indentation hardness or the maximum indentation depth can be used to determine the transformation temperatures but not the deformation stages.
4. High load of 2000 mN produces increased plasticity which impedes the superelastic behavior, results in a lower work recovery than low load (500 mN). Moreover, it can be conclude that higher load results in lower T_{SE}.
5. Hysteretic behavior was observed for all method on NiTiHf shape memory alloys from indentation response.

6.3. Temperature and Load Effect of NiTi-Based Shape Memory Alloys under Spherical Indenter

6.3.1. Load-Depth Curves of NiTi-based Shape Memory Alloys under Cooling

As mentioned in previous section 6.2, there are typically five stages of deformation of SMAs during cooling process: I) ($T>M_d$) plastic deformation of austenite with no recovery; II) ($T_{SE}<T< M_d$) phase transformation with plastic deformation (PD) results in partial recovery or no recovery; III) ($A_f<T<T_{SE}$) superelastic (SE) behavior with full recovery; IV) ($M_f<T<A_f$) phase transformation (PT) behavior or variant reorientation (VR) with no or partial recovery ; V) ($T<M_f$) martensite reorientation (MR), no recovery. Here, the M_d temperature is defined as the maximum temperature at which SMAs can no longer transform to martensite. The T_{SE} is defined as the temperature where the maximum superelasticity is observed. The stages above were determined by assuming that loading is only continued till the end of phase transformation. A detailed description of the deformation stages of SMAs was reported in our previous study [140]. In this chapter, only the temperature dependent indentation behavior during cooling was studied.

Figure 6.5 shows the load-displacement (L-D) curves for the spherical indentation response of Ti, NiTi, 50.8NiTi and NiTiHf alloys at selected temperatures from 340 down to 30 °C. The data obtained at other temperatures are omitted in the figure for clarity. Figure 6.5a and Figure 6.5b present the L-D curves at various indentation temperatures of the reference specimen Ti under 500 mN and 2000 mN, respectively. The maximum indentation depth (D_{max}) of Ti decreases with decreased indentation temperature for both low and high loads, which indicates that Ti softens with increasing temperature. This behavior is expected due to the conventional softening of metallic alloys with temperature.

Figure 6.5c and Figure 6.5d present the L-D curves at various indentation temperatures of NiTiHf under load 500 mN and 2000 mN, respectively. Under 500 mN, D_{max} slightly increases with decreasing the temperature from 340 °C down to 200 °C resulting a minor decrease in indentation hardness. A sudden increase in D_{max} was observed when temperature was further decreased to 140 °C. It will be shown later that the lowest hardness and modulus were observed at this temperature and thus 140 °C can be identified as M_s [140]. When the temperature is lowered to 120 °C, D_{max} decreases slightly and it continues to decrease. Under 2000 mN, the alloy shows a similar behavior as it was under 500 mN but with increased indentation depth.

Figure 6.5e shows the L-D curves of NiTi at selected temperatures under 500 mN. Its behavior is very similar to NiTiHf, where D_{max} increases incrementally as temperature decreases from 340 to 160 °C and then suddenly increases with further cooling to 90 °C. D_{max} decreases slightly and then it is constant. The behavior of D_{max} does not change considerably when the load was increased to 2000 mN. The lower D_{max} observed above 90 °C also indicates that material is stronger in austenite phase than martensite which is in good agreement with bulk measurement in NiTi alloys [100, 102, 104].

Figure 6.5g and Figure 6.5h show the L-D curves of 50.8NiTi under 500 mN and 2000 mN loads, respectively. The D_{max} increases with decreasing the temperature from 340-40 °C. Interestingly, the remnant depth, D_r, does not change with temperature except at 28 °C. This suggests that the extent of recovery increases with decreasing temperature till 40 °C. Comparing the maximum indentation depth with NiTi (Figure 6.5e), 50.8NiTi shows lower D_{max} at the same testing temperature. The same behavior is also observed

under high load of 2000 mN. Thus, we can conclude that 50.8NiTi is stronger than NiTi which is in a good agreement with the Vickers hardness result shown in Table 6.1.

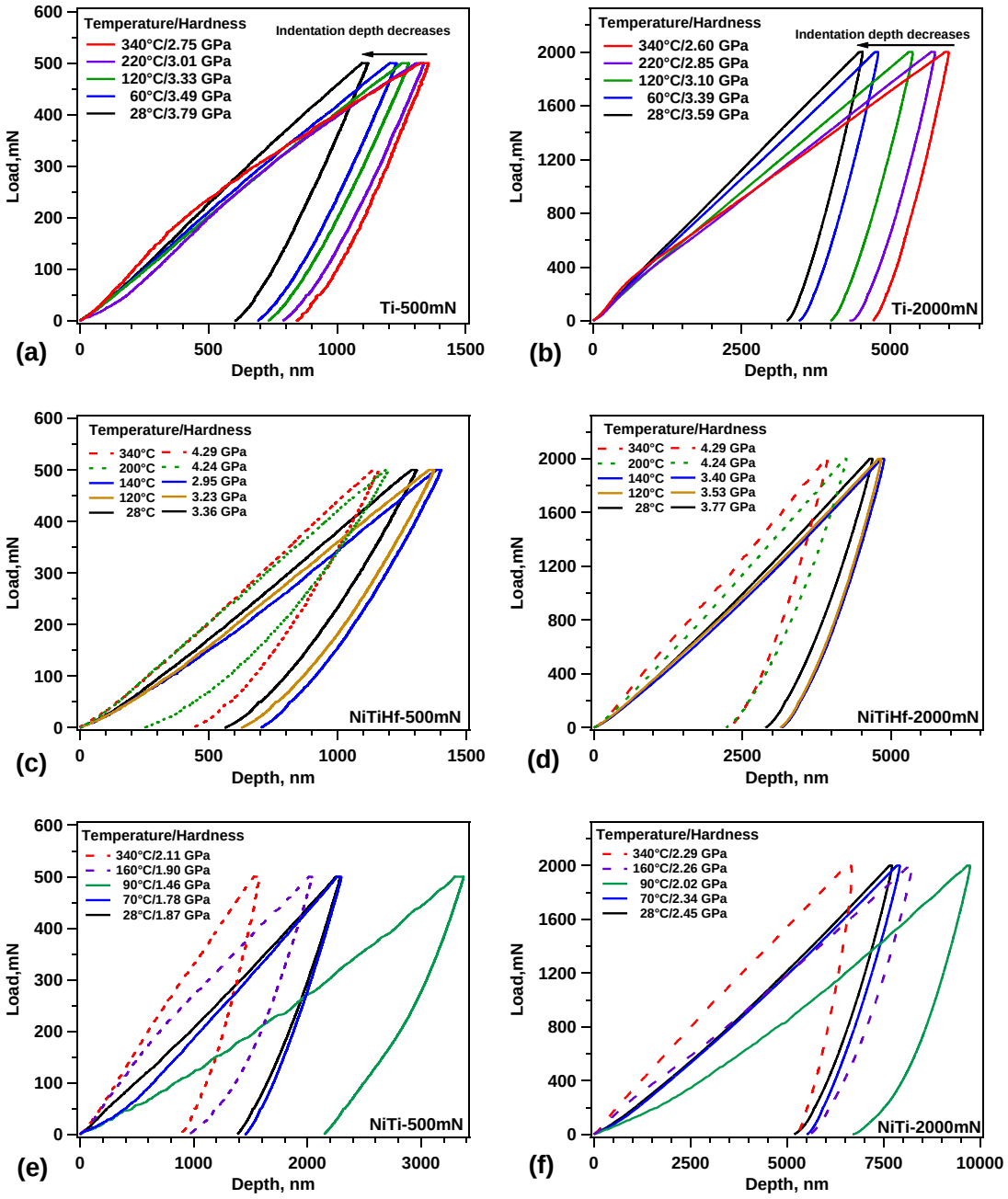

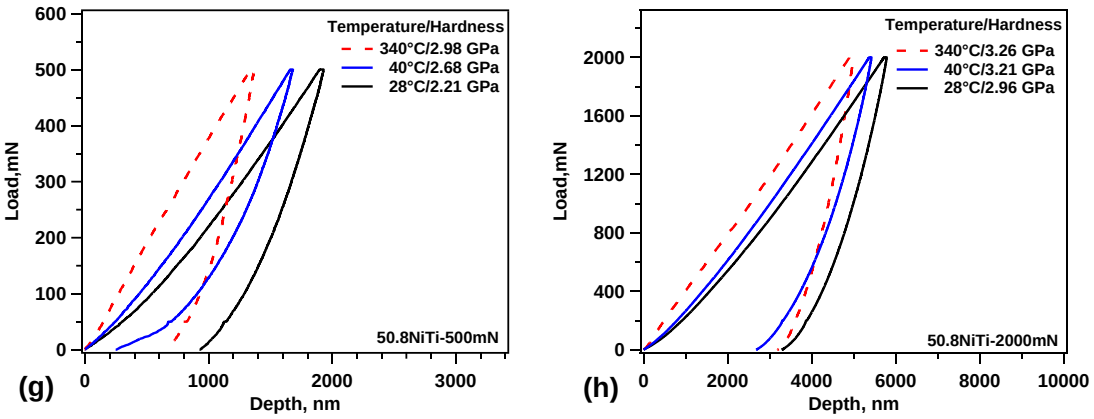

Figure 6.5: Spherical indentation responses of typical load-displacement relationships. Load-displacement curve of (a) Ti under load 500 mN and (b) Ti under load 2000 mN, (c) NiTiHf under load 500 mN, (d) NiTiHf under load 2000 mN, (e) NiTi under load 500 mN, (f) NiTi under load 2000 mN, (g) 50.8NiTi under load 500 mN, (h) 50.8NiTi under load 2000 mN as a function of temperature from 340 °C down to 28 °C.

6.3.2. Discussion

6.3.2.1. Indentation Work Recoverable Ratio

The work/depth recovery as a function of temperature is often used to characterize the superelastic behavior of SMAs [91, 101, 140]. Figure 6.6 shows the temperature and force dependent work recoverable ratio (η_w) responses of NiTiHf, NiTi, 50.8NiTi and Ti alloys. During cooling from 340 to 30 °C, the average work recoverable ratios were calculated from three repeated experiments, and then shown with the standard deviation (error bar) in Figure 6.6.

In Figure 6.6a, during cooling from 340 to 300 °C under 500 mN, the η_w is constant at about 0.55, and this region is donated as stage V where only the plastic deformation occurs. It is well known that superelastic behavior only takes place when the stress required for phase transformation is lower than the stress required for plastic deformation [147]. Thus, superelasticity cannot be observed at high temperatures above M_d. Between 300-200 °C, η_w increases and reaches to a maximum value of 0.65. 200 °C is selected as T_{SE}

where the best superelasticity can be observed [140]. The temperature range from 300 to 200 °C is denoted as the stage IV. As temperature decreases the strength of the material increases while critical stress for phase transformation decreases, resulting in better superelasticity. η_w drops of about 20 % when the temperature is decreased from 200 and 140 °C. The lowest η_w is observed at 140 °C, and it is selected as the M_s^I where SMAs show the lowest critical stress for phase transformation. The work recovery ratio decreases with temperature below A_f as only partial (above A_s) or no (below A_s) back transformation is expected. From 140-120 °C, the η_w increases sharply as the austenite to martensite transformation is expected at the sample before the start of the indentation and thus martensite reorientation would occur during loading. M_f^I is determined to be 120 °C as the η_w below that temperature is almost constant due to completed austenite to martensite phase transformation. Temperature range from 200-120 °C is selected as stage II+III. Temperature dependent behavior of η_w under 2000 mN was observed, but the stages are not as clear as they were under 500 mN. The lower η_w observed under 2000 mN can be contributed to the increased plasticity under higher stress level.

Since the martensite phase transformation temperatures of NiTi are above room temperature, temperature dependent behavior of η_w of NiTi (Figure 6.6b) is similar to the η_w of NiTiHf (Figure 6.6a). Work recoverable ratio keeps constant from 340-180 °C, and then increases slightly at 160 °C. Thus, 160 °C is selected as T_{SE}. η_w decreases from 160 to 90 °C , increases at 70 °C, and then slightly increases with further cooling. The η_w values are lower under 2000 mN then they were under 500 mN and the changes in η_w are not as distinguishable as it was under 500 mN.

50.8NiTi is austenite at room temperature which means some of the deformation stages (I, II, III) cannot be observed during cooling from 340 to 28 °C. As shown in Figure 6.6c, 50.8NiTi shows higher work recovery than the NiTi alloy at room temperature. The work recovery ratio increases slightly with decreasing temperature from 340-40 °C. There is also a notable drop of about 15 % decrease observed from 40-28 °C. Thus, T_{SE} is determined as 40 °C.

The η_w of Ti shows linear increase with decreasing temperature, as shown in Figure 6.6d. The change of η_w with temperature is due to material softening with temperature. In all cases, work recoverable ratios under 2000 mN are lower than the ones under 500 mN due to increased plastic deformation.

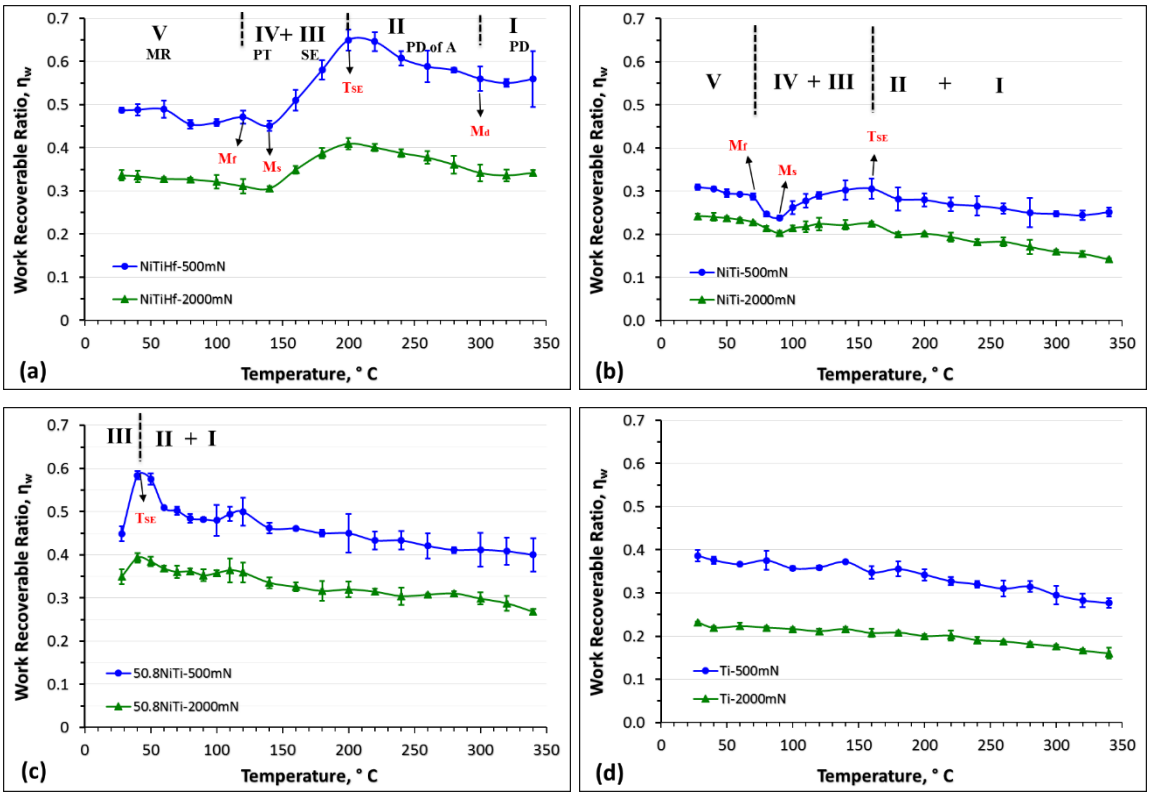

Figure 6.6: Work recoverable ratio as a function of temperature for a) NiTiHf, b) NiTi, c) 50.8NiTi, and d) Ti under load 500 mN and 2000 mN.

Based on the discussion above on the temperature dependent indentation work recoverable ratio response, four alloys in this study can be summarized and listed in Table 6.3 with temperature ranges (stage I, II+III, IV, V).

Table 6.3: Indentation temperature stages of Ti, NiTi, 50.8NiTi and NiTiHf alloys under both 500 mN and 2000 mN load. Indentation Hardness.

	Stage I (MR)	Stage II+III (PT +SE)	Stage IV (PD of Austenite)	Stage V (PD)
NiTiHf	28 °C<T< 120 °C	120 °C< T < 140 °C	140 °C< T < 200 °C	200 °C< T < 340 °C
NiTi	28 °C<T< 70 °C	70 °C< T < 90 °C	90 °C< T < 160 °C	160 °C< T < 340 °C
50.8NiTi		lower than 28°C<T<40 °C	40 °C<T< ~ °C	~ °C< T < 340 °C
Ti	NA	NA	NA	NA

6.3.2.2.Indentation Hardness

Figure 6.7 shows the spherical indentation hardness of NiTiHf, NiTi, 50.8NiTi and Ti as a function of indentation temperature that is calculated from the load-displacement curves from Figure 6.5. The average hardness was calculated from three repeating experiments, and then shown with the error bar representing the standard deviation. Indentation hardness of NiTiHf alloy as a function of temperature was divided into five stages. Comparing with other three alloys, the indentation hardness of NiTiHf under 500 mN shows significant changes during cooling process under 500 mN.

In Figure 6.7a, from 340-260 °C under 500 mN, the average indentation hardness is constant at 4.3 GPa. However, it should be noted that the error bars indicate a relatively large variation at those temperatures. This behavior can be attributed to the fact that shape memory behavior and plastic deformation are orientation dependent [140]. In detail, the indentation response at three different locations results in different L-D results as some of

them might show superelasticity while others could be plastically deformed. From 260 to 220 °C, the hardness increases and reaches to its highest value at 220 °C. Indentation hardness drops of about 1.8 GPa when the temperature is decreased from 220 °C to 140 °C under 500 mN. The decrease in indentation hardness was 1 GPa under 2000 mN for the same temperature range. The large decrease of hardness is due to increased volume of the phase transformation from austenite to martensite during loading. From 140 °C to 120 °C, hardness increases slightly due to the completion of martensite transformation of the sample before testing. Below 120 °C, indentation hardness increases indistinctively with decreasing the temperature and saturate at 3.5 GPa. Under 500 mN, the indentation hardness response trend with temperature is almost identical to the work recoverable ratio results shown in Figure 6.6a. Under 2000 mN, the hardness response has a similar tendency with the low load (500 mN), but it does not clearly show the deformation stages

Figure 6.7b shows the hardness response of NiTi, where the stages cannot be separated as clear as the work recoverable ratio response shown in Figure 6.6b. The indentation hardness behavior did not change with load level. Figure 4c shows the hardness of 50.8NiTi alloy as function of temperature, and it is almost constant till 40 °C. From 40 to 28 °C, hardness decreases dramatically due to the austenite to martensite transformation of the sample. Indentation hardness of NiTiHf is the highest among the three SMAs investigated in this study, and 50.8NiTi shows a higher indentation hardness than NiTi. These results are in good agreement with the Vickers hardness results provided in Table 1. In Figure 6.7d, the indentation hardness of Ti increases with decreasing temperature. Its hardness is slightly lower under 2000 mN.

In Figure 6.7, indentation hardness of four alloys as a function of temperature under 2000 mN behaves in a similar manner as the ones under 500 mN, but stages cannot be separated at higher load level due increased plasticity. Indentation hardness of NiTi-based alloys is slightly higher under 2000 mN which is in good agreement with the previous spherical indentation studies of NiTi-based alloys [110]. It is worth to note that the indentation hardness is calculated at a single point while the work recoverable ratio is calculated from the whole loading/unloading curves. Thus, in order to characterize the shape memory properties accurately, the work recoverable ratio method is more appropriate to use than the indentation hardness response.

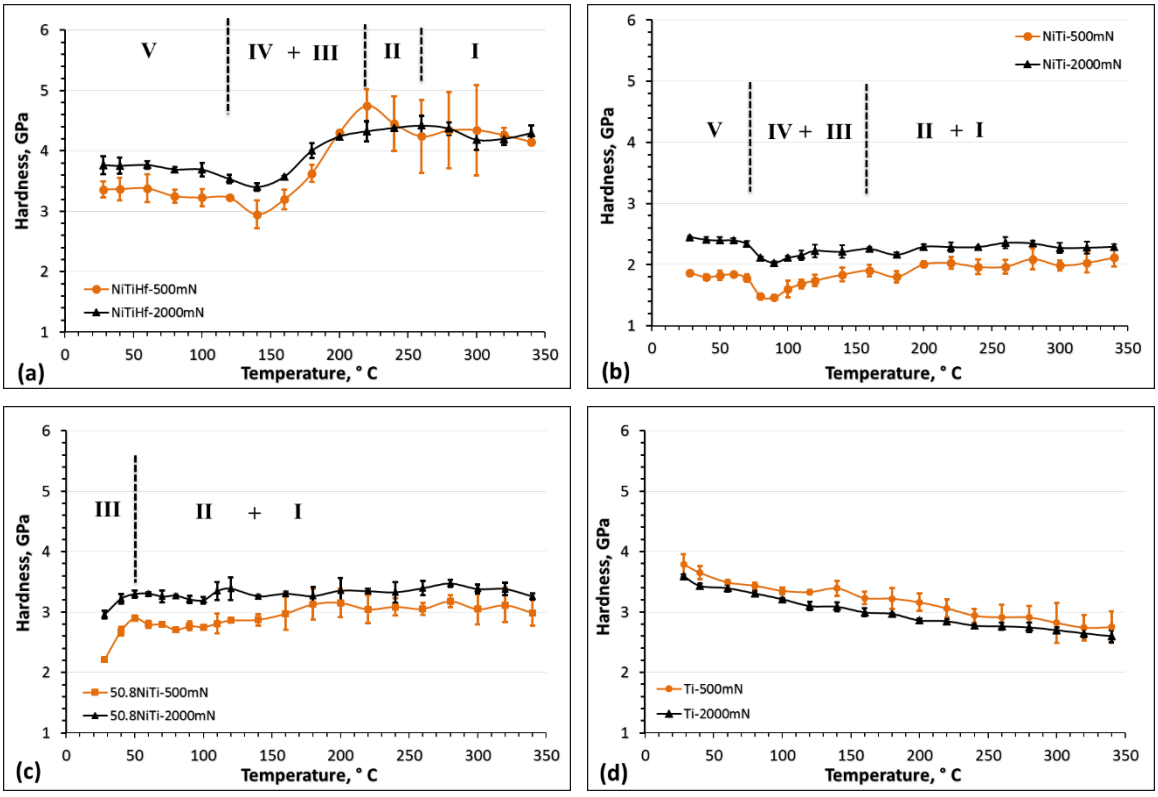

Figure 6.7: Spherical indentation hardness as a function of elevated temperatures for a) NiTiHf, b) NiTi, c) 50.8NiTi, and d) Ti under load 500 mN and 2000 mN.

6.3.2.3. Indentation Modulus

Figure 6.8 shows the contact modulus of NiTiHf, NiTi, 50.8NiTi and Ti alloys as a function of temperature under 500 and 2000 mN.

At low load 500 mN, Ti has a Young's modulus of 95 GPa at room temperature, which is in good agreement with the Young's modulus (100 to 130 GPa) measured by mechanical testing [148-151]. In Figure 6.8, indentation contact modulus of Ti under both 500 and 2000 mN, initially decreases as decreasing temperature till to 240 °C, and then slightly increases with further cooling. It should be noted that Young's modulus of Ti-6Al-4V depends on the heat treatments that affect the volume fraction of existing phases [149]. For indentation experiments with elevated temperature, it takes almost two hours to make measurements at each indentation temperature. Thus, the contact modulus of Ti might be affected by the unintentional heat treatment during the indentation experiment. It should also be noted that the modulus of conventional materials such as Al, Cu, Ti decreases with increasing temperature due to the material softening [141-143]. On the contrary, the moduli of three SMAs decrease with decreasing temperature. Such temperature dependence of the elastic constants and anisotropy factors were previously reported in NiTi-based alloys [144-146], where elastic constants decreases prior to the forward martensitic transformation, mainly due to the softening. The contact moduli of all the alloys are greater under 500 mN than 2000 mN. In NiTi and NiTiHf, the lowest moduli are observed at 90 and 160 °C and they can be selected as the M_S^I, respectively. Since 50.8NiTi is austenite at room temperature, the contact modulus decreases linearly during cooling, and modulus drops at around 40 °C.

At room temperature, it is instructive to note that the modulus of martensitic NiTiHf is higher than the moduli of NiTi alloys under both load levels shown in Figure 6.8. However, modulus at 340 °C shows no difference between NiTi and NiTiHf alloys.

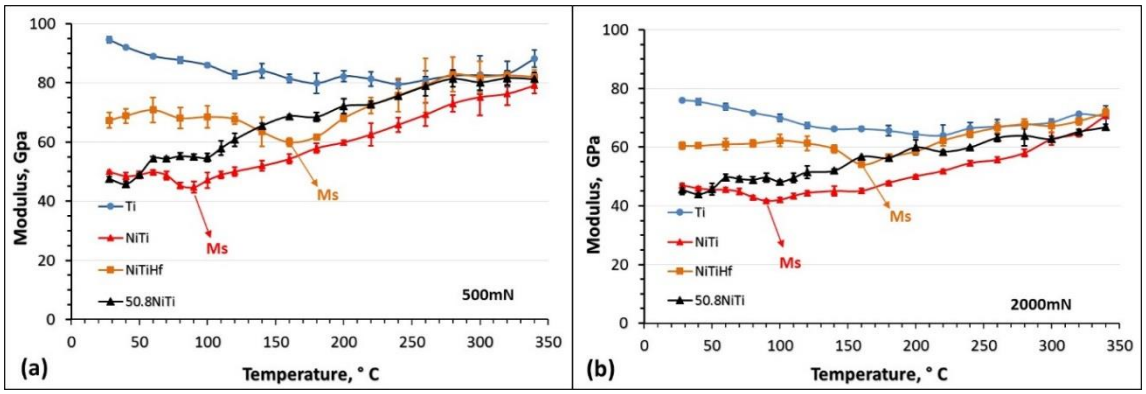

Figure 6.8: Spherical indentation modulus as a function of temperature for NiTiHf, NiTi, 50.8NiTi, and Ti under load (a) 500 mN and (b) 2000 mN.

Table 6.4 lists shape memory properties such as TTs, T_{SE}, and M_d observed from temperature dependent indentation response under two load levels for NiTi and NiTiHf alloys, using work recovery, hardness, and modulus methods. Ti alloys is not included in Table 3 because it does not show TTs between 30-340 °C.

As shown in Table 6.4, it can be concluded as follow: 1) shape memory properties of superelastic NiTi alloys cannot be characterized from temperature dependent indentation response under both load levels due to the low TTs; 2) indentation modulus method can only determine the martensite start and finish temperatures, results agree well with other methods; 3) due to the weak mechanical behavior of NiTi alloy, shape memory properties cannot be characterized as complete as high temperature/strength NiTiHf through indentation response; 4) Indentation work recovery and hardness response of NiTiHf can provide clearly relations with temperatures. Moreover, deformation stages and shape

memory properties can be determined accordingly under low load; 5) due to the nature difference of indentation hardness and work recovery measurements, same characterization results from these two methods are not expected; 6) T_{SE} of NiTiHf alloys are highly load dependent, but such load dependent behavior did not show on NiTi alloy. Since NiTiHf in this study shows better indentation response (work recovery, hardness, and modulus) than other NiTi alloys, thus, it can be suggested that NiTiHf is an ideal material for mechanical characterization through high temperature indentation techniques.

Table 6.4: Shape memory properties such as TTs, T_{SE}, and M_d observed from temperature dependent indentation response under two load levels were listed for NiTi, NiTiHf alloys.

SMAs	**Method**	**500 mN**				**2000 mN**			
		M_s^I **(°C)**	M_f^I **(°C)**	$\mathbf{T_{SE}}$ **(°C)**	$\mathbf{M_d}$ **(°C)**	M_s^I **(°C)**	M_f^I **(°C)**	$\mathbf{T_{SE}}$ **(°C)**	$\mathbf{M_d}$ **(°C)**
NiTi	Work recovery	90	70	160	N	90	N	160	N
	Hardness	90	60	N	N	90	60	N	N
	Modulus	90	N	N	N	N	N	N	N
50.8NiTi	Work recovery	N	N	40	N	N	N	40	N
	Hardness	N	N	N	N	N	N	N	N
	Modulus	40	N	N	N	N	N	N	N
NiTiHf	Work recovery	140	120	200	300	140	N	200	300
	Hardness	140	120	220	300	140	100	260	300
	Modulus	160	N	N	N	N	N	N	N

6.3.3. Conclusion

Spherical indentation response (work recoverable ratio, hardness, and contact modulus) of Ti, NiTi, 50.8NiTi, and NiTiHf were investigated with a cooling process from high temperature 340 to 28 °C with an interval of 20 °C/each under 500 mN and 2000 mN. It has been concluded that

1. Phase transformation temperatures (M_s, M_f), T_{SE}, and M_d of non-superelastic NiTi and NiTiHf alloys were observed from spherical indentation during cooling process using the work recovery method under 500 mN. However, due to the weak mechanical behavior of NiTi alloy, its indentation characterizations with temperature are not as clear as high temperature/strength NiTiHf alloy.
2. Indentation contact modulus of SMAs decrease with decreasing temperature prior to the forward martensitic transformation due to softening of elastic constant, while inversely result was observed in Ti alloy. This method can be only used for determine the martensite start and finish temperatures.
3. Shape memory properties of superelasticity 50.8NiTi alloy cannot be characterized through indentation responses since the transformation temperatures are lower than room temperature.
4. Indentation response of SMAs is temperature dependent, and it is revealed that TTs, T_{SE}, and M_d are load dependent, but lower load shows more prominent and accurate results than the high load.

7 ORIENTATION DEPENDENT INDENTATION RESPONSE OF NITI-BASED SMAS

7.1. Introduction

It should be noted that these previous single crystal studies were conducted at room temperature. Therefore, no attempt was made to systematically investigate the effects of temperature on their response through indentation techniques, and it remains unclear whether their indentation response is orientation dependent.

In this chapter, $Ni_{50.3}Ti_{29.7}Hf_{20}$ alloys aged at 650 °C for 3h were selected to conduct high temperature indentation along the [100], [110] and [111] orientations since their mechanical responses were revealed before [50]. The main aims of this study on the single crystal $Ni_{50.3}Ti_{29.7}Hf_{20}$ alloys are to investigate the effect of orientation and temperature on their indentation responses and shape memory properties by analyzing the indentation work recovery and hardness results, and then correlate these results with the results obtained from macro compression tests.

7.2. Load-Depth Curves of Single Crystal NiTiHf SMAs

Figure 7.1a and Figure 7.1b show the load-displacement (L-D) curves during heating and cooling for the spherical indentation of the NiTiHf alloys under the load of 500 mN at selected temperatures between 30 and 340 °C along the [111] orientation, respectively.

During heating from 40 to 130 °C, the L-D curves are almost identical to each other as the main deformation mechanism was martensite reorientation. The maximum

indentation depth (D_{max}) increases profoundly with temperature from 130 to 145 °C where the maximum D_{max} was observed at 145 °C. The increase in D_{max} can be attributed to the fact that the alloy transforms from martensite to austenite with increased temperature. Above 145 °C, D_{max} decreased dramatically with temperature till 340 °C, resulting in increased in hardness. When the temperature was increased from 145 °C to 195 °C, both D_{max} and the recoverable depth (D_r) decreased of about 300 nm, suggesting the increased work/depth recovery due to superelasticity since austenite phase was formed completely. Moreover, at 195 °C, the highest work/depth recovery ratio was observed.

During cooling (Figure 7.1b), at 340 °C, the sample was austenite initially and deformed plastically because the temperature was high and above M_d. D_{max} increased slightly as temperature decreased from 340 to 195 °C. With further cooling from 195 to 115 °C, large increase in D_{max} (about 300 nm) and D_r (about 500 nm) were observed while the hardness dropped profoundly from 4.74 to 3.02 GPa. The maximum D_{max} was occurred at 115 °C which corresponds to the lowest hardness during cooling and in good agreement with the M_s (123 °C) determined from DSC. It is instructive to note that the highest work recoverable ratio was again observed at temperature 195 °C. When the temperature decreased from 115 to 40 °C, both the D_{max} and D_r decreased slightly. Pop-in behavior was not observed in $Ni_{50.3}Ti_{29.7}Hf_{20}$ single crystals.

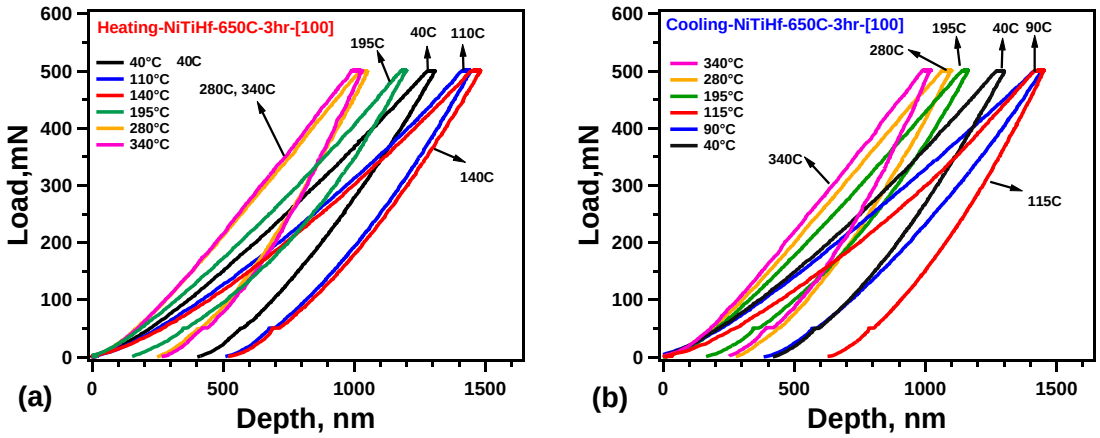

Figure 7.1: Spherical indentation response of typical load-depth relationships at selected temperatures between 30 and 340 °C under 500 mN. The L-D curves of [100]-oriented NiTiHf 650 °C-3h are shown in (a) heating and (b) cooling process.

7.3.Discussion

7.3.1. Indentation Work Recovery

Figure 7.2a and Figure 7.2b are the temperature dependent work recovery ratio (η_w) and maximum indentation depth (D_{max}) of [111]-oriented NiTiHf single crystal under 500 mN, respectively.

In Figure 7.2a, the η_w is constant at about 0.63 from 30 to 130 °C, and then it sharply decreases to the lowest value of 0.61 at 145 °C during heating. Such phenomenon of sharp decrease was not observed in previously reported polycrystalline NiTiHf alloys [140]. From 145-150 °C, the η_w dramatically increases from 0.61 to 0.67. With further heating to 190 °C, the η_w continues to increase and reaches to its highest value of 0.74. Above 190 °C, the η_w gradually decreases with temperature, and saturates at about 320 °C. During cooling from 340 to 150 °C, the η_w is almost identical to the η_w obtained during heating as the sample is completely austenite in both cases. The η_w decreases slightly from

150 to 125 °C, and then sharply decreases to 0.54 (the lowest) at 115 °C. With further cooling to 105 °C, the η_w increases quickly and reaches to 0.63. Below 105 °C, the η_w keeps constant at 0.63 as the heating experiments.

The corresponding temperature dependent maximum indentation depth during heating and cooling were shown in Figure 7.2b. It should be noted that the indentation hardness is inversely proportional to the maximum indentation depth, where the lowest hardness occurs at the highest D_{max}, and vice versa. Moreover, the measurement of work recoverable ratio depends on the elasticity, superelastic behavior, and plastic deformation during both loading and unloading paths, however, the measurement of D_{max} only relies on the displacement movement of indenter at the end of loading. In Figure 7.2b, the D_{max} increases till 145 °C, and then decreases with temperature. The highest D_{max} is observed at 145 °C. The sharp increase and then decrease of D_{max} are observed from 130 to 145 °C and from 145 to 155 °C, respectively. Following the heating, the D_{max} of cooling process follows the identical path from 340 to 160 °C. With further cooling, the highest D_{max} is obtained at 115 °C and the D_{max} sharply decreases from 115 to 85 °C. Below 85 °C, the D_{max} is constant with temperature. It should be noted that during cooling, there are also two sudden changes of D_{max} where it increases sharply from 130 to 115 °C, and decreases dramatically from 115 to 85 °C. Such dramatic behavior change of D_{max} with temperature can be correlated with the work recovery ratio in Figure 7.2a.

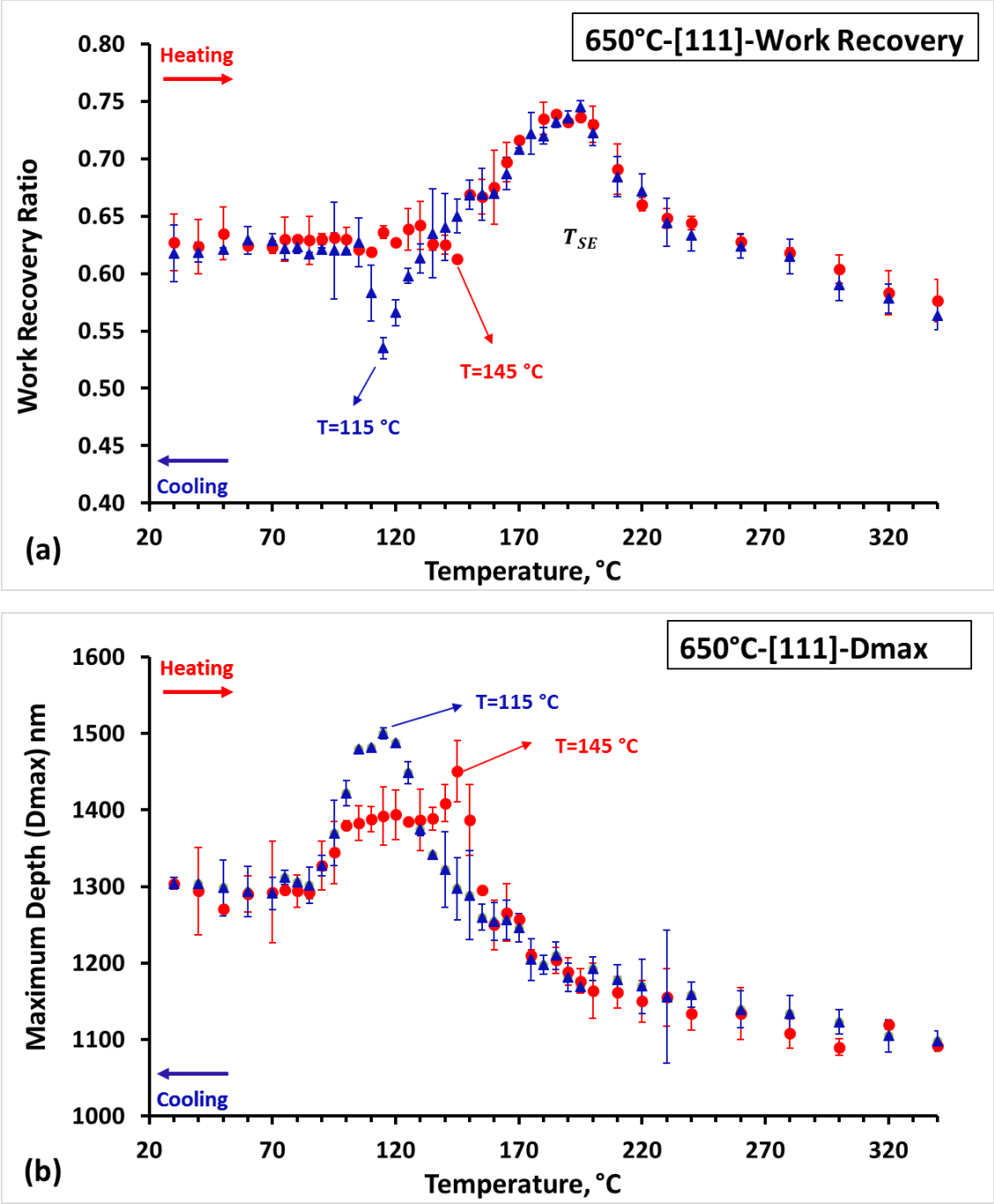

Figure 7.2: Spherical indentation response of work recoverable ratio (a) and the corresponding maximum depth (b) as a function of temperature under 500 mN of single crystal NiTiHf aged at 650 °C-3h with heating process from 30 to 340 °C marked as circle and cooling process from 340 to 30 °C marked as triangle in [111] orientations.

7.3.2. Deformation Behavior in Schematics

A typical SMA exhibits phase transformation from austenite to martensite phases or martensite reorientation, depending on the applied stress and temperature. It has been known that the critical stress (σ_c) for variant reorientation decreases with temperature below A_s, and σ_c for phase transformation increases with temperature between $A_s<T<M_d$. σ_c for plastic deformation decreases at temperatures above M_d. For detail phase deformation behavior of conventional compressive response, please refer to our previous study [140].

The temperature dependent indentation work recovery of single crystal is found to be different than the behavior of polycrystalline NiTiHf alloys [140]. The deformation stages can be observed more clearly in the single crystalline response which can be attributed to the fact that shape memory and deformation mechanisms of SMAs are orientation dependent. In polycrystalline alloys, the small scale indentation response could vary with the orientation of the grains affected. . In order to relate the indentation response and compressive response, a simplified schematic is presented in Figure 7.3 to show the 5 deformation stages of SMAs. Transformation temperatures, T_{SE} and M_d are displayed in Figure 7.3 based on the understanding from polycrystalline NiTiHf [140] and the temperature dependent stress-strain behavior under uniaxial compressive load. In detail, the temperature, where shows the highest D_{max} during heating and cooling, corresponds to A_f^I and M_s^I, respectively, while the temperature at the lowest work recoverable ratio during heating and cooling corresponds to A_s^I and M_s^I, respectively. Moreover, the temperature with the highest work recoverable ratio is the T_{SE}, and M_d can be determined at the temperature where the work recoverable ratio starts to saturate after $T_{SE.}$

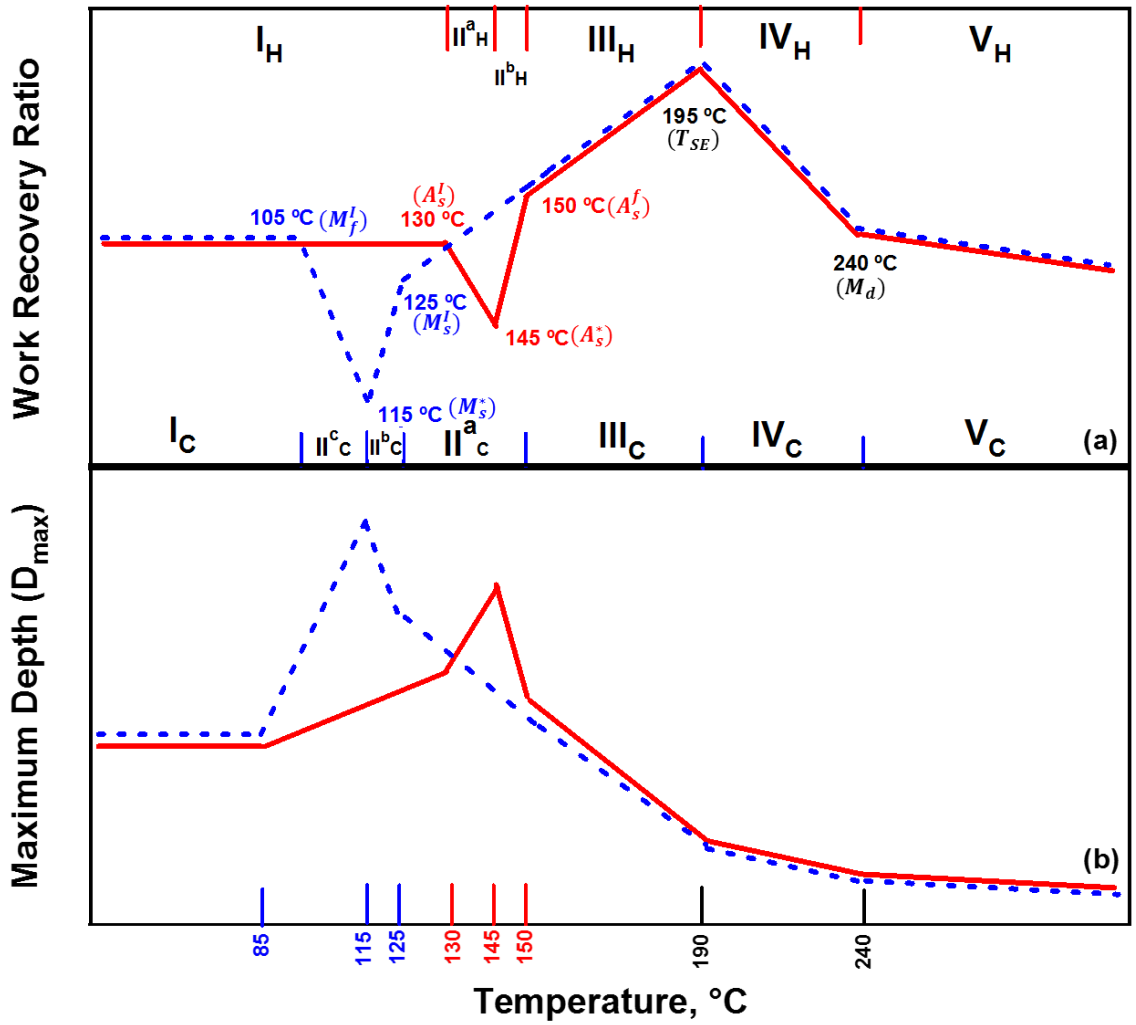

Figure 7.3: The schematic drawing of (a) work recovery, and (b) maximum indentation depth as a function of temperature during heating (solid lines) and cooling (dotted lines).

7.3.3. Deformation Behavior during Heating

In the following sections, only boundary temperatures at each stage will be used for discussion. For example, deformation behavior or indentation responses at only boundary temperatures (e.g. 30 and 130 °C) during stage I_H will be analyzed.

(1) Stage I_H -T< A_s^I (30-130 °C)

Figure 7.4 shows the stress-strain curves at different temperature range in a schematic way from compression test, and the maximum indentation depth is also displayed in the figure. During heating from 30 to 130 °C, η_w is constant while D_{max} increases with temperature. Starting with room temperature where the alloy is martensite, martensite variant reorientation (VR) takes place during indentation under the peak load of 500 mN. As shown in Figure 7.4, the conventional compressive stress-strain relation of a SMA shows that the stress for variant reorientation (σ_c^{VR}) decreases with temperature when $T<A_s$. Thus, under a constant peak load during indentation, as the temperature increased, the deformation behavior under indentation becomes easier, which results in larger D_{max} with temperature. Hence, the austenite start temperature obtained from indentation (A_s^I) can be selected as 130 °C.

(2) Stage II_H^a - $A_s^I < T < A_s^*$ (130-145 °C)

The stage II shows phase transformation behavior and includes two parts (II_H^a and II_H^b), and they will be discussed separately. From 130 to 145 °C, the η_w decreases to its lowest value and D_{max} increases to its highest value. Figure 7.4b shows the temperature dependent stress-strain relation in compression test when martensite starts to transform to austenite. From A_s to A_f, the volume fraction of martensite will decrease and the volume fraction of austenite will increase. When these two phases exist together, both the VR of martensite and stress induced transformation from austenite to martensite can be observed. It should also be noted that σ_c^{VR} decreases while σ_c^{SIM} increases with temperature. At temperatures close to A_s (e.g. 130 °C) the volume fraction of martensite is high so it dominates the response. As temperature is increased, the volume fraction of austenite increases and eventually it becomes more dominant. After austenite transforms to

martensite during loading, the back transformation does not take place when the temperature is below A_f. The lack of martensite to austenite back transformation, results in a sudden drop of η_w when temperature is decreased to 145 °C. During stage II_H^a with a mix phase M+A (M is dominant), the stress-induced martensitic phase transformation, σ_c^{SIM}, is lower than σ_c^{VR}. Thus, for the constant applied load a larger austenite region will transform to martensite at 145 °C, resulting in higher D_{max}. The indentation depth of these two temperatures were also presented in Figure 7.4b. As shown in Figure 7.3, the lowest η_w was obtained at 145 °C during heating. Hence, 145 °C is selected as A_s^*, the temperature which is expected to be between A_s and A_f.

(3) Stage II_H^b - $A_s^* < T < A_f^I$ (145-150 °C)

From 145 to 150 °C, a dramatic increase of η_w was observed in Figure 7.3, manifesting the completion of martensite to austenite phase transformation at 150 °C. Such an increase in the work recovery ratio is due to the increased volume fraction of austenite phase in the matrix that undergoes SIM upon loading. In stage II_H^b, austenite phase becomes dominant when the temperature is close to 150 °C. Moreover, as shown in Figure 7.4c, σ_c^{SIM} becomes greater than σ_c^{VR}. The D_{max} drops abruptly from 1451 to 1295 μm in this temperature range while η_w increases. This observation can be attributed to the high σ_c^{SIM}. Since the applied force is kept constant during indentation, and higher σ_c^{SIM} at 150 °C results in a lower volume of transformation and lower D_{max}. The work recovery continues to increases above 150 °C, thus A_f^I=150 °C, which is lower than the A_f = 175 °C from DSC.

(4) Stage III_H - $A_f^I < T < T_{SE}$ (150-195 °C)

Above A_f^I, the η_w keeps increase till 195 °C and the D_{max} decreases with temperature in stage III_H. The highest work recovery ratio indicates the best superelastic behavior upon unloading at 195 °C (T_{SE}). Thus, the range 150-195 °C was defined as the superelastic region. Figure 7.4d shows the temperature dependent stress-strain behavior in compression test, where the σ_c^{SIM} increases with temperature. Thus, the decrease of D_{max} with temperature can be attributed to the higher critical stress for phase transformation at higher temperature of 195 °C.

(5) Stage IV_H - T_{SE} <T< M_d (195-240 °C)

During this temperature range, both the η_w and D_{max} decrease with temperature. Such a decrease of the η_w is attributed to the increased plastic deformation of austenite phase with partial superelasticity, and it also indicates phase transformation. Figure 7.4e shows that the critical stress for phase transformation and plastic deformation of austenite increase with temperature, which also indicates that indentation deformation is getting difficult at higher temperature, resulting in decrease of D_{max}.

(6) Stage V_H- T > M_d (240-340 °C)

Above 240 °C, with only plastic deformation during indentation, the work recovery ratio and D_{max} are almost constant with temperature. M_d was selected as 240 °C since phase transformation behavior is not expected to be observed at higher temperatures. As shown in Figure 7.4f, the stress for plasticity slightly decreases with temperature due to the material softening. However, the change is not so obvious which results the constant D_{max} during indentation with temperature.

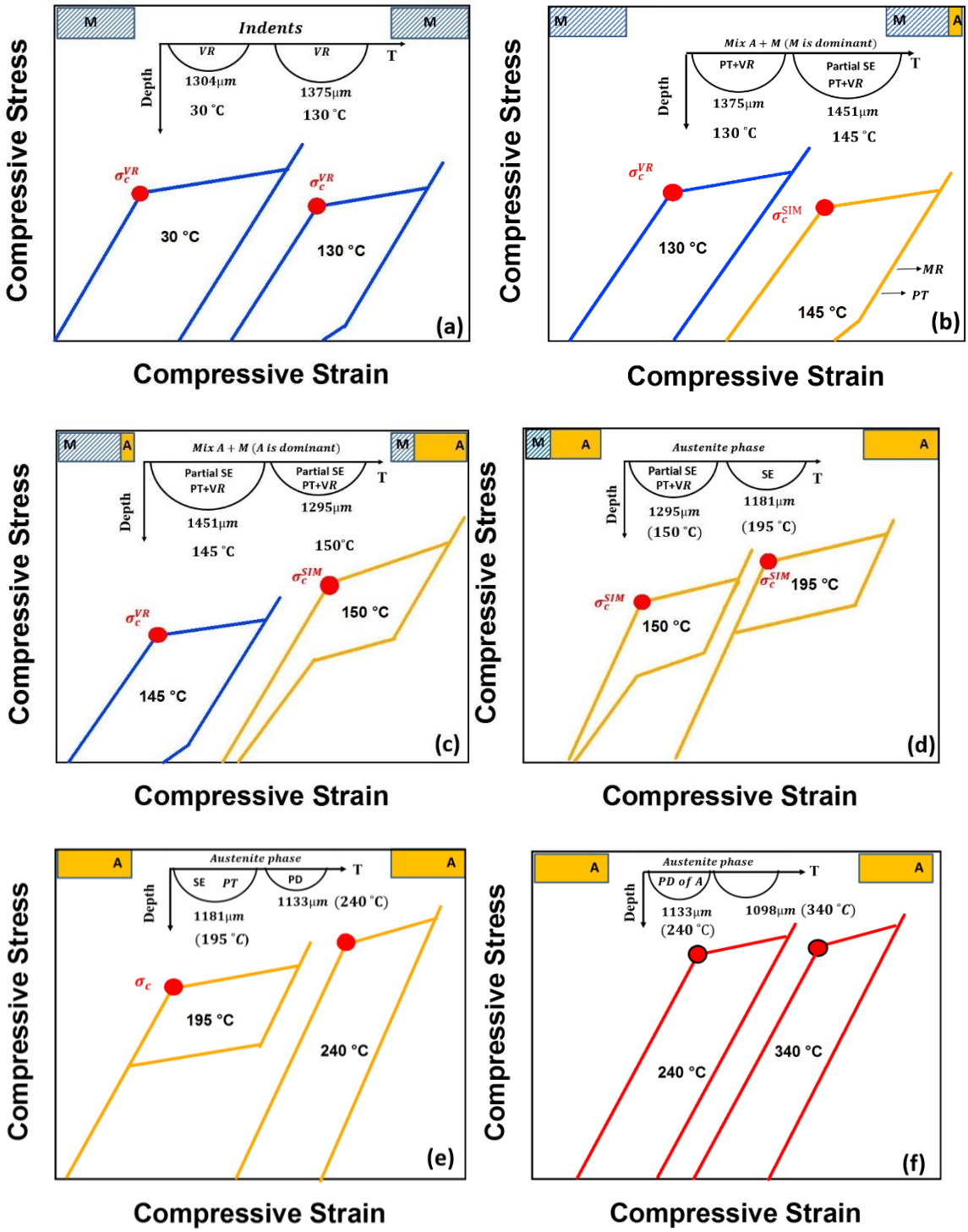

Figure 7.4: Temperature dependent compressive stress-strain relation of a typical SMA during heating process in (a) stage I_H (T< A_s^I), (b) Stage II_H^a (A_s^I< T< A_s^*), (c) Stage II_H^b

(A_s^*< T< A_f^I), (d) Stage III_H (A_f^I<T<T_{SE}), (e) Stage IV_H (T_{SE}<T<M_d), and (f) Stage V_H (T > M_d). The correspondent D_{max} is also presented at each temperature.

7.3.4. Deformation Behavior during Cooling

Following the heating experiments, the work recovery ratio as a function of temperature with cooling process was also divided into five stages as shown in Figure 7.3 with dotted lines. During cooling from 340 to 150 °C, the indentation work recovery ratio and the maximum indentation depth have the same values as the ones obtained from the heating experiments. This is expected as sample is completely austenite in this temperature region. Since work recovery ratio is almost identical, this behavior indicates the deformation of austenite has a good agreement of heating and cooling experiments. Therefore, the stage III, V, and IV of cooling process are in the same temperature range as with the heating process, and the deformation behavior under indenter can be explained in the same way. Moreover, the stage I_C also overlapped within the stage I_H since sample is in pure martensite phase. With further cooling, the phase transformation stage II was divided into three sections as II_C^a, II_C^b, II_C^c, and they will be discussed in detail as following.

(1) Stage $\boldsymbol{II_C^a}$ **(150-125 °C)**

As the sample is cooled, the indented area will be initially in austenite phase as long as the temperature is above M_s. Thus this stage is the continuation of the previous stage where η_w decreases but the D_{max} increases due to decreased σ_c^{SIM} shown in Figure 5a.

(2) Stage $\boldsymbol{II_C^b}$ **-$\boldsymbol{M_s^*}$<$\boldsymbol{T}$<$\boldsymbol{M_s^I}$ (115-125 °C)**

During this temperature stage, the η_w decreases dramatically to the lowest value while the D_{max} increases to the highest point at 115 °C. At 125 °C, austenite phase starts to transform to martensite, thus it was selected as M_S^I. The temperature at where it shows the lowest work recovery ratio was selected as the M_S^* (It is expected to be between the M_s and M_f from DSC). It is well known that the lowest σ_c^{SIM} is observed at M_s. Between 125 and 115 °C, although martensite starts to transform, austenite is still the dominant phase with higher volume fraction, The schematic shown in Figure 5b and 5c are the stress-strain curves at 125 and 115 °C, respectively. It should be noted that the σ_c^{SIM} is lower than the σ_c^{VR} at this mix phase (*A*+*M*) stage. At 125 °C the combined effects of σ_c^{SIM} and σ_c^{VR} will be presented by the $\sigma_c^{VR+SIM} = v_f^M \sigma_c^{VR} + v_f^A \sigma_c^{SIM}$. When the temperature is decreased to 115 °C, volume fraction of austenite and σ_c^{SIM} decreases as well. As shown in Figure 5c, at 115 °C, the σ_c^{VR} is almost constant, while σ_c^{SIM} decreases profoundly. Thus, σ_c^{VR+SIM} at 115 °C is decreased resulting in higher D_{max}.

(3) Stage $\boldsymbol{II_C^c}$**-** $\boldsymbol{M_f^I < T < M_S^*}$ **(105-115 °C)**

From 115 to 105 °C, the η_w increases sharply and the D_{max} decreases pronouncedly. The indentation martensite finish temperature M_f^I was chosen at 105 °C since work recovery ratio stays constant with further cooling. Below 115 °C, martensite phase becomes dominant. From Figure 7.3a, it can be concluded that the work recovery ratio of austenite is lower than the martensite phase in this region. Therefore, the increase of η_w is attributed to higher volume fraction of martensite. Figure 7.5d shows the stress-strain relation at these two temperature boundaries. Since the $\sigma_c^{VR} > \sigma_c^{SIM}$ during this temperature range, the indentation deformation becomes difficult as temperature gets close

to the M_f^I where only the variant reorientation exists. Therefore, the D_{max} is increased at 105 °C.

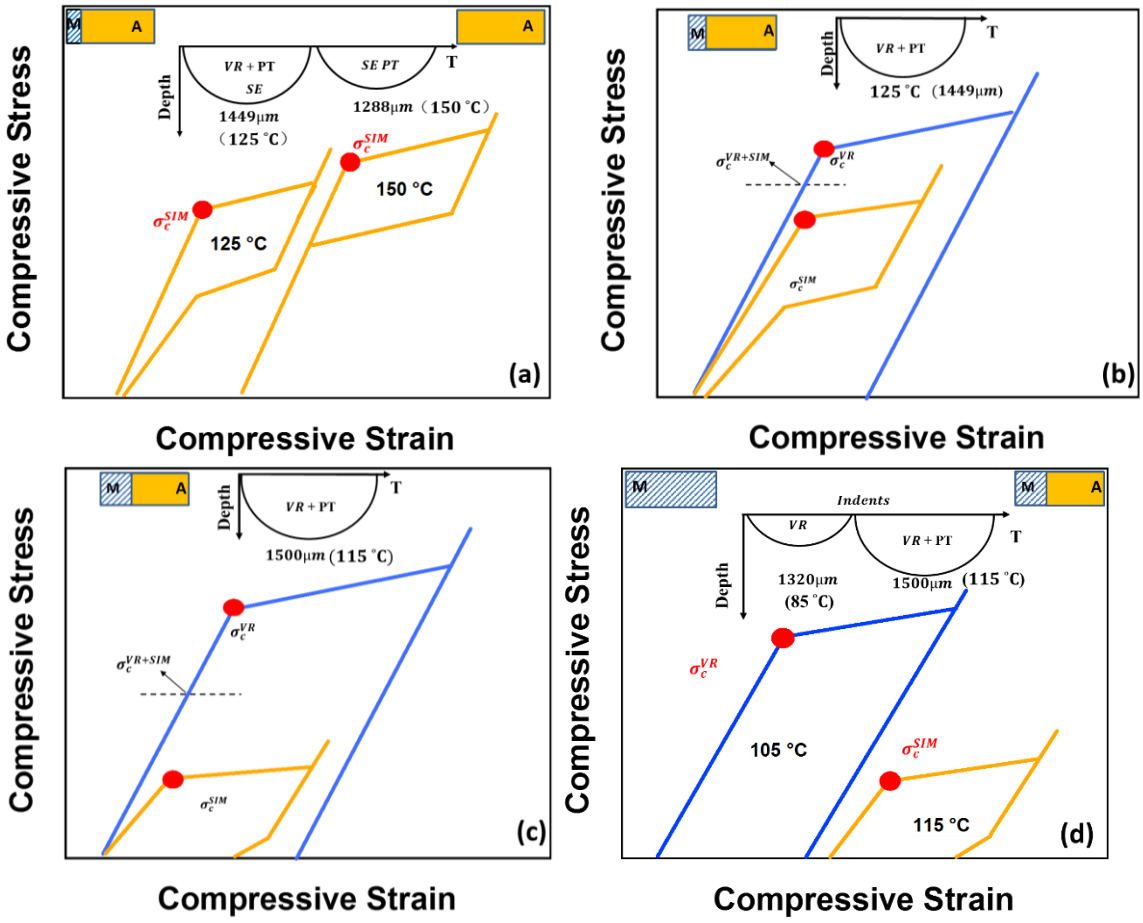

Figure 7.5: Temperature dependent compressive stress-strain relation of a typical SMA during cooling process at (a) Stage II_C^a ($M_s^I < T < A_f^I$), (b) temperature 125 °C (M_s^I), (c) temperature 115 °C (M_s^*), (d) Stage II_C^c ($M_f^I < T < M_s^*$). The correspondent D_{max} is also presented at each temperature.

7.3.5. Work Recovery Analysis in [100] and [110]

Figure 7.6a and Figure 7.6b show the temperature dependent work recovery ratios in [100] and [110] orientations, respectively. Comparing with [111] (shown in Figure 7.2a), it can be concluded that work recoverable ratio is almost orientation independent in NiTiHf

alloys. The work recovery ratio at martensite phase is 0.63 for all three orientations. Along the [100] orientation, it is difficult to determine the A_s^I and A_s^* during heating, but T_{SE} (195 °C) is same as the one observed in [111]. The cooling curve of [100] behaves the same way as [111]. The work recovery curves of [110] are very similar with [111], and the lowest η_w is observed at 135 °C and 95 °C during heating and cooling process, respectively. However, the T_{SE} is 175 °C from [110] which is 20 degrees lower than other two orientations.

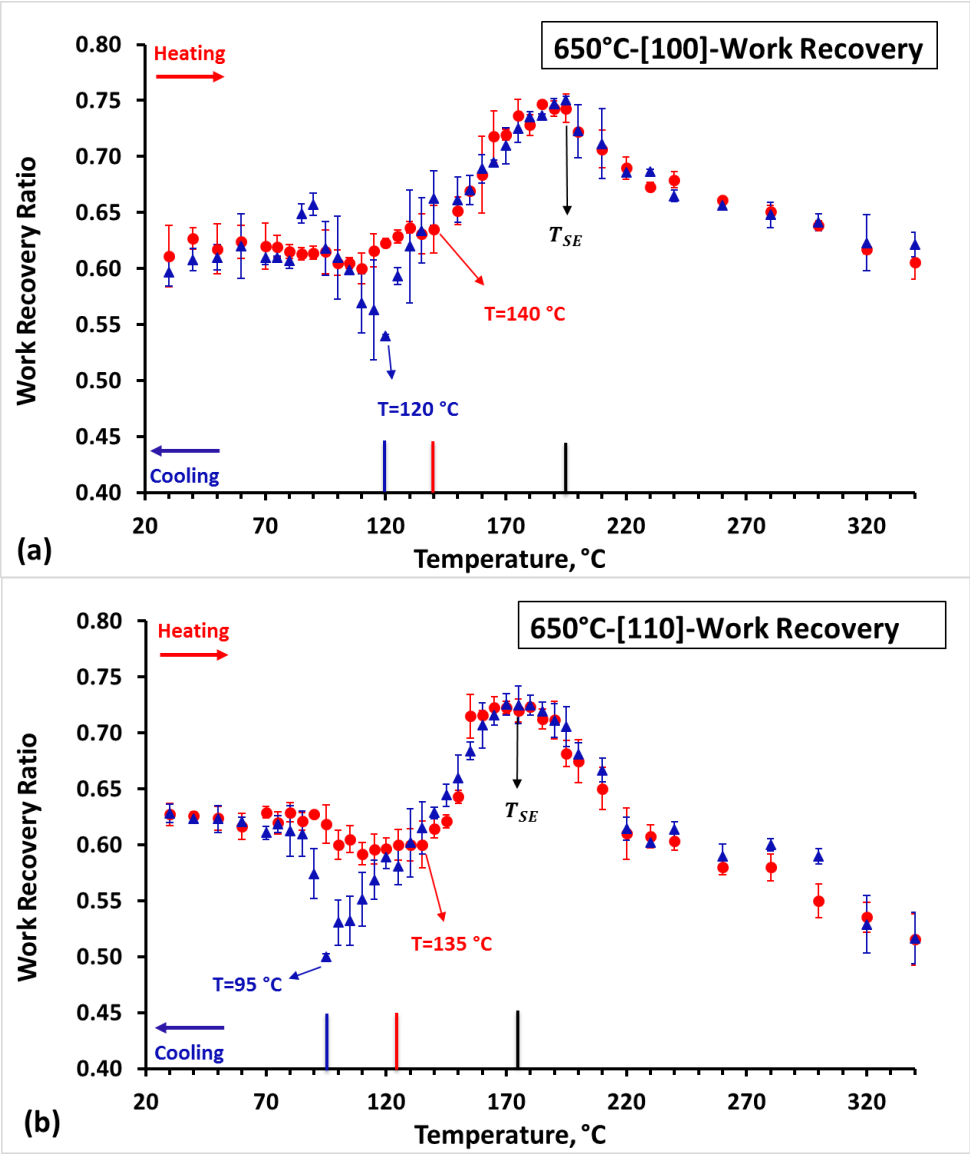

Figure 7.6: Spherical indentation response of work recoverable ratio as a function of temperature under 500 mN of single crystal NiTiHf aged at 650 °C-3h with heating process from 30 to 340 °C marked as circle and cooling process from 340 to 30 °C marked as triangle in (a) [111] and (b) [110] orientation.

Table 7.1 summarizes the TTs ($M_s^*, M_f^I, A_s^*, A_f^I$) obtained by using the method in section 7.2.1 and 7.2.2 from Figure 7.2a and Figure 7.6, as well as the TTs obtained from DSC. The A_s^* in [100] is difficult to determine from Figure 7.6a, but the ones observed in [110] and [111] are very close to each other. It can be seen that the TTs are very close in three orientations expect the M_s^*. It is well know that the martensite start temperature does not depend on orientations [50, 152] during thermal cycling experiment under near stress free condition (5 MPa). However, current indentation study shows that martensite starts temperatures M_s^* of three orientations are varied from work recovery response. Such orientation dependent behavior of TTs can be understood by the Clausius- Clapeyron (CC) relation (i.e. $\frac{\Delta\sigma}{\Delta T} = -\frac{\Delta H}{T_0\,\varepsilon_{tr}}$, where the $\Delta\boldsymbol{\sigma}$ is the change in the critical stress, ΔT is the change in temperature, and ΔH is the transformation enthalpy, T_0 is the equilibrium temperature, and $\boldsymbol{\varepsilon}_{tr}$ is the transformation strain). Since ΔH and T_0 are crystal orientation independent, thus, it is clear that the CC slope is inversely proportional to the $\boldsymbol{\varepsilon}_{tr}$. Under peak load of 500 mN (applied stress) during indentation experiments, the M_s^* observed from work recovery are different in three orientations as $\boldsymbol{\varepsilon}_{tr}$ is orientation dependent under stress. However, other than M_s^*, TTs (M_f^I, A_s^*, A_f^I) and T_{SE} are almost orientation independent from indentation experiments.

Table 7.1: Shape memory properties observed from indentation work recovery and hardness under 500 mN from [100], [110], and [111] orientations, as well as the DSC results.

	Orientation	M_s^* (°C)	M_f^I (°C)	A_s^* (°C)	A_f^I (°C)	T_{SE} (°C)
DSC		**123 (M_s)**	**85 (M_f)**	**145 (A_s)**	**175 (A_f)**	
Work Recovery	[100]	120	85	110	140	195
	[110]	95	85	135	150	175
	[111]	115	105	145	155	195

7.4.Conclusions

1. Temperature dependent indentation work recovery response of NiTiHf single crystal shows more clear temperature stages than poly crystalline, where these stages were explained and discussed by correlating the mechanical compression test. With a better understanding of the deformation behavior under the indenter, shape memory properties were again characterized.

2. Transformation temperatures and deformation stages (SE and PD) can be observed from spherical indentation response. The temperature, where shows the highest D_{max} during heating and cooling, corresponds to A_f^I and M_s^*, respectively, while the temperature at the lowest work recoverable ratio during heating and cooling corresponds to A_s^* and M_s^*, respectively.
3. It was revealed that shape memory properties such as M_f^I, A_s^*, A_f^I, and T_{SE} are almost orientation independent from indentation response of work recovery, but M_s^* shows orientation dependent behavior, which is opposite observation with thermal cycling experiments of single crystal SMAs.

8 GENERAL CONCLUSIONS AND FUTURE WORKS

NiTi-based polycrystalline shape memory alloys (superelastic and non-superelastic) were characterized using indentation techniques under both spherical and Berkovich indenter. Vickers hardness results were also included. Effect of indenter shape, load, temperature, and orientations on shape memory properties were investigated. Uniaxial compression mechanical results (constant stress thermal cycling, and isothermal stress cycling tests) of NiTi-based alloys were also performed to understand the mechanical behavior in macro scale, and then they were correlated with the small-scale indentation measurements. Moreover, orientation effects of single crystal NiTiHf alloys were also studied through indentation techniques. Based on all results discussed above, following conclusions can be arrived:

1. The spherical and Berkovich indentation responses of NiTi-based alloys are highly load/depth and composition dependent. Moreover, the indentation responses also depend on whether the material show superelasticity or not. Indentation work recoverable ratios of NiTi-based alloys are extremely depth dependent in spherical indentation and they decrease substantially with indentation depth while they are depth independent under Berkovich indenter.
2. Spherical indentation hardness of NiTi-based alloys increase with indentation depth due to the increase in the transformed region and plastic deformation during loading, while Berkovich indentation hardness decreases with depth due to increased plastic deformation. Vickers hardness of NiTi-based alloys are close to the Berkovich hardness

(minimum value) since Vickers measurement is a test with sharp tip. Moreover, spherical indenter shows the highest hardness values compared with sharp indenters (Vickers and Berkovich).

3. All three indenter tips show good agreement on indentation hardness that superelastic NiTiHfPd alloys are the strongest, and martensitic NiTi is the weakest. It can be concluded that superelastic behavior of SMAs can help to increase the indentation hardness within the same family.
4. Superelasticity increases the work recoverable ratio can be observed under both spherical and Berkovich indenters. Moreover, spherical indenter can produce more work recoverable ratio than Berkovich, where a perfect work recoverable ratio (spherical) was obtained on superelastic NiTiHfPd alloys under low load. The lower load, the higher work/depth recovery can be observed.
5. The modulus from spherical and Berkovich indentation responses of NiTi-based alloys initially decrease with indentation depth and then saturates at larger depth/load. Both measurements show similar value in contact modulus for all alloys, except NiTi alloys. Moreover, superelasticity does not affect on the modulus under both spherical and Berkovich indenters.
6. Indentation technique can be used as an alternative rapid method to determine some of the important shape memory properties of SMAs. Indentation response of a high-temperature NiTiHf alloy was determined as a function of temperature. A clear relationship between the work recoverable ratio and transformation temperatures, superelastic and plastic behavior was observed. Indentation response can be used to measure local superelasticity response, determine phase transformation temperatures

and reveal the temperature intervals of the deformation mechanisms of shape memory alloys.

7. The temperature, which shows the highest D_{max} during heating and cooling, corresponds to A_f and M_s, respectively, while the temperature at the lowest work recoverable ratio during heating and cooling corresponds to A_s and M_s, respectively. The temperature with the highest work recoverable ratio is the T_{SE}, and M_d can be determined at the temperature where the work recoverable ratio starts to saturate after $T_{SE.}$
8. This simple indentation technique is capable of quantitative characterization at micro- and nano-meter scales of shape memory materials. The results obtained using the indentation method are in a good agreement with the phase transformation behavior performed on bulk materials under compression and transformation temperatures obtained by DSC.
9. Such a new method of characterizing shape memory properties has several advantages than the conventional method: i) the programming interface of indentation technique makes the experiments easier and save time for researchers, ii) it can be employed as nondestructive testing of bulk SMAs, iii) the small scale measurement economically saves material, iv) it can precisely determine local properties at nano or macro scales, v) the purging system avoids oxidization at high temperature.
10. Temperature dependent of indentation work recoverable ratio, hardness, modulus were investigated between 30 and 340 C on as-received NiTiHf alloy, under two load levels. It was found that indentation response of work recovery ratio, hardness and modulus are highly temperature, and load dependent. Work recoverable ratio under low load

(500 mN) shows the TTs and deformation stages clearly, while the high load of 2000 mN cannot identify detail information completely due to the increased plasticity generated at higher load. High load of 2000 mN produces increased plasticity which impedes the superelastic behavior, results in a lower work recovery than low load (500 mN). Moreover, it can be conclude that higher load results in lower T_{SE}.

11. Phase transformation temperatures (M_s, M_f), T_{SE}, and M_d of non-superelastic NiTi and NiTiHf alloys were observed from spherical indentation during cooling process using the work recovery method under 500 mN. However, due to the weak mechanical behavior of NiTi alloy, its indentation characterizations with temperature are not as clear as high temperature/strength NiTiHf alloy.
12. Indentation contact modulus of SMAs decrease with decreasing temperature prior to the forward martensitic transformation due to softening of elastic constant, while inversely result was observed in Ti alloy. This method can be only used for determine the martensite start and finish temperatures.
13. Shape memory properties of superelasticity 50.8NiTi alloy cannot be characterized through indentation responses since the transformation temperatures are lower than room temperature. Indentation response of SMAs is temperature dependent, and it is revealed that TTs, T_{SE}, and M_d are load dependent, but low load shows more prominent and accurate results than the high load.
14. Temperature dependent indentation work recovery response of NiTiHf single crystal shows more clear temperature stages than poly crystalline, where these stages were explained and discussed by correlating the mechanical compression test. With a better

understanding of the deformation behavior under the indenter, shape memory properties were again characterized.

15. Transformation temperatures and deformation stages (SE and PD) can also be observed from spherical indentation response for single crystal. The temperature, where shows the highest D_{max} during heating and cooling, corresponds to A_f^I and M_s^*, respectively, while the temperature at the lowest work recoverable ratio during heating and cooling corresponds to A_s^* and M_s^*, respectively. It was revealed that shape memory properties such as M_f^I, A_s^*, A_f^I, and T_{SE} are almost orientation independent from indentation response of work recovery, but M_s^* shows orientation dependent behavior, which is opposite observation with thermal cycling experiments of single crystal SMAs.

In this current study, the effects of temperature, orientation, load level and indenter shape on the indentation response of NiTi-based shape memory alloys were investigated. In the light of the observed results, possible future studies on small-scale indentation measurements could be:

1. Investigate shape memory effect (SME) and two-way shape memory effect (TWSME) on NiTi and NiTiHf polycrystalline shape memory alloys by measuring the depth recovery of the post indent made with indentation.
2. Load effect on indentation response of single crystalline NiTiHf alloys is required for further study. Precipitation effect of indentation response should be studied as well.

3. Characterize the dynamic (high strain rate) nano-indentation response of NiTi-based alloys (NiTi or NiTiHfPd).

REFERENCES

[1] D.C. Lagoudas, Science and Business Media, LLC (2008).
[2] T. Duerig, R. Zadno, Butterworth-Heinemann, Engineering Aspects of Shape Memory Alloys(UK), 1990 (1990) 369-393.
[3] K. Gall, K. Juntunen, H.J. Maier, H. Sehitoglu, Y.I. Chumlyakov, Acta Materialia 49(16) (2001) 3205-3217.
[4] K. Otsuka, X. Ren, Progress in materials science 50(5) (2005) 511-678.
[5] H. Karaca, I. Kaya, H. Tobe, B. Basaran, M. Nagasako, R. Kainuma, Y. Chumlyakov, Materials Science and Engineering: A 580 (2013) 66-70.
[6] J. Ma, I. Karaman, R.D. Noebe, International Materials Reviews 55(5) (2010) 257-315.
[7] K. Eckelmeyer, Scripta Metallurgica 10(8) (1976) 667-672.
[8] P. Potapov, A. Shelyakov, A. Gulyaev, E. Svistunov, N. Matveeva, D. Hodgson, Materials Letters 32(4) (1997) 247-250.
[9] H.E. Karaca, S.M. Saghaian, G. Ded, H. Tobe, B. Basaran, H.J. Maier, R.D. Noebe, Y.I. Chumlyakov, Acta Materialia 61(19) (2013) 7422-7431.
[10] H.Y. Kim, T. Jinguu, T.-h. Nam, S. Miyazaki, Scripta Materialia 65(9) (2011) 846-849.
[11] R. Liu, D. Li, Y. Xie, R. Llewellyn, H. Hawthorne, Scripta Materialia 41(7) (1999) 691-696.
[12] W. Ni, Y.-T. Cheng, D.S. Grummon, Applied Physics Letters 82(17) (2003) 2811.
[13] H.E. Karaca, E. Acar, G.S. Ded, B. Basaran, H. Tobe, R.D. Noebe, G. Bigelow, Y.I. Chumlyakov, Acta Materialia 61(13) (2013) 5036-5049.
[14] W. Ni, Y.-T. Cheng, D.S. Grummon, Applied physics letters 80(18) (2002) 3310-3312.
[15] X. Fei, D.S. Grummon, C. Ye, G.J. Cheng, Y.-T. Cheng, Journal of Materials Science 47(5) (2012) 2088-2094.
[16] M. Frâemond and S. Miyazaki, Shape Memory Alloys (Springer, New York, 1996).
[17] K. Otsuka, C.M. Wayman, Shape memory materials, Cambridge university press1999.
[18] G. Kurdjumov, L. Khandros, Doklady Akademii Nauk SSSR 66 (1949) 211-213.
[19] L. Chang, T. Read, American Institute of Mining and Metallurgical Engineers 191 (1951) 47.
[20] Y. Liu, P. McCormick, Acta Metallurgica et Materialia 38(7) (1990) 1321-1326.
[21] L. Contardo, G. Guenin, Acta Metallurgica et Materialia 38(7) (1990) 1267-1272.
[22] D.A. Miller, D.C. Lagoudas, Smart Materials and Structures 9(5) (2000) 640.
[23] X. Ren, K. Otsuka, Physical review letters 85(5) (2000) 1016.
[24] J. Perkins, R. Sponholz, Metallurgical transactions A 15(2) (1984) 313-321.
[25] E. Cingolani, M. Ahlers, M. Sade, Acta metallurgica et materialia 43(6) (1995) 2451-2461.
[26] R. Stalmans, J. Van Humbeeck, L. Delaey, Acta metallurgica et materialia 40(11) (1992) 2921-2931.
[27] K. Enami, A. Nagasawa, S. Nenno, Scripta Metallurgica 9(9) (1975) 941-948.
[28] L. Gracia-Villa, J. Puértolas, (2002).
[29] T. Fukuda, M. Takahata, T. Kakeshita, T. Saburi, Materials Transactions 42(2) (2001) 323-328.

[30] M.S. Shakeri, J. Khalil-Allafi, V. Abbasi-Chianeh, A. Ghabchi, Journal of Alloys and Compounds 485(1–2) (2009) 320-323.
[31] K. Wada, Y. Liu, Journal of Alloys and Compounds 449(1–2) (2008) 125-128.
[32] E. Cingolani, M. Ahlers, Materials Science and Engineering: A 273–275(0) (1999) 595-599.
[33] X. Zhang, J. Fernandez, J. Guilemany, Origin of two way shape memory effect in Cu-based shape memory alloys, Journal de Physique IV (Proceedings), EDP sciences, 2003, pp. 487-493.
[34] I. MAYO, G. KAUFFMAN, The story of Nitinol: The serendipitous discovery of the memory metal and its applications, Springer-Verlag New York, INC, 1996.
[35] W.J. Buehler, letter to Amy Axt hanson (15 Jun 1991).
[36] Hanson, A. A. Technology Review 1991, 94(4), 26.
[37] Wang, F. E; Buehler, W. J.; Pickart, S. J. J. App. Phys. 1965, 36, 3232.
[38] Wang, F. E.; DeSavage, B. F.; Buehler, W. J. J. App. Phys. 1968, 39, 2166.
[39] Kurtz, J. The New York Times, 19 May 1991, Section F, p 7.
[40] Galton, L. Parade: The Sunday Newspaper Magazine, 12 June 1977, p 11.
[41] W.J. Buehler, F.E. Wang, Ocean Engineering 1(1) (1968) 105-120.
[42] S. Padula, II, S. Qiu, D. Gaydosh, R. Noebe, G. Bigelow, A. Garg, R. Vaidyanathan, Metallurgical and Materials Transactions a-Physical Metallurgy and Materials Science 43A(12) (2012) 4610-4621.
[43] P. Krulevitch, A.P. Lee, P.B. Ramsey, J.C. Trevino, J. Hamilton, M.A. Northrup, Microelectromechanical Systems, Journal of 5(4) (1996) 270-282.
[44] T. Duerig, A. Pelton, D. Stöckel, Bio-medical materials and engineering 6(4) (1996) 255-266.
[45] J. O'Leary, J. Nicholson, R. Gatturna, T. Duerig, K. Melton, D. Stöckel, C. Waguian, Engineering Aspects of Shape Memory Alloys, Butterworth-Heinemann, Boston, T. Duerig et al., ed, 1990.
[46] H. Sehitoglu, I. Karaman, R. Anderson, X. Zhang, K. Gall, H. Maier, Y. Chumlyakov, Acta Materialia 48(13) (2000) 3311-3326.
[47] H. Sehitoglu, J. Jun, X. Zhang, I. Karaman, Y. Chumlyakov, H. Maier, K. Gall, Acta Materialia 49(17) (2001) 3609-3620.
[48] K. Gall, H. Sehitoglu, R. Anderson, I. Karaman, Y.I. Chumlyakov, I.V. Kireeva, Materials Science and Engineering: A 317(1) (2001) 85-92.
[49] I. Kaya, (2014).
[50] S. Saghaian, H. Karaca, H. Tobe, M. Souri, R. Noebe, Y. Chumlyakov, Acta Materialia 87 (2015) 128-141.
[51] H.E. Karaca, S.M. Saghaian, B. Basaran, G.S. Bigelow, R.D. Noebe, Y.I. Chumlyakov, Scripta Materialia 65(7) (2011) 577-580.
[52] X. Meng, W. Cai, Y. Fu, J. Zhang, L. Zhao, Acta Materialia 58(10) (2010) 3751-3763.
[53] X. Meng, W. Cai, K. Lau, L. Zhao, L. Zhou, Intermetallics 13(2) (2005) 197-201.
[54] H.E. Karaca E.Acar, G.S. Ded, S. M. Saghaian, B. Basaran, H.Tobe, M.Kok, H. J. Maier, R.D. Noebe, YI Chumlyakov. Compression response of Ni45.3Ti29.7Hf20Cu5 high temperature shape memory alloys Materials Science and Engineering A 2014;submitted.
[55] H. Hertz, Miscellaneous papers, Macmillan, London, U.K., 1896.
[56] D. Tabor, Hardness of Metals. Clarendon, Oxford, U.K., 1951
[57] B.R. Lawn, Fracture of brittle solids, Cambridge university press1993.
[58] F. Auerbach, Ann. Phys. Chem 43 (1891) 61.
[59] F. Frank, B. Lawn, Proceedings of the Royal Society of London. Series A. Mathematical and Physical Sciences 299(1458) (1967) 291-306.
[60] W.C. Oliver, G.M. Pharr, Journal of materials research 7(06) (1992) 1564-1583.
[61] L. Qian, X. Xiao, S. Wen, Langmuir 16(2) (2000) 662-670.

[62] X. Xiao, L. Qian, Langmuir 16(21) (2000) 8153-8158.
[63] J. Luo, L. Qian, S. Wen, L. Wen, S. Wen, L.K. Li, Tribology transactions 42(4) (1999) 912-916.
[64] R. Pond, Y. Chai, S. Celotto, Materials Science and Engineering: A 378(1) (2004) 47-51.
[65] C.P. Frick, T.W. Lang, K. Spark, K. Gall, Acta Materialia 54(8) (2006) 2223-2234.
[66] A.C. Fischer-Cripps, Nanoindentation, Springer2011.
[67] D. Tabor, The hardness of metals, ClarendonP1951.
[68] B.W. Mott, Micro-indentation hardness testing, Butterworths Scientific Publications1956.
[69] A. P. Ternovskiœ, V. P. Alekhin, M. Kh. Shorshorov, et al.,Zavod. Lab. 39, 1242 (1973)

[70] S. I. Bulychev, V. P. Alekhin, M. Kh. Shorshorov, et al.,Zavod. Lab. 41, 1137 (1975).

[71] I. Zarudi, L. Zhang, W. Cheong, T. Yu, Acta materialia 53(18) (2005) 4795-4800.
[72] W.C. Oliver, G.M. Pharr, Journal of materials research 19(01) (2004) 3-20.
[73] A. Fischer-Cripps, Journal of materials science 32(3) (1997) 727-736.
[74] K. Johnson.
[75] G. Sinclair, P. Follansbee, K. Johnson, International Journal of Solids and Structures 21(8) (1985) 865-888.
[76] C.-M. Cheng, Y.-T. Cheng, Applied physics letters 71(18) (1997) 2623-2625.
[77] S.D. Mesarovic, N.A. Fleck, Proceedings of the Royal Society of London. Series A: Mathematical, Physical and Engineering Sciences 455(1987) (1999) 2707-2728.
[78] M.F. Doerner, W.D. Nix, Journal of Materials research 1(04) (1986) 601-609.
[79] W. Ni, Y.-T. Cheng, C.-M. Cheng, D.S. Grummon, Journal of materials research 19(01) (2004) 149-157.
[80] W. Ni, Y.-T. Cheng, D.S. Grummon, Surface and Coatings Technology 177-178 (2004) 512-517.
[81] X.-G. Ma, K. Komvopoulos, Applied physics letters 83(18) (2003) 3773-3775.
[82] Y.J. Zhang, Y.T. Cheng, D.S. Grummon, Journal of Applied Physics 98(3) (2005).
[83] M. Qidwai, D. Lagoudas, International Journal for Numerical Methods in Engineering 47(6) (2000) 1123-1168.
[84] H. Naito, Y. Matsuzaki, T. Ikeda, Smart materials and structures 13(3) (2004) 535.
[85] Y. Ivshin, T.J. Pence, Journal of intelligent material systems and structures 5(4) (1994) 455-473.
[86] M. Brocca, L. Brinson, Z. Bažant, Journal of the Mechanics and Physics of Solids 50(5) (2002) 1051-1077.
[87] F. Auricchio, U. Stefanelli, International journal for numerical methods in engineering 61(1) (2004) 142-155.
[88] Y. Zhang, Y.-T. Cheng, D.S. Grummon, Journal of Applied Physics 101(5) (2007) 053507.
[89] J. Su, W.M. Huang, M.H. Hong, Smart materials and structures 16(1) (2007) S137.
[90] Y.J. Zhang, Y.T. Cheng, D.S. Grummon, Applied Physics Letters 88(13) (2006).
[91] K. Gall, K. Juntunen, H. Maier, H. Sehitoglu, Y.I. Chumlyakov, Acta Materialia 49(16) (2001) 3205-3217.
[92] W. Ni, Y.-T. Cheng, D.S. Grummon, Surface and Coatings Technology 177 (2004) 512-517.
[93] W. Poisl, W. Oliver, B. Fabes, Journal of materials research 10(08) (1995) 2024-2032.
[94] T. Suzuki, T. Ohmura, Philosophical Magazine A 74(5) (1996) 1073-1084.
[95] B.D. Beake, J.F. Smith, Philosophical Magazine A 82(10) (2002) 2179-2186.
[96] B.D. Beake, S.R. Goodes, J.F. Smith, Zeitschrift für Metallkunde 94(7) (2003) 798-801.

[97] J.C. Trenkle, C.E. Packard, C.A. Schuh, Review of Scientific Instruments 81(7) (2010) 073901.
[98] C.A. Schuh, C.E. Packard, A.C. Lund, Journal of materials research 21(03) (2006) 725-736.
[99] A. Sawant, S. Tin, Scripta materialia 58(4) (2008) 275-278.
[100] A.M. Wood, T. Clyne, Acta materialia 54(20) (2006) 5607-5615.
[101] A.M. Wood, S. Sanjabi, Y. Fu, Z. Barber, T. Clyne, Surface and Coatings Technology 202(13) (2008) 3115-3120.
[102] X. Huang, J. Nohava, B. Zhang, A. Ramirez, International Journal of Smart and Nano Materials 2(1) (2011) 39-49.
[103] K. Komvopoulos, X.-G. Ma, Applied Physics Letters 87(26) (2005) 263108.
[104] V.V. Shastry, U. Ramamurty, Smart Materials and Structures 22(7) (2013) 077002.
[105] B. Gan, M. Gatepin, S. Cantonwine, S. Tin, Philosophical Magazine Letters 92(5) (2012) 254-261.
[106] J. Mason, A. Lund, C. Schuh, Physical review B 73(5) (2006) 054102.
[107] C. Schuh, A. Argon, T. Nieh, J. Wadsworth, Philosophical Magazine 83(22) (2003) 2585-2597.
[108] Y. Liu, P. Labossiere, H. Sehitoglu, Y.I. Chumlyakov, Urbana 51 (2002) 61801.
[109] G. Laplanche, J. Pfetzing-Micklich, G. Eggeler, Acta Materialia 78 (2014) 144-160.
[110] P. Li, H.E. Karaca, Y.-T. Cheng, Journal of Alloys and Compounds 651 (2015) 724-730.
[111] H.E. Karaca, E. Acar, H. Tobe, S.M. Saghaian, Materials Science and Technology (United Kingdom) 30(13) (2014) 1530-1544.
[112] H. Karaca, S. Saghaian, G. Ded, H. Tobe, B. Basaran, H. Maier, R. Noebe, Y. Chumlyakov, Acta Materialia 61(19) (2013) 7422-7431.
[113] H. Karaca, E. Acar, G. Ded, S. Saghaian, B. Basaran, H. Tobe, M. Kok, H. Maier, R. Noebe, Y. Chumlyakov, Materials Science and Engineering: A 627 (2015) 82-94.
[114] H. Karaca, E. Acar, B. Basaran, R. Noebe, Y. Chumlyakov, Scripta Materialia 67(5) (2012) 447-450.
[115] X. Meng, W. Cai, Y. Zheng, Y. Tong, L. Zhao, L. Zhou, Materials Letters 55(1) (2002) 111-115.
[116] W. Yan, Q. Sun, X.-Q. Feng, L. Qian, International journal of solids and structures 44(1) (2007) 1-17.
[117] Z. Farhat, G. Jarjoura, M. Shahirnia, Metallurgical and Materials Transactions a-Physical Metallurgy and Materials Science 44A(8) (2013) 3544-3551.
[118] Y.-T. Cheng, C.-M. Cheng, Journal of Materials research 13(04) (1998) 1059-1064.
[119] A. Sinha, P. Chattopadhyay, Materials Science and Engineering: A 552 (2012) 540-546.
[120] A. Amini, C. Cheng, Scientific reports 3 (2013).
[121] D. Tabor, Philosophical Magazine A 74(5) (1996) 1207-1212.
[122] J. Swadener, E. George, G. Pharr, Journal of the Mechanics and Physics of Solids 50(4) (2002) 681-694.
[123] K. McElhaney, J. Vlassak, W. Nix, Journal of Materials Research 13(05) (1998) 1300-1306.
[124] W.D. Nix, H. Gao, Journal of the Mechanics and Physics of Solids 46(3) (1998) 411-425.
[125] G. Kang, W. Yan, Philosophical Magazine 90(5) (2010) 599-616.
[126] L. Qian, M. Li, Z. Zhou, H. Yang, X. Shi, Surface and Coatings Technology 195(2) (2005) 264-271.
[127] D. Bahr, D. Kramer, W. Gerberich, Acta materialia 46(10) (1998) 3605-3617.
[128] Q. Kan, W. Yan, G. Kang, Q. Sun, Journal of the Mechanics and Physics of Solids 61(10) (2013) 2015-2033.
[129] E. Acar, H. Karaca, H. Tobe, R. Noebe, Y. Chumlyakov, Intermetallics 54 (2014) 60-68.

[130] Y. Zhang, Y.-T. Cheng, D.S. Grummon, Journal of Materials Research 22(10) (2007) 2851-2855.
[131] K. Yamauchi, Shape memory and superelastic alloys: technologies and applications, Woodhead Publishing2011.
[132] J. Van Humbeeck, Materials Science and Engineering: A 273 (1999) 134-148.
[133] C. Zhang, L. Zhao, T. Duerig, C. Wayman, Scripta Metallurgica et Materialia 24(9) (1990) 1807-1812.
[134] Y. Tanaka, Y. Himuro, R. Kainuma, Y. Sutou, T. Omori, K. Ishida, Science 327(5972) (2010) 1488-1490.
[135] J. San Juan, M.L. Nó, C.A. Schuh, Nature nanotechnology 4(7) (2009) 415-419.
[136] S.M. Saghaian, H.E. Karaca, M. Souri, A.S. Turabi, R.D. Noebe, Materials & Design 101 (2016) 340-345.
[137] S.M. Saghaian, H.E. Karaca, H. Tobe, M. Souri, R. Noebe, Y.I. Chumlyakov, Acta Materialia 87(0) (2015) 128-141.
[138] Y. Li, X. Fang, B. Xia, X. Feng, Scripta Materialia 103 (2015) 61-64.
[139] L. Qian, X. Xiao, Q. Sun, T. Yu, Applied Physics Letters 84(7) (2004) 1076-1078.
[140] P. Li, H.E. Karaca, Y.-T. Cheng, scientific reports (2017).
[141] J. Tallon, A. Wolfenden, Journal of Physics and Chemistry of Solids 40(11) (1979) 831-837.
[142] M. Fukuhara, A. Sanpei, Journal of materials science letters 12(14) (1993) 1122-1124.
[143] D.O. Thompson, D. Holmes, Journal of Applied Physics 30(4) (1959) 525-541.
[144] X. Ren, N. Miura, K. Taniwaki, K. Otsuka, T. Suzuki, K. Tanaka, Y.I. Chumlyakov, M. Asai, Materials Science and Engineering: A 273 (1999) 190-194.
[145] X. Ren, N. Miura, J. Zhang, K. Otsuka, K. Tanaka, M. Koiwa, T. Suzuki, Y.I. Chumlyakov, M. Asai, Materials Science and Engineering: A 312(1) (2001) 196-206.
[146] K. Otsuka, X.B. Ren, Factors affecting the Ms temperature and its control in shape-memory alloys, Materials Science Forum, Trans Tech Publ, 2002, pp. 177-184.
[147] K. Otsuka, C. Wayman, Shape memory materials (1998) 27-49.
[148] G. Welsch, W. Bunk, Metallurgical Transactions A 13(5) (1982) 889-899.
[149] Y. Lee, G. Welsch, Materials Science and Engineering: A 128(1) (1990) 77-89.
[150] Y.-T. LEE, Zeitschrift fuer Metallkunde 78 (1987) 49-57.
[151] G. Yoder, L. Cooley, T. Crooker, Metallurgical Transactions A 8(11) (1977) 1737-1743.
[152] P. Li, H.E. Karaca, Y.I. Chumlyakov, Journal of Alloys and Compounds (2017).

VITA

Peizhen Li was born in 1988 in Jilin, China. She studied three years of collage in China University of Mining and Technology and then transferred to University of Kentucky in 2010. She got her Bachelor's degree in Mechanical Engineering from University of Kentucky, Kentucy, USA. In December 2011. She was then admitted to the Ph.D. program in the Department of Mechanical Engineering at the University of Kentucky under the supervision of Prof. Haluk E. Karaca. During the PhD study, she investigated the mechanical characterization behavior of single crystal CoNiAl shape memory alloys at high temperature. Then she focused on the small-scale mechanical behavior of NiTi-based shape memory alloys, the nano and micro indentation. She published four journal papers and two conference papers during his graduate tenure. In addition, she has one journal article under review and five journal articles which are ready to be submitted.

Peizhen Li, Haluk E.Karaca, YT Cheng "Rapid Characterization of Local Shape Memory Properties through Indentation" **Nature Scientific Report**, 2017 (submitted)

Peizhen Li, Haluk E.Karaca, Y. Chumlyakov "Orientation Dependent Compression Behavior of High Temperature Co35Ni35Al30 Single Crystals" Journal of alloys and compounds, April 28 2017

Ilhom Saidjafarzoda, **Peizhen Li**, Dovletgeldi Seyitliyev, Khomidkohodza Kholikov, Zachary Thomas, Omer San, Haluk Karaca, Ali & O Er "Laser Shock Wave Assisted Patterning on NiTi Shape Memory Alloy Surfaces" Journal of shape memory and superelasticity, 2017 (Submitted)

Chen S, Yu L, Ren J, Xie X, Li X, Xu Y, Zhao G, **Li P**, Yang F, Ren Y, Liaw PK. Self-Similar Random Process and Chaotic Behavior In Serrated Flow of High Entropy Alloys. **Nature Scientific Reports**. 2016;6

Peizhen Li, Haluk E.Karaca, YT Cheng "Spherical Indentation of NiTi-based Shape Memory Alloys" Journal of alloys and compounds, 2015

H.E. Karaca, A.S. Turabi, B. Basaran, A.K. Pathak, I. Dubenko, N. Ali, Y. Chumlyakov, **P. Li** "Compressive Response of Polycrystalline NiCoMnGa High-Temperature Metamagnetic Shape Memory Alloys" Journal of Materials Engineering and Science, 2013